



VCU

Virginia Commonwealth University
VCU Scholars Compass

Theses and Dissertations

Graduate School

2016

OPTIMIZING COBALT CARBIDE BASED NANOMATERIALS BY USING NUCLEATING AGENTS AND STATISTICAL ROUTES

Turki I. Almugaiteeb

Follow this and additional works at: <https://scholarscompass.vcu.edu/etd>



Part of the [Engineering Commons](#), and the [Life Sciences Commons](#)

© The Author

Downloaded from

<https://scholarscompass.vcu.edu/etd/4310>

This Dissertation is brought to you for free and open access by the Graduate School at VCU Scholars Compass. It has been accepted for inclusion in Theses and Dissertations by an authorized administrator of VCU Scholars Compass. For more information, please contact libcompass@vcu.edu.

© TURKI I. ALMUGAITEEB 2016
ALL RIGHTS ARE RESERVED

**OPTIMIZING COBALT CARBIDE BASED NANOMATERIALS BY USING
NUCLEATING AGENTS AND STATISTICAL ROUTES**

A dissertation submitted in partial fulfillment of the requirements for the degree of
Doctor of Philosophy at Virginia Commonwealth University

By

Turki I. Almugaiteeb

B.S., King Fahad University of petroleum and mineral, 2005

Director: Everett E. Carpenter,

Professor of Chemistry

Virginia Commonwealth University

Richmond, Virginia

March 2016

Acknowledgements

First and foremost I want to thank my advisor Professor Everett Carpenter. It has been an honor to be part of his lab members. He has taught me, both consciously and unconsciously, how to solve problems and open mind to different approach in interesting interdisciplinary program nanoscience/nanotechnology. I appreciate all his contributions of time, ideas, and funding to make my Ph.D. experience productive and stimulating. The support I have received was tremendously great for me to keep up motivated after trying many ideas for my experiments. I have been honored also to be part of the project of rare earth free permanent magnet materials (2 million \$) which was funded by DOE between 2012 -2014. In this project I have also learned great deal of technologies such as micro reaction systems and I did apply my engineering background to solve problems in flow chemistry and optimization. I am thankful for all my committee professors who have directly or indirectly sometimes helped me out with my research and provided valuable advices through the years. I also appreciate the friendly atmosphere I experienced working with my lab mates who been more like a family for me; we spent together great time and challenging moments when dealing with everyday experimental work. I would like to thank my family who been supporting during struggles and hardship. I would not also forget the families here at Richmond who I received great support during hardship away from family back home.

Table of contents

| | |
|---|-----------|
| List of figures..... | iv |
| Chapter 1. Introduction..... | 1 |
| 1.1 Overview | 2 |
| 1.2 Ferromagnetism | 4 |
| 1.2.1 Ferromagnetic material and basic properties | 4 |
| 1.2.2 Ferromagnetism; theory and background..... | 7 |
| 1.2.3 Magnetic nanocomposites (MNCs)..... | 18 |
| 1.2.4 Magnetic Pinning:..... | 19 |
| Chapter 2. Microreactor | 22 |
| 2.1 Introduction: | 23 |
| 2.2. Microfluidic types: | 23 |
| 2.2.1 Capillary microfluidic type..... | 23 |
| 2.2.2 Microfluidic chip type..... | 28 |
| 2.3 Synthesising Copper face centered cube nanoparticles structure using MMRS..... | 32 |
| 2.3.1 Experimental..... | 32 |
| 2.3.2 Materials characterization..... | 33 |
| 2.3.3 Results and discussions..... | 34 |
| 2.4 Synthesising cobalt hexagonal nanoparticles structure in MMRS..... | 36 |
| 2.4.1 Experimental..... | 36 |
| 2.4.2 Results and discussions..... | 38 |
| 2.5 Synthesising Cobalt carbide in modified MMRS | 40 |
| 2.5.1 Introduction and motivation..... | 40 |
| 2.5.2 Experimental..... | 41 |
| 2.5.3 Results and discussions..... | 42 |
| 2.5.4 Conclusion | 45 |
| Chapter 3. JMP statistical software for design of experiments | 48 |
| 3.1 Introduction..... | 49 |
| 3.2 Design of experiments (DOE)..... | 51 |
| 3.2.1 Design of experiments types:..... | 53 |
| Chapter 4. Design of experiment to produce enhanced Co_xC magnetic product in polyol with SAS-JMP statistics | 61 |
| 4.1 Overview/ Motivation | 62 |
| 4.2 Statistical approach to enhance ideal energy product of cobalt carbide and verify the significant parameters..... | 63 |
| 4.2.1 Synthesis of cobalt carbide using based on JMP design of experiment..... | 64 |
| 4.2.2 Materials characterization..... | 64 |
| 4.2.3 Result and discussion..... | 65 |

| | |
|--|------------|
| Chapter 5. High magnetocrystalline anisotropy of Co_xC ($x=2$ or 3) | 77 |
| 5.1 Introduction..... | 78 |
| 5.2 Experimental..... | 78 |
| 5.3 Results and discussions..... | 78 |
| 5.3 Conclusion..... | 85 |
| Chapter 6. Co_xC ($x= 2$ or 3) synthesis using nucleating agent..... | 87 |
| 6.1 Overview/Motivation..... | 88 |
| 6.2 Introduction..... | 91 |
| 6.3 Experimental methods..... | 94 |
| 6.3.1 Synthesis..... | 94 |
| 6.3.2 JMP design of experiment | 95 |
| <i>Coercivity selected to be the response for design of experiments results. When using varied concentration of noble metals such as Ag or Au, it is expected to result in diminishing magnetization unfortunately. At the same time due to possible shape or magnetocrystalline anisotropic control, the macroscopic coercivity can attain enhancement at room temperature.^{10,69,75,82}</i> | 96 |
| 6.3.3 Characterization..... | 96 |
| 6.4 Results..... | 98 |
| 6.4.1 Proposed mechanism..... | 98 |
| 6.4.2 Model fit..... | 99 |
| References | 111 |

List of figures

| | |
|---|----|
| Fig. 1.1.1 Energy product of various permanent magnet materials (a) ¹ , hysteresis loop for ferromagnetic materials showing coercivity (H_c) and saturated magnetization (M_s) (b). ² | 2 |
| Fig. 1.2.1.1 Permanent magnet sales by US Dollars also by metric tons for the largest current used materials. (a) Show the sales in dollars while (b) show the sales in tons. ³ | 5 |
| Table 1.2.1.1. Showing intrinsic magnetic properties of different PM materials. ² | 6 |
| Table 1.2.2.1.1. Properties of some ferromagnetic materials: T_c the curie temperature, K the anisotropy constant, M_s per unit volume saturation magnetization, and l_{ex} is the exchange length; that can be compared to domain wall thickness, where; $l_{ex} = \sqrt{A/K}$ = and A is the exchange stiffness. ⁵ | 9 |
| Fig. 1.2.2.1.1. Single domain hysteresis loop obtained for an arbitrary angle, ϕ , between the magnetic field and the anisotropy axis. Important magnetic quantities such as coercivity H_c , and remanant magnetization M_r depend on ϕ whereas intrinsic saturation magnetization M_s does not depend on. ⁵ | 10 |
| Fig. 1.2.2.2.2. Increase in coercivity when reaching critical size. ¹² | 13 |
| Fig. 1.2.2.2.3. (a) TEM images of Cobalt nanowires produced by introducing $RuCl_3$ in polyol media (b) Hysteresis a) at room temperature showing coercivity of 4.5 Oe b) Hysteresis of the sample in toluene at 150K c) Simulation of the frozen sample magnetization curve using Stoner-Wolfarth. ^{13,14} | 14 |
| Fig. 1.2.3.1. (a) On the far left show magnetic single multi domain structure in a bulk material (b) Show magnetic single domain structure for nano particles. (c) Critical size of single domain and superparamagnetism of several materials. ¹⁵ | 18 |
| Fig. 2.2.1.1. Capillary reactor schematic used to synthesis CdSe QDs. The precursor solutions were pumped in a Y shaped junction to be mixed in a convective mixer before entering the heated PTEE tubing where nucleation and growth occur. ²⁷ | 24 |
| Fig. 2.2.1.2. TEM images for; (a-c) fcc cobalt nanoparticles 3.6 nm obtained at flow rate of 0.9 ml/min and quenched at the outlet of the microfluidic reactor. With diffraction ring image showing the crystal structure, (d-f) show hcp cobalt nanoparticles of 3.5nm produced at flow rate of 0.08 ml/min, and (g-i) show spherical particles of epsilon crystal structure ϵ with an average size of 4.7 n m. ³⁰ | 26 |
| Fig. 2.2.1.3. Absorption and emission spectra of CdSe nanoparticles synthesized at 280°C with different resident time. ²⁷ | 27 |
| Fig. 2.2.1.4. TEM image of 3.6 nm CdSe produced in microfluidic reactor within 160 s resident time. ²⁷ | 28 |
| Fig. 2.2.2.1. Microreactor made of glass fabricated by Micronit for typical use for quantum dot synthesis. ²⁷ | 29 |
| Fig. 2.2.2.2.1. Left image shows the photoluminescence spectra of CdSe product from capillary microreactor using different alkyl chain lengths. The right image shows the peak emission wavelength vs the chain length of alkyl amine at different reaction times. It concludes that longer alkyl chains showed smaller QDs with blue shifted | |

| | |
|--|----|
| emission due to diffusion of alkyl long chain compared to the smaller ones resulting growth rates reduction. ^{27,28} | 31 |
| Fig. 2.3.3.1 Top XRD scans for 10 ml/min flow rate of Cu(NO ₂) ₂ in ethanol at 180°C and 20 bars matching FCC copper structure of JCPDS card no. 4-0836 below peaks. The crystal size of 50 nm was calculated using Scherrer calculator tool from High score. | 35 |
| Fig. 2.4.1.1. Modular Microreaction system (MMRS) containing all parts; mixture, sandwich microreactor, inlet/outlet modules, and flanges..... | 37 |
| Fig. 2.4.2.2. Diagram showing three different flow regimes in micro fluidic reactors. In (a) In continuous flow parabolic velocity profile is formed across the channels when a friction with the tube wall, the velocity will be faster at the center of the flow with respect to the flow profile, (b) In slug flow the flow profile is discrete due to the immiscible phase introduced in the flow stream that can be gas or liquid that will cause convective mixing occurring across the channels, (c) flow stream in discrete droplets from immiscible liquid phase that are beneficially isolated from the channel walls. ²⁷ | 39 |
| Fig. 3.2.1. Typical model for a process system. | 51 |
| Fig. 3.2.1.2. Box-Behnken design for three factors. ⁵⁵ | 57 |
| Fig. 3.2.1.4. Surface response profile showing forecaster of surface area in (m ² /g) response with respect to variation in in time, and ramp temperature. | 60 |
| Fig. 4.2.3.0.1. La-Mer model demonstrate the mechanism of the growth and nucleation process vs time. At critical concentration (C _{criti}) the of nucleation process (stage II) start till the growth process kick in (stage III). ⁶³ | 68 |
| Fig. 4.2.3.2. The sequential nature of response surface methodology. ⁵⁴ | 69 |
| Fig. 4.2.3.2. Prediction profile showing the three factors (reaction time, cobalt concentration, and reaction temperature) optimized to reach the highest response of ideal magnetic product at 6.64 MGOe..... | 70 |
| Table 4.2.3.2. Interaction table showing all the interacting factor terms with respect to probability. | 71 |
| Fig. 4.2.3.4. Hysteresis of the proposed run for optimized factors predicted in fig. 4.2.3.3. | 72 |
| Fig. 4.2.3.5. Stationary points for; maximum response (top right fig.), minimum response (bottom fig.), and saddle point (top right fig.) ⁵⁴ | 74 |
| Fig. 4.2.3.6. Surface profile graph showing stationary point of a saddle point in the top corner where reaction time with cobalt concentration level interaction will significantly affect response (H _c xM _s). | 75 |
| Fig. 4.2.3.7. Contour profile showing two factors ([Co], time) interaction with response (H _c xM _s). | 76 |
| Fig. 5.3.0.1. XRD diffraction pattern for CoC nanoparticles. The crystallite size for each phase has been determined using Scherrer formula. (For interpretation of the references to color in this fig., the reader is referred to the web version of this article.) | 79 |
| Fig. 5.3.2. TEM images of CoC nanoparticles. The particles shape is rod like particles. | 80 |
| Fig. 5.3.3. Specific magnetic study of CoxC nanoparticles: (a) Magnetization dependence of an external magnetic field at different temperatures. (b) Coercivity dependence of temperatures (determination of TB at HC=0). (c) Temperature | |

| | |
|--|-----|
| dependent on M_r/M_s ratio reveals uniaxial anisotropy for Co_xC . (d) Magnetic domain phase diagram: determination of Co_xC nanoparticles critical sizes. (e) Temperature dependent on magnetization at $H=1$ and 5 kOe. Inset fig. shows paramagnetic behavior at higher temperature. (f) Calculation of the Curie temperature from the cohesive energy model. | 82 |
| Fig. 6.2.1. The increase of $[\text{OH}^-]/[\text{Co}]$ ratio shifted cobalt from hcp phase to fcc. ⁵⁹ ... | 92 |
| Table 6.3.2.1. Surface response design table showing three factors; time, temperature, $[\text{Ag}]$, and $[\text{Co}]$. Also, coercivity H_c was chosen as response. | 97 |
| Figure 6.4.1. Schematic show the mechanism heterogamous growth of cobalt carbide controlled shape assisted by the nucleation sites of silver nanoparticles. | 98 |
| Figure 6.4.2.1 Fit Y by X from JMP software showing the regression of H_c (Oe) vs Temp. ($^{\circ}\text{C}$) Where H_c can possibly be highest at 285°C around 3kOe | 100 |
| Figure 6.4.2.2 Fit Y by X from JMP software showing the regression of H_c vs Temp. Where H_c reaches 3kOe at 3 hours and 2.5kOe at 1 hour. | 101 |
| Figure 6.4.2.3 Fit Y by X from JMP software showing the regression of H_c (Oe) vs $[\text{Ag}]$ (M). Where H_c can possibly as high as 3kOe when silver concentration is low. | 101 |
| Figure 6.4.2.4 Fit Y by X from JMP software showing the regression of H_c vs Temp. Where H_c can possibly be highest at low and high cobalt concentrations. | 102 |
| Table 6.4.2.1. The table reports the strength of the interaction between different terms at the source column based on their strength at the Prob>F column. | 103 |
| Figure 6.4.2.4. Hysteresis for sample 8 where silver concentration 0.017 M, cobalt concentration 0.039 M, temp 270°C , time 3 hrs. The silver concentration effect is pronounced in the hysteresis from the overlapping between the two phases soft and hard phases. While the it was possible to attain a coercivity of 2.6 kOe at low temperature as a concrescence of adding silver as nucleating agent. The poor magnetization is related to the non-ferromagnetic phase added to cobalt carbide. | 104 |
| Figure 6.4.2.5. Hysteresis for sample 1 where silver concentration 0.0005 M, cobalt concentration 0.059 M, temp 300°C , time 1 hrs. The silver concentration effect is less pronounced since its less than previous figure, the hysteresis from the overlapping between the two phases soft and hard phases. While the it was possible to attain a coercivity of 2.4 kOe at low temperature as a concrescence of adding silver as nucleating agent. | 104 |
| Figure 6.4.2.6. Hysteresis for sample 6 where silver concentration 0.017 M, cobalt concentration 0.039 M, temp 300°C , time 3 hrs. The low coercivity (466 Oe) indicates that cobalt carbide phase did not form, the phase is close to cobalt structure since magnetization saturated at 60 emu/g with low coercivity. | 105 |
| Figure 6.4.2.7. Hysteresis for sample 23 where silver concentration 0.0005 M, cobalt concentration 0.059 M, temp 270°C , time 3 hrs. The low coercivity (200 Oe) indicates that cobalt carbide phase did not form. | 106 |
| Figure 6.4.2.8. Hysteresis for sample 20 where silver concentration 0.017 M, cobalt concentration 0.039 M, temp 300°C , time 1 hrs. The low coercivity (650 Oe) indicates that cobalt carbide phase did not form. The poor magnetization id | |

| | |
|--|-----|
| related to insufficient source of magnetic material resulted from the low cobalt precursor concentration. | 106 |
| Figure 6.4.2.4.9 Hysteresis for sample 20 where silver concentration 0.017 M, cobalt concentration 0.039 M, temp 300°C, time 1 hrs. The low coercivity (650 Oe) indicates that cobalt carbide phase did not form. The poor magnetization id related to insufficient source of magnetic material resulted from the low cobalt precursor concentration. | 107 |
| Figure 6.4.2.11 One factor at a time vs the response coercivity H_c in Oe. | 107 |
| Figure 6.4.2.12. Showing change for cobalt carbide nanoparticle with the increase in Ag:Co ratio. From top to down as Ag concentration increase, nanorods are formed and will vary in aspect ratio as Ag concentration increase. | 108 |
| Figure 6.4.2.13. Surface profile showing saddle point for the profile of the effects; Ag, Temp vs the response H_c . The black points represent the design points in the design table. | 109 |

Abstract

Optimizing Cobalt Carbide based nanomaterials by using nucleating agents and statistical routes

By: Turki I. Almugaiteeb, Ph.D.

A dissertation submitted in partial fulfillment of the requirements for the degree of
Doctor of Philosophy at Virginia Commonwealth University

Virginia Commonwealth University, 2016

Director: Dr. Everett E. Carpenter

Professor of Chemistry

The continuous high demand on permanent magnets in industries opened new research plateau to develop alternative magnetic material. The current used permanent magnet materials in the market still suffer from high cost and insufficient magnetic or thermal properties. The central focus of this dissertation work is the optimization of cobalt carbide based nanomaterial by means of modifying polyol synthesis assisted by nucleation agent and systematic statistics using JMP software tool. In most existing literatures, producing cobalt carbide (Co_2C or Co_3C) lack reproducibility and consistency resulting in nonsolid magnetic properties results. The practical requirements for cobalt carbide to be used as permanent magnet are high coercivity (H_c), high magnetization

(M_s), resulting in a high-energy product ($H_c \times M_s$). Previous literatures have shown coercivities of 1.5 to 2.5 kOe for cobalt carbides under aggressive temperatures conditions (300°C) or after aligning the particles under magnetic field.

A statistical guided method performed a sequence of experiments toward producing high coercivities using surface response design. Primarily, the statistical study to optimize cobalt carbide was made by analyzing experimental condition to fulfill high magnetic properties with tuned conditions as much as possible. Therefore, having the advantage for superior control on process variable when shifting cobalt carbide for scale up production in flow chemistry set up using microreaction system (MMRS). The optimization is based upon selecting the most important conditions in polyol reaction to produce cobalt carbide (Co_2C or Co_3C) and feed JMP software model e.g. reaction temperature, reaction time, and or precursor concentration...etc. These factors called (effects) used to design experiments and generate tables to run minimum experiments. Points of each effect (levels) are selected based on previous knowledge and experience with the synthesis. The output called (response) can be any of the magnetic properties of our interest e.g. magnetization (M_s), coercivity (H_c), or energy magnetic product ($H_c \times M_s$). In the first model fit of cobalt carbide magnetic was studied in a polyol reaction to increase its magnetic energy product and optimize the experimental conditions. The results disclosed increase in magnetic energy product (6.2 MGOe) when validating the prediction model conditions suggested by JMP: shorter reaction time, and lower precursor concentration conditions at maximum reaction temperature.

Finally, to my knowledge studying the effect of the nucleating agent to alter cobalt carbide growth have not been studied so far. Therefore, statistical study design

using central composite design (CCD) to investigate the nucleating agent effect of silver nitrite on cobalt carbide coercivity was made. The importance of nucleating agent on coercivity is vigorous to attain and control the growth direction of cobalt carbide nanoparticles. This is due to the shape anisotropy contribution to enhance coercivity unlike weak shape anisotropy attributed to agglomeration of nanoparticles demonstrated in previous studies. Enhancement of coercivity reached 3 kOe with aspect ratio control as a function of silver nitrite concentration under lower reaction temperature.

Chapter 1. Introduction

1.1 Overview

Ferromagnetic materials have been introduced in many industrial applications such as permanent magnets (PM). PM can be utilized in many technologies such as; communication devices, wind turbines and electric vehicles.¹ PM motors have significant advantages when compared to induction motors such as smaller size, lighter weight and higher efficiency.¹ The ability of PM to provide high magnetic properties gives them high efficiency in such applications. The high magnetic properties result from high magnetic energy product or BH_{\max} fig. 1.1.1(a), which is the metric measurement degree of energy stored per unit volume.

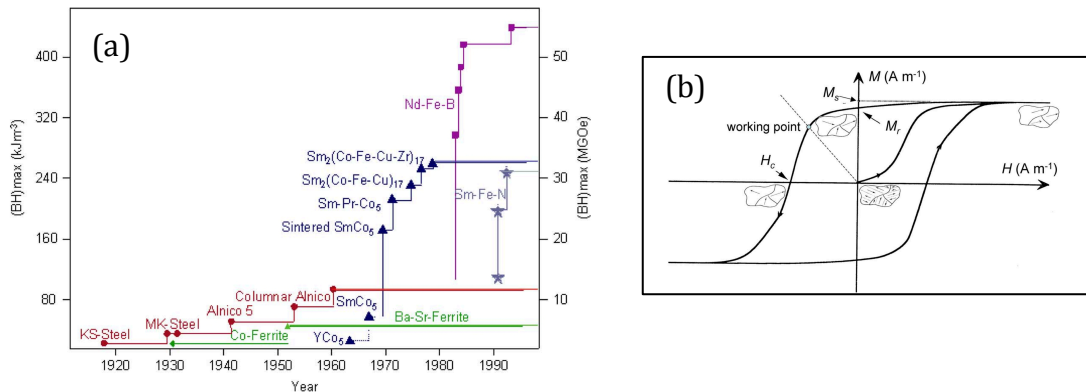


Fig. 1.1.1 Energy product of various permanent magnet materials (a)¹, hysteresis loop for ferromagnetic materials showing coercivity (H_c) and saturated magnetization (M_s) (b).²

The energy product is the outcome of two major components that can be revealed from magnetic measurements; coercivity and magnetization. These two components can be drawn from the magnetic measurements found in the hysteresis loops shown in Fig. 1.1.1(b).² Simply, coercivity can be thought of as the energy required demagnetizing a

magnetized material this resulted from magnetic force needed to bring the magnetic moment to zero.

Thin films are very important in spintronics and memory devices but they are not sufficient in PM applications.² This can be attributed to their incapability to produce the stray field needed outside the material's volume (air gap) in order to be effective for PM motor. The absence of a stray field is related to the demagnetization constant (N) that range between 0 to 1 depending on the shape e.g. N = 1/3 for spheres, N= 0 for needles, N=1 for thin films and other shapes can be approximated by ellipsoids. It is related to the demagnetization field (H_d) equated in linear relationship with magnetization (M_s) as per the below equation;^{1,2}

$$H_d = - N M_s$$

The demagnetization field contribute to reduce the magnetic moment of the material induced by the shape.² The demagnetization field contributes to reduce the coercive field as will through the following equation:

$$H_c = H_d + H_a$$

Where H_c and H_a are the coercivity, and anisotropy field respectively. The anisotropy field depends on crystal structure through the anisotropy constant shown in the below relationship:

$$H_a = 2 K_u / M_s$$

Where K_u is the anisotropy constant, and M_s is the magnetization saturation. The origin of this anisotropy constant (K_u) related to the magnetocrystalline anisotropy linked to the spin-orbital coupling of moment at the easy axis of the PM material.² The easy axis can

be defined as the axis where the magnetization lies within the same direction and can be switched at coercive fields.²

1.2 Ferromagnetism

1.2.1 Ferromagnetic material and basic properties

Basically, PM materials are divided into two types; 1) rare earth (RE) PM based materials, e.g. Sm_xCo_y and $\text{Nd}_2\text{Fe}_{14}\text{B}$ 2) RE-free materials that either can be steel based alloys or ceramic ferrite magnets. The high energy product in RE materials is attributed to the high magnetocrystalline anisotropy energy (MAE).² Magnetocrystalline induced by the doping of RE elements in transition metal crystals.^{1,2}

This high operating MAE for RE permanent magnets causes an increase in the coercivity. The potential of manipulating different chemical composition of rare earth materials gave significant enhancement to RE PM materials (BH_{max}) between 1970 to 2000 fig. 1.2.1.1(a).^{1,2} The problem with RE based PM materials is the high cost due to the high demand and the lack of resources recently recorded in fig. 1.2.1.1(a). The light blue bars in the chart of fig. 1.2.1.1(a) show the sales in dollars increasing exponentially with the fast growth for Neodymium-iron-boron (Neo) magnets. The estimation accounted for the years between 2010 and 2020. In 2011 there was a spike of demand for Nd fig. 1.2.1.1(a), which gave an attentive to industries to start looking for new alternative materials. While the sales were 8 billion dollars for all permanent magnetic materials during 2005, it is expected to jump to 17 billion dollars for Nd by 2020 as per fig. 1.2.1.1(a) if there is adequate supply of raw materials for Nd.

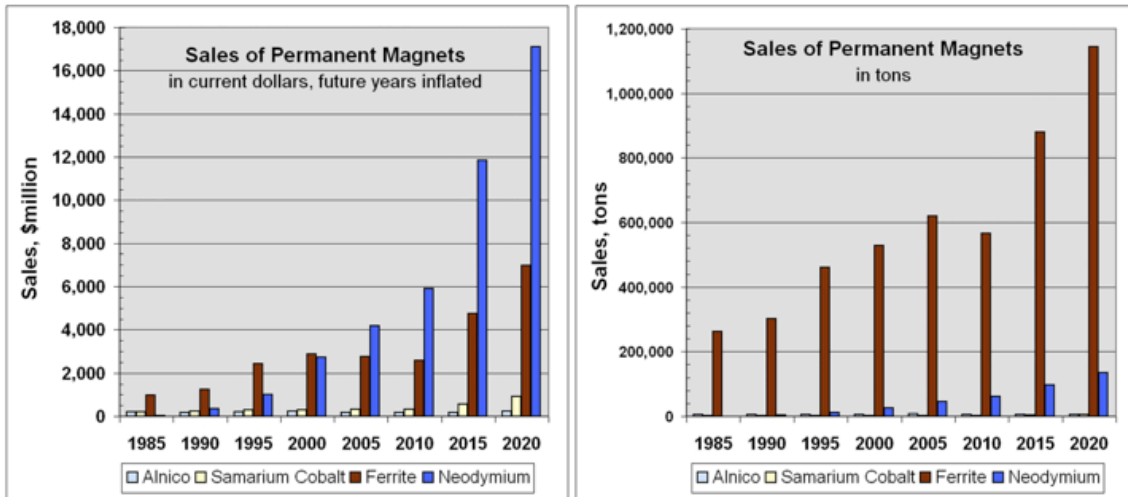


Fig. 1.2.1.1 Permanent magnet sales by US Dollars also by metric tons for the largest current used materials. (a) Show the sales in dollars while (b) show the sales in tons.³

In terms of raw materials fig. 1.2.1.1(b) shows an increase in the demand in tons.³ Current RE-free PM magnets can be divided into; 1) ceramic ferrite magnets and 2) steel based alloys. The ceramic ferrites PMs are ferrimagnetic material with two opposite magnetic sublattices have a hexagonal structure nature. The ceramic name is given to materials composed of iron oxide combined chemically with additional metallic. Unfortunately the hexagonal ferrites do not have much magnetization due to the non-magnetic component of oxygen ions. For example the magnetization at room temperature for $\text{BaFe}_{12}\text{O}_{19}$ or $\text{SrFe}_{12}\text{O}_{19}$ is 380 kAm^{-1} , which is less than that of iron.² The steel based PM materials basically alloys containing Nickel, Aluminum and Cobalt and they can be referred as Alnico magnets. This material was first developed in the early 20th century. Other forms of alnico can be two phases allows nanostructure of CoFe, the anisotropy is due to shape anisotropy.² Thermal magnetic capabilities are important in PM motors technology. The importance of this characteristic is defined by the Curie temperature

(T_C); where ferromagnetic material start to loose its properties and turn into paramagnetic material resulting in reduction of BH_{max} . For example, SmCo showed high thermal magnetic properties opposed to NbFeB, which is important in PM application as shown in table 1.2.1.1 for PM materials.²

| material | T_C (K) | M_s (MA m ⁻¹) | K_1 (MJ m ⁻³) | $ BH _{MAX}$ (kJ m ⁻³) |
|---|-----------|-----------------------------|-----------------------------|------------------------------------|
| Alnico 5 | 1210 | 1.12 | 0.68* | (310) |
| BaFe ₁₂ O ₁₉ | 740 | 0.38 | 0.33 | 45 |
| CoPt | 840 | 0.80 | 4.9 | 200 |
| FePt | 750 | 1.14 | 6.6 | 406 |
| SmCo ₅ | 1020 | 0.86 | 17.2 | 231 |
| Sm ₂ Co ₁₇ | 838 | 0.97 | 4.2 | 294 |
| Nd ₂ Fe ₁₄ B | 588 | 1.28 | 4.9 | 512 |
| Sm ₂ Fe ₁₇ N ₃ | 749 | 1.23 | 8.6 | 473 |

Table 1.2.1.1. Showing intrinsic magnetic properties of different PM materials.²

The low Curie temperature of NbFeB didn't drop down the demand on this material for the use in PM technology as per fig. 1.2.1.1 (a) since its traded with the high-energy product ever recorded (512 kJm⁻³) table 1.2.1.1. Unalloyed materials suffer from having good high temperature performance; the low Curie temperature can be overcome by the substitution of cobalt which has the highest Curie temperature of any material 1360K compared to iron 1044K. Unfortunately, cobalt will add up more in the cost of producing this material in addition to neodymium. This substitution produces reduction in the anisotropy of the tetragonal 2:14:1 structure. Other materials can be substituted to increase anisotropy are: terbium or dysprosium but their high cost will still not make

them practical to use in PM technology compared to iron and niobium. The substitution will produce a slight increase in Curie temperature but at the expense of reducing magnetization because a heavy RE couples antiferromagnetically with iron.²

Developing new materials was carried out during the 90's by using iron-based intermetallic to increase Curie temperature. This is done by interstitial modification to tune crystal field. The process produced $\text{Sm}_2\text{Fe}_{17}$, an iron-rich intermetallic with remarkable Curie temperature 389K. The introduction of nitrogen with three atoms transformed the properties to occupy a triangle of interstitial sites around samarium. As a result an increase in the unit cell to 6% was observed elevating the Curie temperature to 360K. The draw back of $\text{Sm}_2\text{Fe}_{17}\text{N}_3$ is the problem with sintering into fully dense oriented magnet due to the escape of nitrogen at high temperatures causing reduction in magnetic properties.²

1.2.2 Ferromagnetism; theory and background

The basic theory of ferromagnetism started fifty years ago with EWING's theory, which was one of the first attempts to explain ferromagnetism. EWING and Weber assumed that each atom by itself is a permanent magnet and can rotate in any direction about its center. Magnetic forces are the main cause of the orientation of various magnets with respect to the magnetic field.⁴ Ewing theory discarded other forces in his model, which only maintain the dipole moment of neighboring parallel atoms. These are the electrostatic forces of exchange that Heisenberg proposed which are strong enough to align the elementary magnets against the strong disordering effect of thermal agitation. Roughly the magnetization corresponded energy was estimated from the energy of

thermal agitation at the Curie point. The Weiss theory explains how the atomic forces persuade ferromagnetism introduced by the molecular field theory associated with the nature of these forces. Weiss theory is extension to the classical theory of paramagnetism developed by Langevin. This is based on the behavior of collective of elementary magnets (atoms), each of moment μ_A , in a field of strength H . The field will provide the alignment of the moments while the thermal agitation effect will destroy this alignment.

The outcome of the quantum theory of magnetism supplies a natural unit of magnetic moment equal to the magnetic moment of a single electron spin (*Bohr magneton*) $\beta = eh/4\pi mc = 9.27 \times 10^{-21}$ erg/ gauss.

In general the magnetic moment is due to the electron spin and the orbital motion. So that the relationship of magnetic moment is equated as per the following equation:

$$\mu_A = J g \beta$$

The moment can be resultant from each factor individually for example if it is due to the spin electron alone the g-factor (g) dimensionless constant in the equation will be 2 if it is due to orbital motion and will equal to 1; almost all ferromagnetic materials moment is due to electron spin.

1.2.2.1 The Stoner-Wohlfarth (SW) model for ferromagnetism:

The SW model describes the physics of fine magnetic grain, and magnetization. This model can be called the hydrogen model for ferromagnetism since it is the basic theory to explain ferromagnetism. The understanding of the SW model is crucial to gain physical behavior knowledge of magnetic particles when they reach single domain limits

also it can explain the magnetic properties associated with nanoparticles. Some examples of FM materials SW model can explain the properties shown in table 1.2.2.1.

| Unit Material | (K) T_c | (G) M_s | 10^6 (erg cm ⁻³) K | (nm) l_{ex} |
|-------------------|--------------|--------------|---------------------------------------|------------------|
| Fe | 1044 | 1710 | 0.48 | 2.8 |
| Co | 1398 | 1440 | 5 | 3.4 |
| Ni | 627 | 485 | -0.057 | 9.9 |
| Permalloy | 720 | 795 | 0 | 5.7 |
| CrO ₂ | 393 | 397 | 0.22 | 3.2 |
| SmCo ₅ | 993 | 835 | 170 | 7.4 |

Table 1.2.2.1.1. Properties of some ferromagnetic materials: T_c the curie temperature, K the anisotropy constant, M_s per unit volume saturation magnetization, and l_{ex} is the exchange length; that can be compared to domain wall thickness, where; $l_{ex} = \sqrt{A/K} =$ and A is the exchange stiffness.⁵

When applying a magnetic field to an FM material the magnetization M will change, this change is governed by the change in the external magnetic field H . To understand this phenomena plotting the value of the magnetization M projected along the direction of the applied magnetic field H . The point where the magnetization M changes with the change in magnetic field H in the M - H plan is the hysteresis loop shown at fig. 1.2.2.1.1. The term hysteresis; (delay in Greek), means that the material is cycled by the field when it increase then decrease in two different non-overlapping curves occur and $M(H)$ obtained.⁵

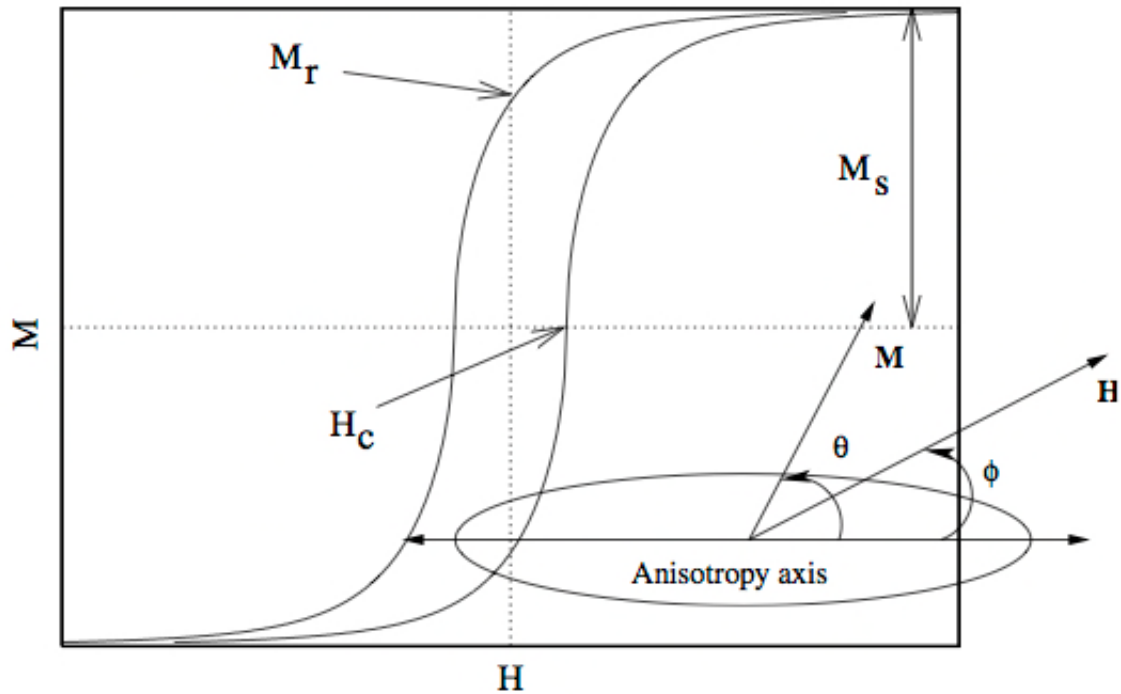


Fig. 1.2.2.1.1. Single domain hysteresis loop obtained for an arbitrary angle, ϕ , between the magnetic field and the anisotropy axis. Important magnetic quantities such as coercivity H_c , and remanent magnetization M_r , depend on ϕ whereas intrinsic saturation magnetization M_s does not depend on.⁵

The hysteresis loop will reveal important magnetic characteristics; saturation magnetization (M_s) which is attained when all magnetic moments are aligned along a common direction which is called easy axis resulting in the largest value of the magnetization and no more increase in magnetization can be revealed, the remanent magnetization (M_r) is the leftover magnetization known also as the memory of the magnetic moment after removing the magnetic field and the coercive field (H_c) is the field at which $M = 0$. Coercive field (H_c) can be defined, as the energy required forcing the spins in magnetic moment resulting in zero net magnetic moment. The input output delay is related to the width of the loop, which in turn defined by the quantity of the ratio between M_r/M_s (squareness). When the ratio is close to 1, it will indicate that the field is close to an orientation known by the easy axis (EA) whereas the hysteresis loop is closest

to a square shape. This means that most magnetic moments are in mutual direction with the external magnetic field. The squareness in the hysteresis demonstrates that material will exhibit a cubic anisotropy having many easy axes. However, when quantity of the ratio between M_r/M_s is below 0.7, it indicates that the material exhibit uniaxial anisotropy means it has only one easy axis as energetically favorable direction for spontaneous magnetization.

The angle (ϕ) made between the magnetic field and the EA is fundamental for magnetic characteristics in the hysteresis loop. For instance when the angle ϕ is high, the opening of the hysteresis loop will be reduced which requires a high magnetic field to saturate the magnetic moments in the hard axis. Most characteristics of hysteresis loop shown in fig. 1.2.2.1.1 for a given temperature and frequency of the applied magnetic field show that magnetic quantities such as remanant magnetization M_r and coercive field H_c depend on the angle ϕ .^{2,4,5} The hysteresis loop shape will change when varying temperature and magnetic frequency; the hysteresis loop branches will possibly collapse together in a single curve if the Curie temperature (T_c) reached, and the material will becomes paramagnetic.⁵ This magnetic phase will loose the ferromagnetic properties including stray field that is important for PM motor applications.²

One of the key considerations to attain increase in coercivity is either by enhancing; shape anisotropy, magnetostatic interaction or and magnetocrystalline anisotropy.⁴ The detailed of magnetocrystalline anisotropy and shape anisotropy will be explained in in the following sections.

1.2.2.2 Nanomagnetism

Interatomic distance and atomic structure play major role to vary the magnetic behavior of a ferromagnetic material. This involves important role in magnetic exchange energy which is energy between two unpaired electrons resulted from the magnetic moment of their interaction. The variation in magnetic exchange energy is a function of interatomic distance shown at fig. 1.2.2.2.1 and changes in the interatomic distance will dictate the magnetic behavior. When the magnetic exchange energy quantity is negative the material will be expected to have antiferromagnetic behavior e.g. Mn, and Cr as per fig. 1.2.2.2.1. Once the exchange magnetic energy is positive the interatomic distance governs the strength of ferromagnetic material as per fig. 1.2.2.2.1.⁶ This change in the magnetic exchange energy with interatomic distance elucidates the importance of the size effect in magnetic nanomaterials. Basically, the changes in magnetic properties at atomic scale attributed to the high atomic surface to volume ratio.^{2,7-11}

From chemistry of material basics the ferromagnetic behavior is a form of paramagnetic material elucidated by the extended long-range order between unpaired electrons in paramagnetic material. The fact that magnetic moment strength is based on the collective spins in material making it a volume dependent will make size very important.

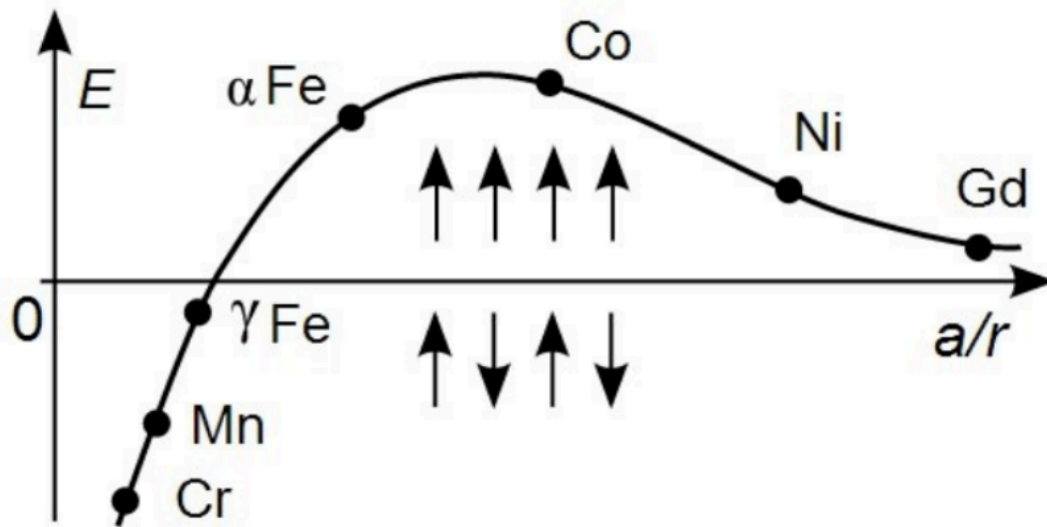


Figure. 1.2.2.2.1. Graph shows the exchange energy vs the atomic over radius of many crystalline metals. If the value of E is positive the material will be ferromagnetic while if it is negative this predict an antiferromagnetic behavior.⁶

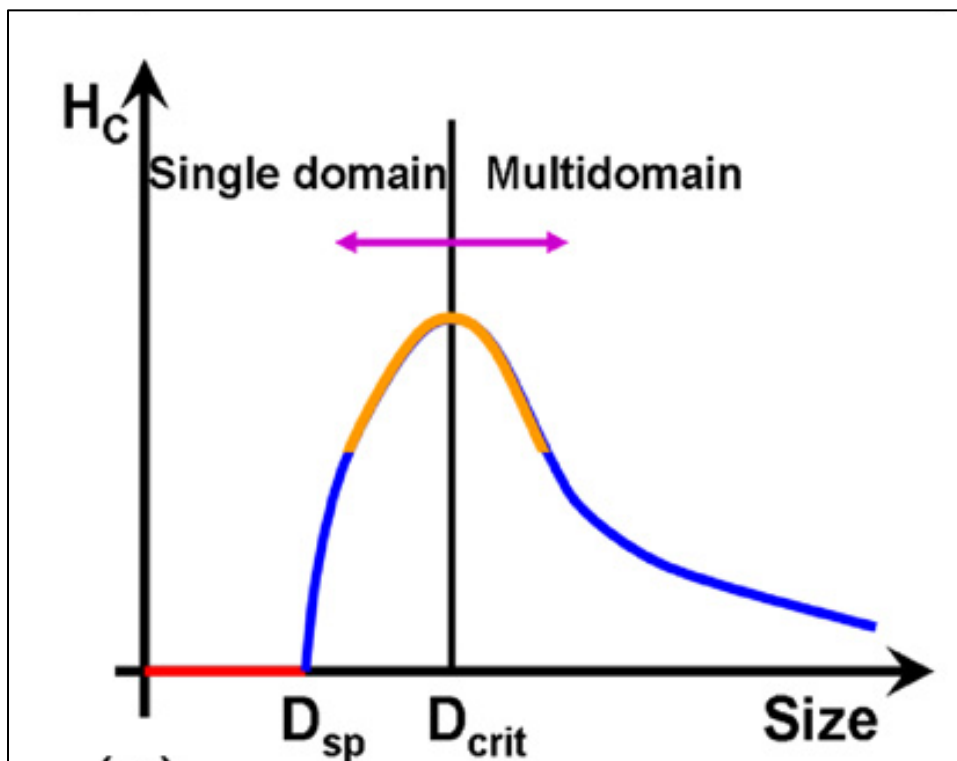


Fig. 1.2.2.2.2. Increase in coercivity when reaching critical size.¹²

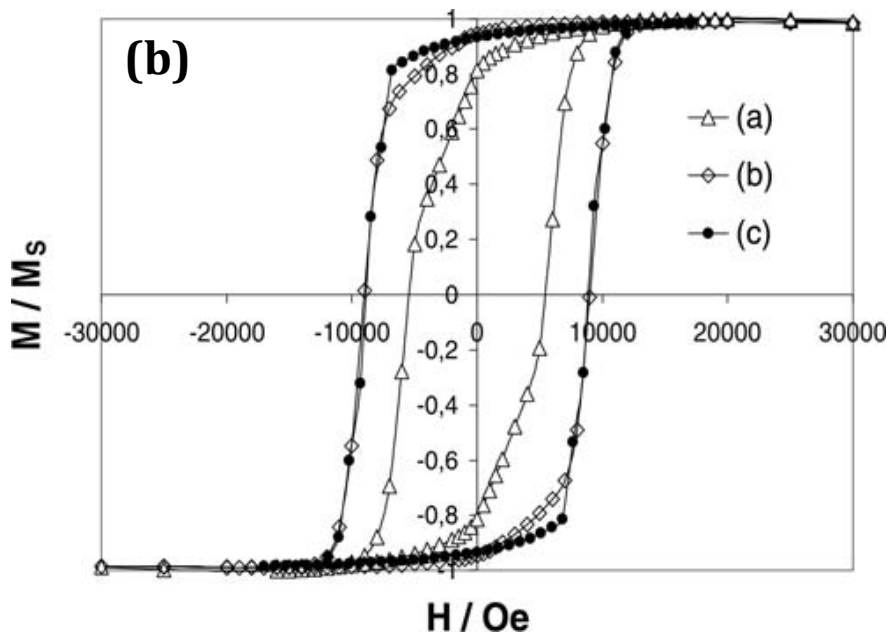
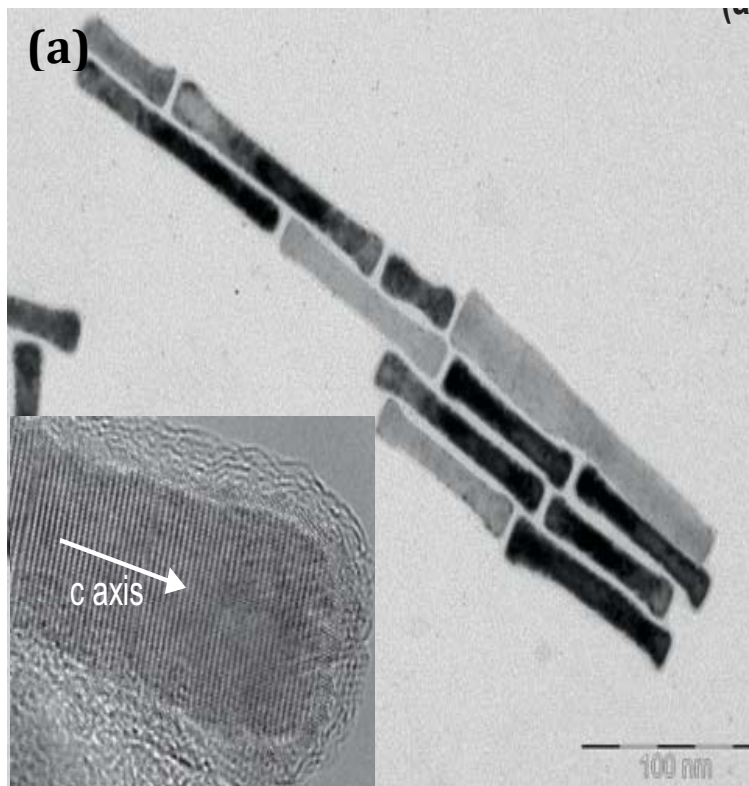


Fig. 1.2.2.2.3. (a) TEM images of Cobalt nanowires produced by introducing RuCl_3 in polyol media (b) Hysteresis a) at room temperature showing coercivity of 4.5 Oe b) Hysteresis of the sample in toluene at 150K c) Simulation of the frozen sample magnetization curve using Stoner-Wolfarth.^{13,14}

The bell shape curve of coercivity as a function of particle size at fig. 1.2.2.2.2 demonstrates the critical size effect on coercivity. At critical size the particle display high coercivity. Critical size can differ from one material to another.^{6,15-17} The critical size will be the intermediate between single domain (superparamagnetic limitation) and multi domain (paramagnetic and ferromagnetic).¹⁸

Domain theory explains the mechanism of rearranging the magnetization in a material with respect to external magnetic field in subdivided regions called *domains*. Magnetization normally distributed uniformly in a ferromagnetic material but it will vary from one domain to another and separated by *domain wall*.¹⁹ A single domain occurs when size of the grain is smaller than some critical length containing 10^{12} – 10^{18} atoms for cobalt nanoparticle case.⁵

Controlling the particle size of cobalt nanoparticle reaching the domain size changes the magnetic properties resulting in coercivity enhancement at room temperature when producing immiscible Au@Co core-shell nanoparticles. The core-shell Au@Co particle forces the magnetic spins to be aligned together increasing the blocking temperature. Surprisingly the enhancement in magnetic properties is viable even with the presence of atomic non-ferromagnetic species such as gold. The increase in coercivity suggested to be attributed to the magnetic pinning behavior and the nature of the interaction at the interfacial between cobalt and gold. The magnetic pinning will be explained in more depth at following section.¹⁰

Ferromagnetism material assets enhancement attained by controlling magnetic anisotropy. This is accomplished by assembling magnetic anisotropic particles related generally to one of following parameters: (i) particles distribution oriented on the easy

axis in the presence of external magnetic field, (ii) the particles shape.²⁰ This is conceived by directing the growth of the particles on the easy axis plane resulting in an increase in coercivity.¹³

Capping agents such as Trioctylphosphine oxide (TOPO) and Oleic acid can block the growth by controlling the molar ratio of 6.3:1 to produce soft magnet (50 Oe) iron Oxide nanowires (NW) through the thermal decomposition of the iron oleate in 1-octadecene.²¹

Cobalt nanowires shown at fig. 1.2.2.2.3(a) produced in a different fashion by introducing RuCl_3 as nucleating agent in a polyol process to reduce cobalt laurate in 1,2-butanediol resulting in high coercivity (4.5 kOe) at room temperature fig. 1.2.2.2.3 (b).¹³

1.2.2.3 Magnetic anisotropy

The importance of high magnetic anisotropy comes from the ability to overcome thermal effects resulting in superparamagnetic inhibition. There are several types of magnetic anisotropy that are considered to enhance magnetic material anisotropy; i) magnetocrystalline anisotropy (e.g. CoPt and CoFe alloys); ii) Exchange anisotropy of ferromagnetic/antiferromagnetic core-shell particle; iii) shape anisotropy of magnetic particles such as rods and wires.²²

1.2.2.3.1 Magnetocrystalline anisotropy

The mechanism of magnetic exchange energy between spins with the hosting lattice crystal is called magnetocrystalline anisotropy. Interaction between the moments

themselves or with the hosting crystal is stimulated by the symmetry of the crystal. This gives the rise to anisotropy energy contributions. Spin-orbit coupling is the dominant mechanism in magnetocrystalline. As a result of this coupling mechanism the electronic orbitals are tied to some extent to the electronic spin and will follow their orientation under magnetic field.¹⁹

1.2.2.3.2 Shape anisotropy

Shape anisotropy is as important as the magnetocrystalline but originated from the magnetostatic energy. Shape anisotropy is originated from the magnetostatic energy, which vary with shape. For example, ellipsoidal shape possesses higher magnetostatic energy due to the high uniform magnetization. A magnetized ellipsoidal shape will produce magnetic charges or dipole at the surface. These distributed charges on the surface will act as another source of magnetic field called demagnetization field. It will act as opposition to the magnetization field that produced it, creating surface pole distribution. Shape anisotropy will be more prominent in nanoparticles than in larger size particles ($\approx > 20\mu\text{m}$). Since the magnetic dipolar anisotropy interaction is long range and is shape dependent, the shape anisotropy is significant.¹⁹

Cobalt nanorods shape reported higher coercivity (4.5 kOe) than other cobalt nanoparticle shapes at room temperature. Ru was used as nucleating agent to provide heterogeneous growth. Cobalt nanorods were produced demonstrated at TEM images at fig. 1.2.2.1.3. (a).^{13,22}

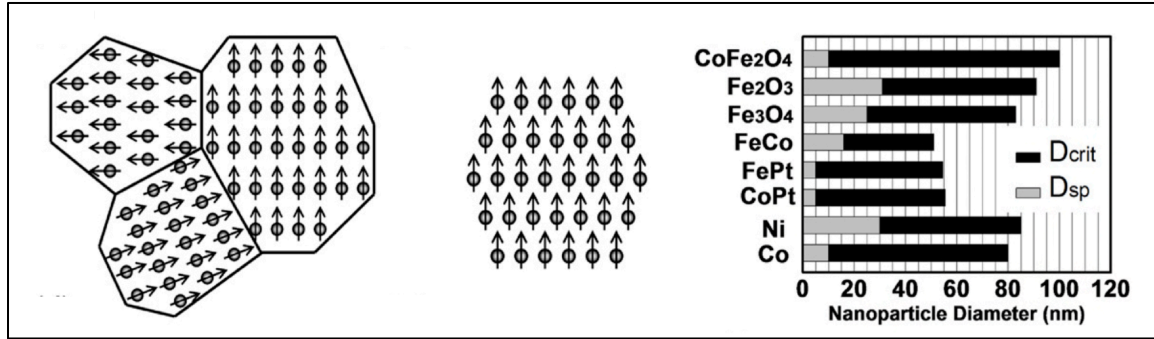


Fig. 1.2.3.1. (a) On the far left show magnetic single multi domain structure in a bulk material (b) Show magnetic single domain structure for nano particles. (c) Critical size of single domain and superparamagnetism of several materials.¹⁵

1.2.3 Magnetic nanocomposites (MNCs)

Magnetic nanocomposites (MNCs) are combination of magnetic nanoparticles (MNPs) and other component that displays multi novel properties along with MNPs. The magnetic component in the MNCs will give it the ability to respond to an external magnetic field without physical contact, making it applicable for remote sensing. The additional magnetic properties from controlling the size from bulk to nano size and control of other non-magnetic i.e. noble metal component provide dual properties like gold@cobalt core-shell offering both surface plasmon resonance and magnetic properties. As a result of particle size control high coercivities reached for MNPs, this is obtained when the particle size is smaller than the critical size D_{crit} shown at fig. 1.2.3.1 (c). Basically this will require transformation of multidomain particle fig. 1.2.3.1 (a) to single domain particles fig. 1.2.3.1 (b). By further reduction in size, coercivity can reach zero eventually when reaching SP limitation size. Superparamagnetism is a unique property of single domain MNPs, determined by temperature, size, and measurements time. This

unique phenomenon can be observed when applying magnetic field at room temperature at 100 s measurements time to a particle size smaller than critical size D_{crit} to give a closed hysteresis loop.¹⁵

1.2.4 Magnetic Pinning:

Magnetic pinning is compromised by the domain wall mechanism as a result of domain wall pinning at the interfacial between two different magnetic species. As the size of the magnetic nanoparticles decrease the domain wall population decrease. The mechanism of the wall motion delimits the favorable wall orientation resulting in reversal magnetization under external magnetic field. The nature of the impediments in wall motion determines coercive field. In some cases impediments observed at wall motion changes with different domain topologies. The impediment in wall motion (wall pinning) rises from structural disorder in domain wall that is attributed to one of the following; presence of randomly distributed residual stresses, nonmagnetic material or grain boundary.¹⁹

There are three common mechanisms used in to explain high coercivity in permanent magnet materials e.g. NbFeB alloy, pinning mechanism that result in high coercivity shown at fig. 1.2.4.1 may be due to; interaction between domain walls and domain defects including atomic disorder, or interaction between grain boundaries, or boundaries between different phases.^{16,23,24} Exchange hardening is responsible for the high coercivity when a nucleation field occur as a result of exchange coupling between the hard and soft phases in a nanocomposite material.²³ High coercivity reported for $Nd_{60}Fe_{30}Al_{10}$ bulk amorphous alloy studied and explained by two mechanisms; magnetic interaction and

wall domain magnetic pinning. Magnetic interaction is related to annealing temperature, and wall domain pinning was less observable during crystallization process.^{16,23} Magnetic interaction was investigated during annealing $\text{Nd}_{60}\text{Fe}_{30}\text{Al}_{10}$ to give more understanding on the coercivity mechanism. $\text{Nd}_{60}\text{Fe}_{30}\text{Al}_{10}$ annealed at 655K – 725K to study hysteresis at different temperatures fig. 1.2.4.1 show as-cast sample coercivity 3.5 kOe and start decay as annealing temperature increased. Investigations propose that increase in temperature promote magnetic interaction and its more pronounced as the crystal size reaches domain size. Therefore, domain wall pinning increases coercivity.^{23,25}

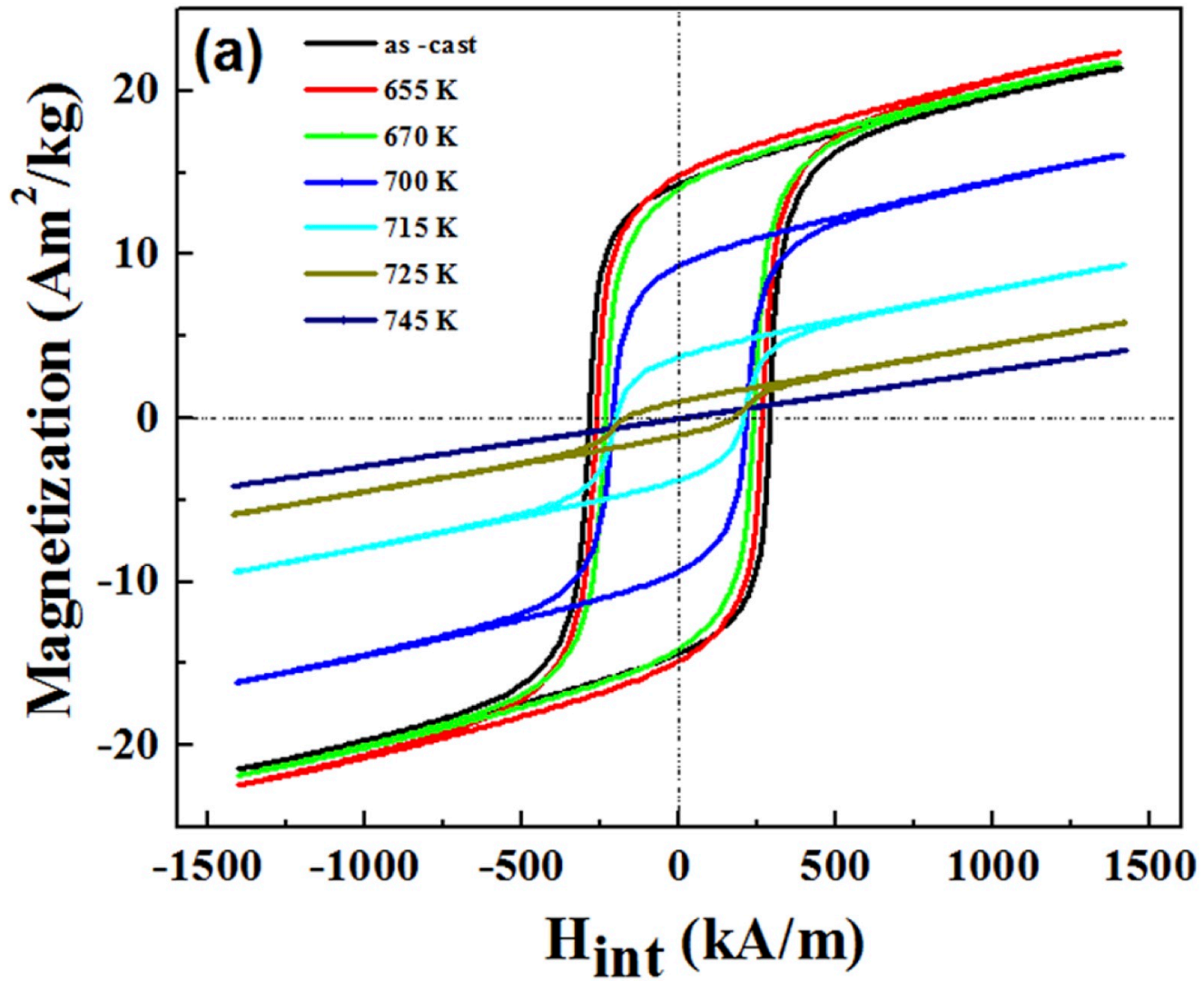


Fig. 1.2.4.1 Hysteresis of NbFeB at different annealing temperature.²³

Chapter 2. Microreactor

2.1 Introduction:

Microreaders are significant technology for nanoparticles production and as application for proven synthesis. They are important tools for optimizing and studying chemical reactions. As a result of their small length and small reaction volume, their heat transfer is improved as well as their narrow size distribution.²⁶

Microreactor technology has been emerged for quantum dot synthesis. Microfluidic studies have been done on nanocrystals synthesis. The concentration on quantum dot (QDs) in microfluidic approach is due to the ability to produce it in confinement space. An important attractive feature of the microfluidic technology is its great simplicity whereas emerging a coil in a hot oil bath did the early reactors. The technique of microfluidic was successfully applied to synthesis various materials; metals, metal oxides, and compound semiconductor nanoparticles. These successful techniques included the production of CdSe, InP, Au, Ag, Co, TiO₂, SiO₂, Fe_xO_y.²⁷

2.2. Microfluidic types:

2.2.1 Capillary microfluidic type

The first type introduced here is the capillary microfluidic type of a broad channel of inner diameter of 100-1000 μm where the precursor solution is injected under pressure and pumped to an emerged oil bath section. A typical set up shown at fig. 2.2.1.1 for microfluidic to synthesis CdSe QDs. Two syringe pumps were used to host two solutions of cadmium and selenium separately and pump them under pressure into separate

capillaries. The two solutions will be mixed in a convective mixer to ensure chemical homogeneity after passing by the two in one Y-shaped junction.

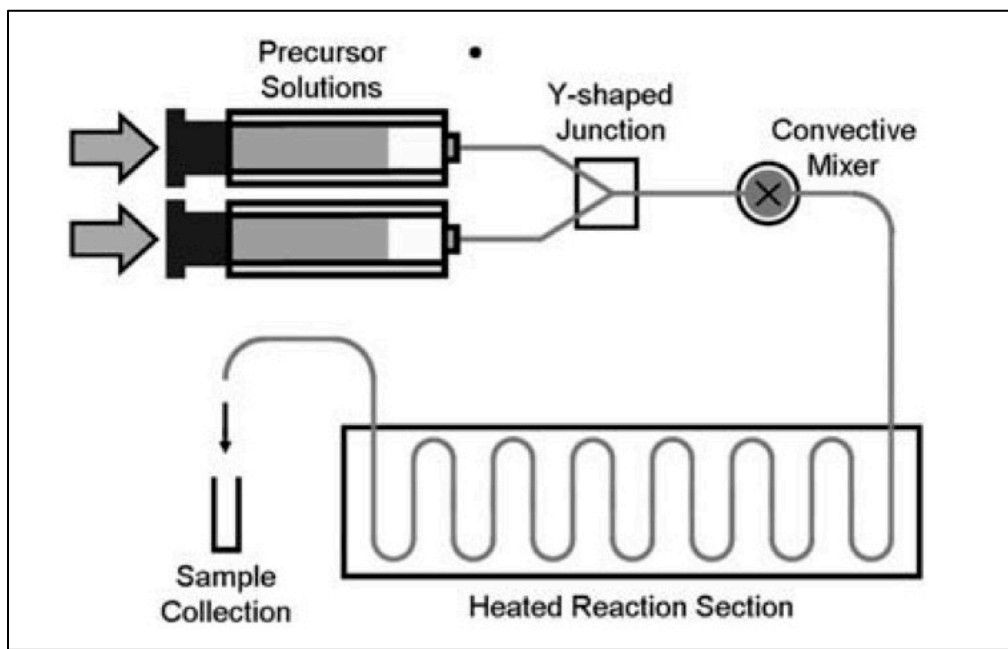


Fig. 2.2.1.1. Capillary reactor schematic used to synthesis CdSe QDs. The precursor solutions were pumped in a Y shaped junction to be mixed in a convective mixer before entering the heated PTFE tubing where nucleation and growth occur.²⁷

The final product will be collected in the capillary outlet. The capillary made from polytetra fluoroethylene (PTFE), which is common, choice and inert in reaction and can sustain high temperatures without degradation.²⁶⁻²⁸ This simple system was successful to produce many other materials due to the ease ability to control the final product. The reaction time is one parameter that can be easily controlled by varying the flow rate or by changing the capillary length. This is done while fixing the concentration ratio of cadmium to selenium in order to control reagent composition over changing the resident time.^{27,29}

The control of kinetic energies through microfluidic lead to producing all three crystal structures of cobalt: hcp, fcc, and epsilon ϵ . This is achieved by controlling; time, flow rate, and quenching procedure.³⁰ Cobalt nano particles controlled by flow rate with immediate quenching procedure using acetone at the outlet. At fig. 2.2.1.2 TEM showed at 0.9 ml/min particle size of 3.9 nm with fcc crystal structure while at 0.08 ml/min particles size was 3.5 nm with hcp crystal structure, and investigating quench effect at the same flow rate with no quench particle size was 4.7 nm with epsilon crystal structure ϵ .³⁰

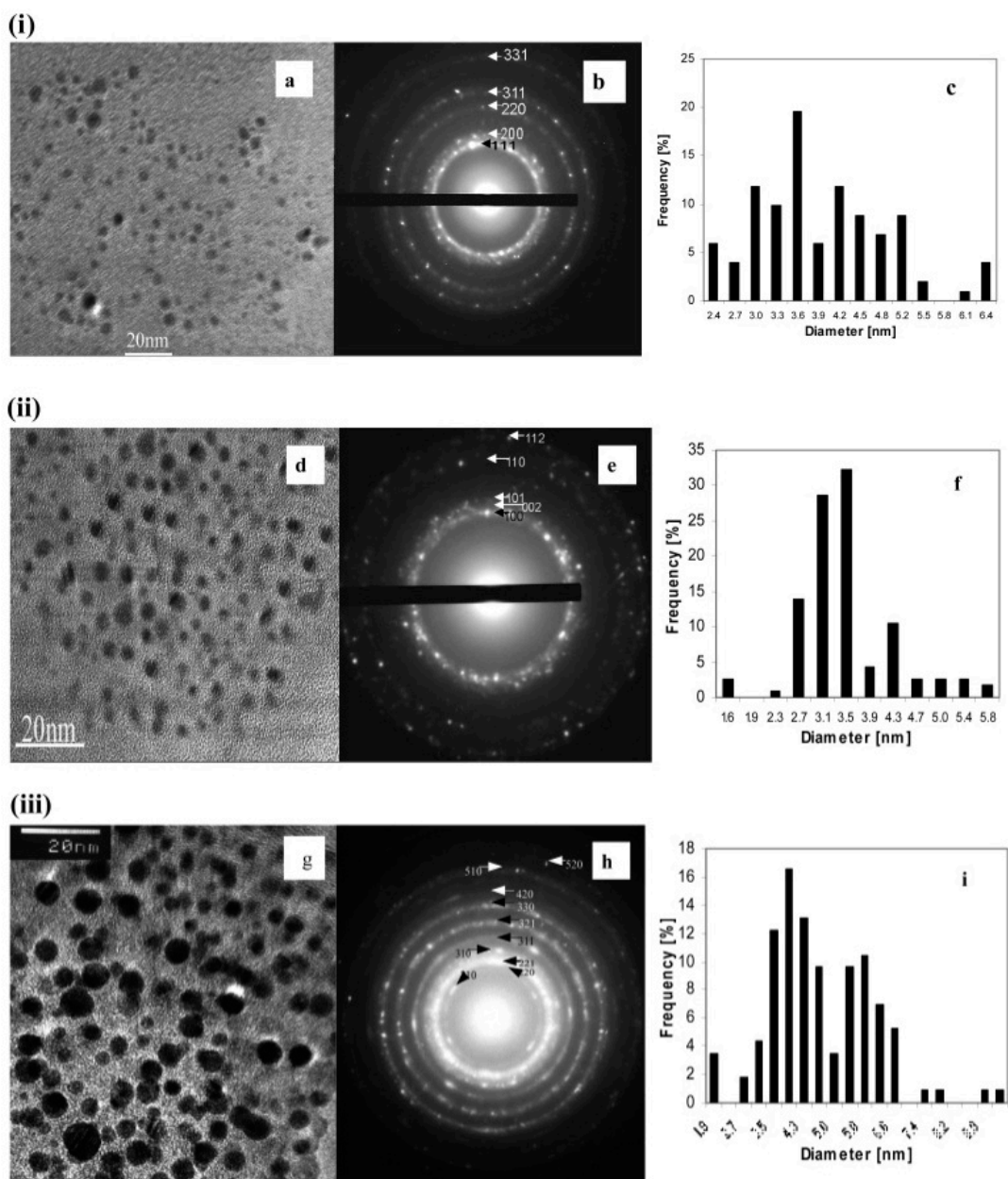


Fig. 2.2.1.2. TEM images for; (a-c) fcc cobalt nanoparticles 3.6 nm obtained at flow rate of 0.9 ml/min and quenched at the outlet of the microfluidic reactor. With diffraction ring image showing the crystal structure, (d-f) show hcp cobalt nanoparticles of 3.5nm produced at flow rate of 0.08 ml/min, and (g-i) show spherical particles of epsilon crystal structure ϵ with an average size of 4.7 nm.³⁰

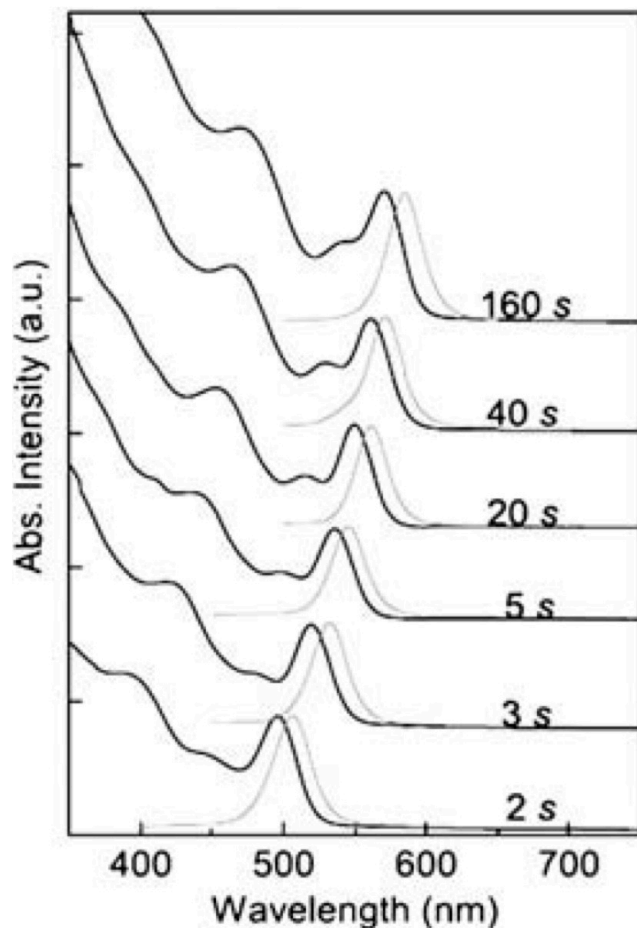


Fig. 2.2.1.3. Absorption and emission spectra of CdSe nanoparticles synthesized at 280°C with different resident time.²⁷

Fig. 2.2.1.3 shows the changes in the absorption and emission for different resident times when reacting CdO and selenium in octadecene, oleic acid and oleylamine used as ligands for Cd and trioctylphosphine (TOP) as the ligand for Se. The organic ligands will stabilize surface atoms to control the growth mechanism of the CdSe QDs. As per fig. 2.2.1.3 the shift in the spectra is observable as resident time increased. The extremely high emission spectra for the uncapped CdSe with narrow line width as per fig. 2.2.1.3 indicate highly particles monodispersity. At longest resident time 160 sec a TEM image

shown at fig. 3.2.1.4 for a spherical particles formed with a narrow size distribution of 3.6 nm.²⁷

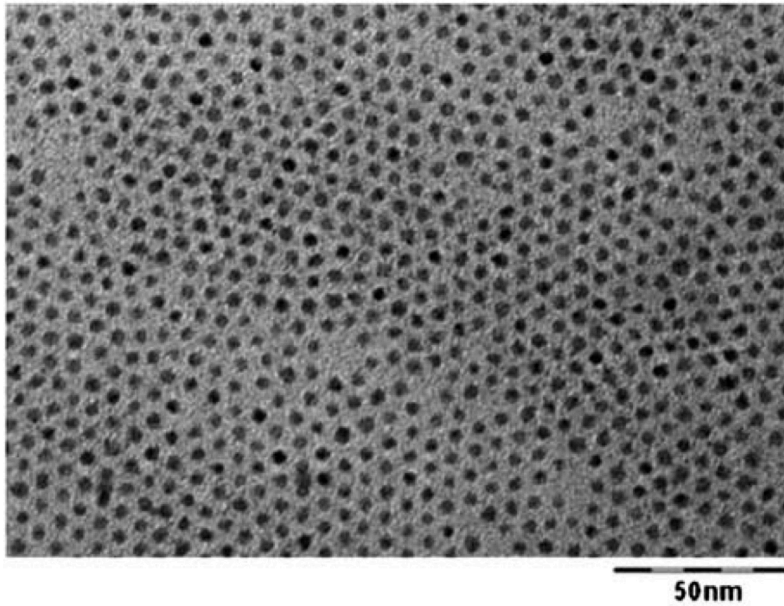


Fig. 2.2.1.4. TEM image of 3.6 nm CdSe produced in microfluidic reactor within 160 s resident time.²⁷

This is one of great advantages of microfluidic reactor more control on particle size and monodispersity. The very narrow size distribution results in very sharp peak in the first exciton. This is linked to the differences in band gap between different sized particles. As a result of small particle size most of the electrons they will get excited over a smaller range of wavelengths. We conclude that the narrower size distribution, the higher exciton peaks that can be seen clearly.^{27,28}

2.2.2 Microfluidic chip type

Another type of microfluidic technology is one used a chip to house channels shown in fig. 2.2.2.1, which have the same width of the first type (100-1000 μm). These microfluidic chips are made form glass, silicon or plastics. Polydimethylsiloxane (PDMS)

is common material used for low temperature synthesis as it allows for rapid chip fabrication.²⁹

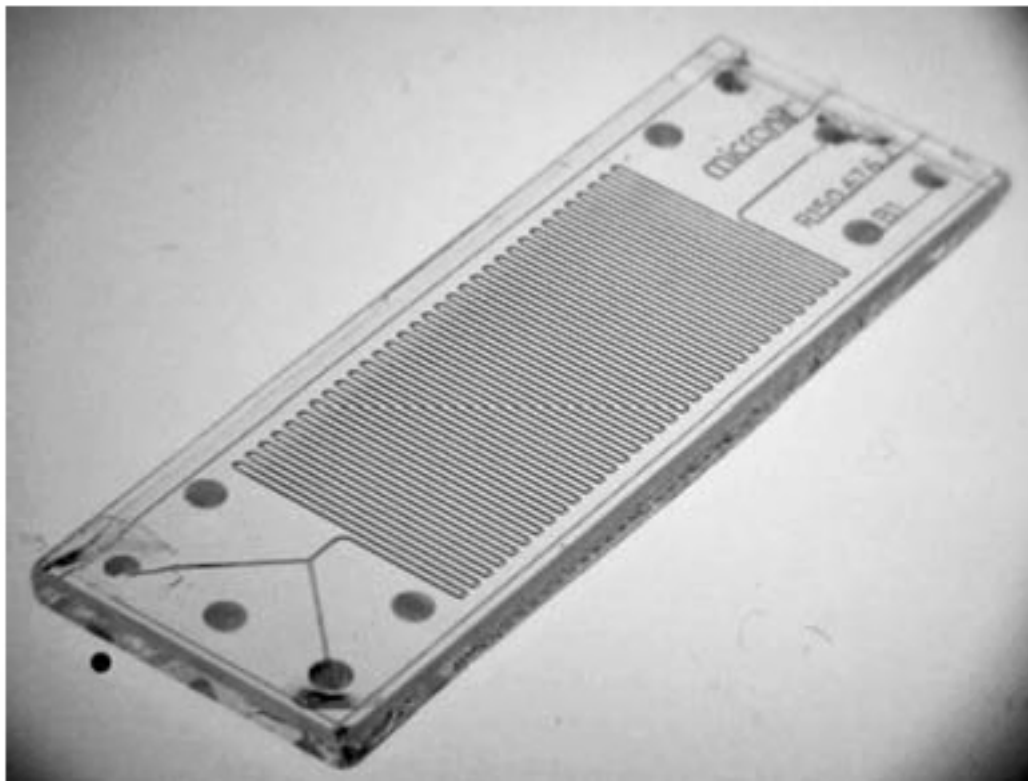


Fig. 2.2.2.1. Microreactor made of glass fabricated by Micronit for typical use for quantum dot synthesis.²⁷

In other high temperature reactions for high quality QDs, glass or silicon chips can be possibly fabricated by standard photolithography. These materials displayed excellent chemical and thermal stability. Fig. 2.2.2.1 shows a typical dual inlet/single outlet microfluidic chip including circuitous channel for QD growth. The heating process is done either by placing the chip on a hot plate or by connecting the chip with localized heaters. The advantage of microfluidic chip over the capillary microreactor is the ability to tailor the chip geometry channels during fabrication so that it suits the reaction requirements also provide multiple chemical processing steps simultaneously such as heating cooling and mixing, etc. that can all be combined in a chip.^{27,29,31}

Among the challenges when synthesising nanoparticles in microfluidic reactors of any kind two main important challenges should be considered:

2.2.2.1. Solvent selection:

It is important to select a solvent that will not only be liquid at room temperature thus making it easy to deliver the solvent from the pumps into the microfluidic channels but also at high temperature (>200°C) required for the synthesis. This consideration will rule out the high viscos from long chain ligands used in patch reactions.³² Still the use of TEG is indispensable in order to produce cobalt carbide.^{17,33} Surface science will play important role during the change in solvent's viscosity nature as temperature changes. Whereas at high temperature TEG compatibility and viscosity will change and start interact with the adhesion forces with the microreactor walls. When carrying cobalt carbide reactions within MMRS; TEG was diluted in Ethanol with a ratio of 4:1 to control viscosity at high temperatures and avoid turbulent flow.

2.2.2.2 Reaction system selection:

The synthesis system selection including solvents, reagents, and reaction condition is very vital in order to avoid any possible precipitation of nanocrystals in narrow channels, which put the reaction in risk of having particle deposition (chemisorption, or physisorption) on the channel walls. This may lead to fouling of the reactor if not been checked for.²⁷

Screening is another important application of microreactors. The application of screening can be accomplished by holding reaction parameters systematically and

varying one of interest. This will make it easily handle large bank of experimental data to investigate unique reaction parameters on large scale.

Alkyl amines as an additive to CdSe QDs synthesis was investigated by using single heated capillary fed by syringe containing fixed amount of pre-mixed CdSe precursor solution and varying the alkyl amine amount, the size, shape was influenced by the electron donation of alky amine. The results showed control in growth rates, passivation and optical properties this showed a luminescence peaks wavelength of QDs as per fig.

2.2.2.2.1. ^{27,28}

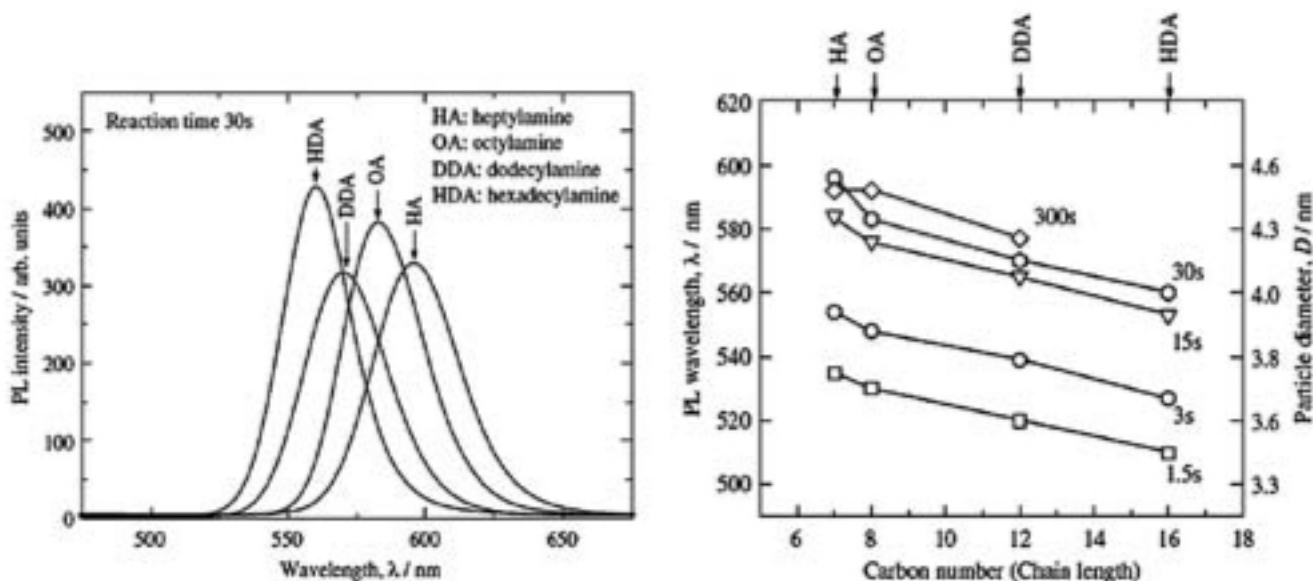


Fig. 2.2.2.2.1. Left image shows the photoluminescence spectra of CdSe product from capillary microreactor using different alkyl chain lengths. The right image shows the peak emission wavelength vs the chain length of alkyl amine at different reaction times. It concludes that longer alkyl chains showed smaller QDs with blue shifted emission due to diffusion of alkyl long chain compared to the smaller ones resulting growth rates reduction. ^{27,28}

2.3 Synthesising Copper face centered cube nanoparticles structure using MMRS

2.3.1 Experimental

All synthesis carried out using the Modular Micro reaction system (MMRS) from EHRFELD technology that was explained in Chapter 1 fig. 2.3.1.1.

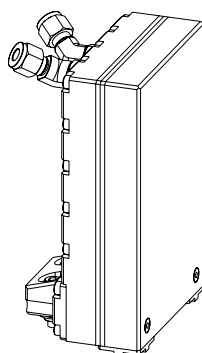
Copper nanoparticles production was tested before attending to make more complex reactions using MMRS. This is due the ease of reducing $\text{Cu}(\text{NO}_2)_2$ into Cu metal and also to test the system capability to isolate copper nanoparticles from further oxidation.

0.01 M $\text{Cu}(\text{NO}_2)_2$ used in ethanol to synthesis copper nanoparticles. The Huber oil circulator was adjusted at 160°C with a ramp rate of $5^\circ\text{C}/\text{min}$. The pressure valve was adjusted at 20 bars. The temperature and pressure observations were monitored through the lab-box temperature and pressure sensors that are hooked to the system via serial communication interface. This enabled adjustment to the pressure valve to meet the right torque set point manually 20 bars. The steel base plate was also adjusted at the same temperature in order to maintain homogenous temperature. The pump was set at 10 ml/min providing a resident time of 4 min. After pump completion of 100 ml ethanol $\text{Cu}(\text{NO}_2)_2$ mixture, the brownish/orangeish product was collected at the outlet in a flask after left to cool down at room temperature.

(a)



(b)



(c)

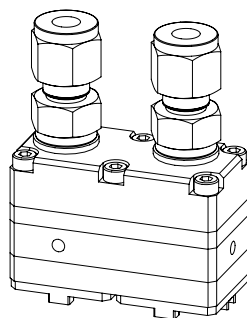


Fig. 2.3.1.1 Showing MMRS (a) steel microreactor (b), sandwich reactor and (c) micro mixing unit. (From the manufacturer EHRFELD technology website)

2.3.2 Materials characterization

Panalytical X'Pert Pro MPD series diffractometer was used to collect X-ray diffraction (XRD) scans, with Cu K α radiation ($\lambda=0.154056 \text{ \AA}$) in θ - 2θ geometry. Further analysis was carried out using X'Pert Highscore Plus software. Grain size of XRD scans

was determined by starting with background correction then smoothed and each FWHM for each peak was identified using the Profit algorithm.

Transmission Electron Microscopy (TEM) was performed with a Zeiss Libra 120 operating at 120 kV and a JEOL 2100 LaB6 operating at 200 kV. TEM samples were prepared by suspending the particles in ethanol and sonicated for five minutes. Small amounts were then pipetted onto ultrathin carbon TEM grids and the solvent was allowed to dry before imaging. Lakeshore VSM with a maximum applied field of 10 kiloOersted (kOe) used to identify magnetic properties. Isothermal Remanance Magnetization (IRM) plots were collected as a function of applied field. IRM plot, the magnetization was measured at zero field, then ramped to ΔH , and returned to zero field.

2.3.3 Results and discussions

As per the refined scans from XRD fig. 2.3.3.1, the fitted peaks matched copper face centered cubic metal of standard (JCPDS card no. 4-0836). The crystal size was 50 nm calculated from Scherrer calculator built in High score tool. The XRD scans reveals MMRS ability to produce chemically stable copper nanoparticles. This reaction was done under high-pressure 20 bars, which permitted ethanol to act as a reducing agent. Ethanol has been successful to reduce cobalt metal in an autoclave with high pressure and temperature reaching close to supercritical conditions forbidden the vaporized fluid from going back to liquid phase even at higher than the critical temperature.³⁴ Generally, supercritical conditions will allow fluids to reach critical temperature and pressure where vapor/liquid terminus coexistence curves.³⁵ The advantage of MMRS over autoclave is the ability to provide real time control on pressure and temperature. Operating the ethanol

at 20 bars and 180°C will increase the reduction rate crystallizing copper particles into FCC copper structure resulting in shorter resident time requirements for the microreactor.

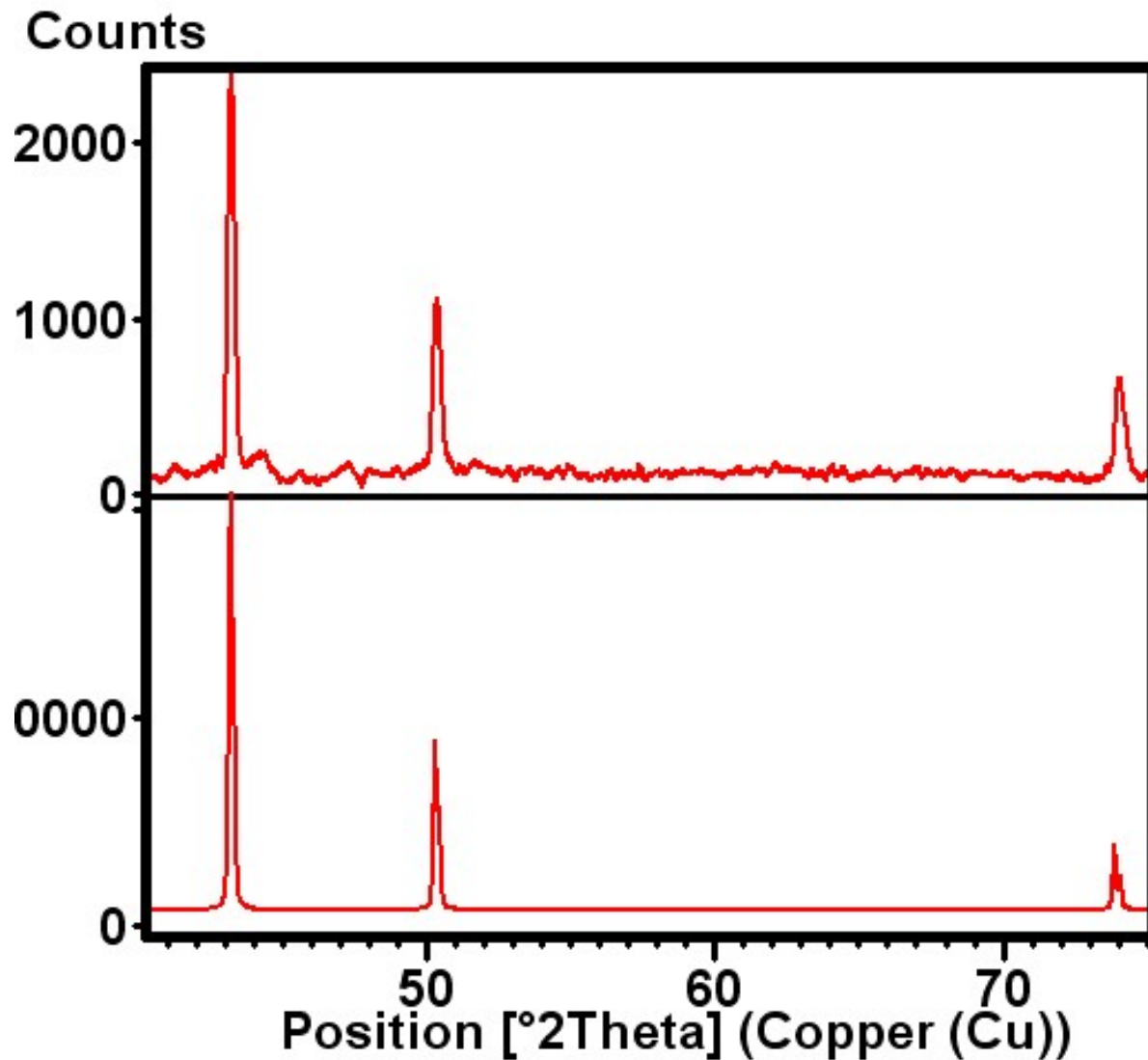


Fig. 2.3.3.1 Top XRD scans for 10 ml/min flow rate of $\text{Cu}(\text{NO}_2)_2$ in ethanol at 180°C and 20 bars matching FCC copper structure of JCPDS card no. 4-0836 below peaks. The crystal size of 50 nm was calculated using Scherrer calculator tool from High score.

The fast nucleation attributed to the homogenous high temperature also high pressure that induces multistage process nucleation resulting in excessive particle growth similar to burst nucleation.³⁶

The advantage of having lab-box control monitor is of high importance enabling immediate pressure and temperature automated correction during reaction with high accuracy. This will avoid uncertainty and regular manual errors created by human in traditional bench reactions.

Producing copper nanoparticles in MMRS is more empirical when compared to the microwave method to produce copper nanoparticles in polyol. Unlike microwave method to produce copper with polyol, the MMRS can shown copper production with no capping agent needed neither high power for temperature operation or ascorbic acid as a reducing agent used in microwave methods.³⁶ The high mixing at the molecular scale capabilities of MMRS makes the reduction process much faster providing a reduction in temperature.

2.4 Synthesising cobalt hexagonal nanoparticles structure in MMRS

2.4.1 Experimental

All synthesis carried out using the Modular Micro reaction system (MMRS) from EHRFELD technology that was explained in Chapter 1. Attempts to scale up Co metal with MMRS was done by using 4:1 sodium hydroxide NaOH to Cobalt tetra hydrate acetate $\text{Co}(\text{C}_2\text{H}_3\text{O}_2)_2(\text{H}_2\text{O})_4$ molar ration in tetra ethylene glycol (TEG). The solution was

heated up to 100°C in 250 ml round flask then pumped to the MMRS system in order to dissolve the hydroxide and cobalt precursor. Pumps were set at high flow rate 25 ml/min providing a total resident time of 2 minutes inside the sandwich reactor whereas the Huber oil circulator was set at 300°C with a heating ramp of 5°C/min. The steel base, where all parts mounted as per fig. 3.8, temperature was set at 200°C to keep the temperature while the product flowing in the whole system. The product flowing out from the outlet module in a separate flask was left to cool down to room temperature for 20-25 min. Then, the powder product was collect with a rare earth magnet and sonicated with Methanol three times before kept in vacuum oven overnight.



Fig. 2.4.1.1. Modular Microreaction system (MMRS) containing all parts; mixture, sandwich microreactor, inlet/outlet modules, and flanges.

2.4.2 Results and discussions

The collected powder showed hexagonal Cobalt peaks as per fig. 2.4.2.1 verified by. This is an indication of an intermediate phase before forming Co_xC as per previous studies. The different flow dynamics illuminated in fig. 2.4.2.2, whereas for MMS due to fast flow rate the flow will be looking like the one at (a).

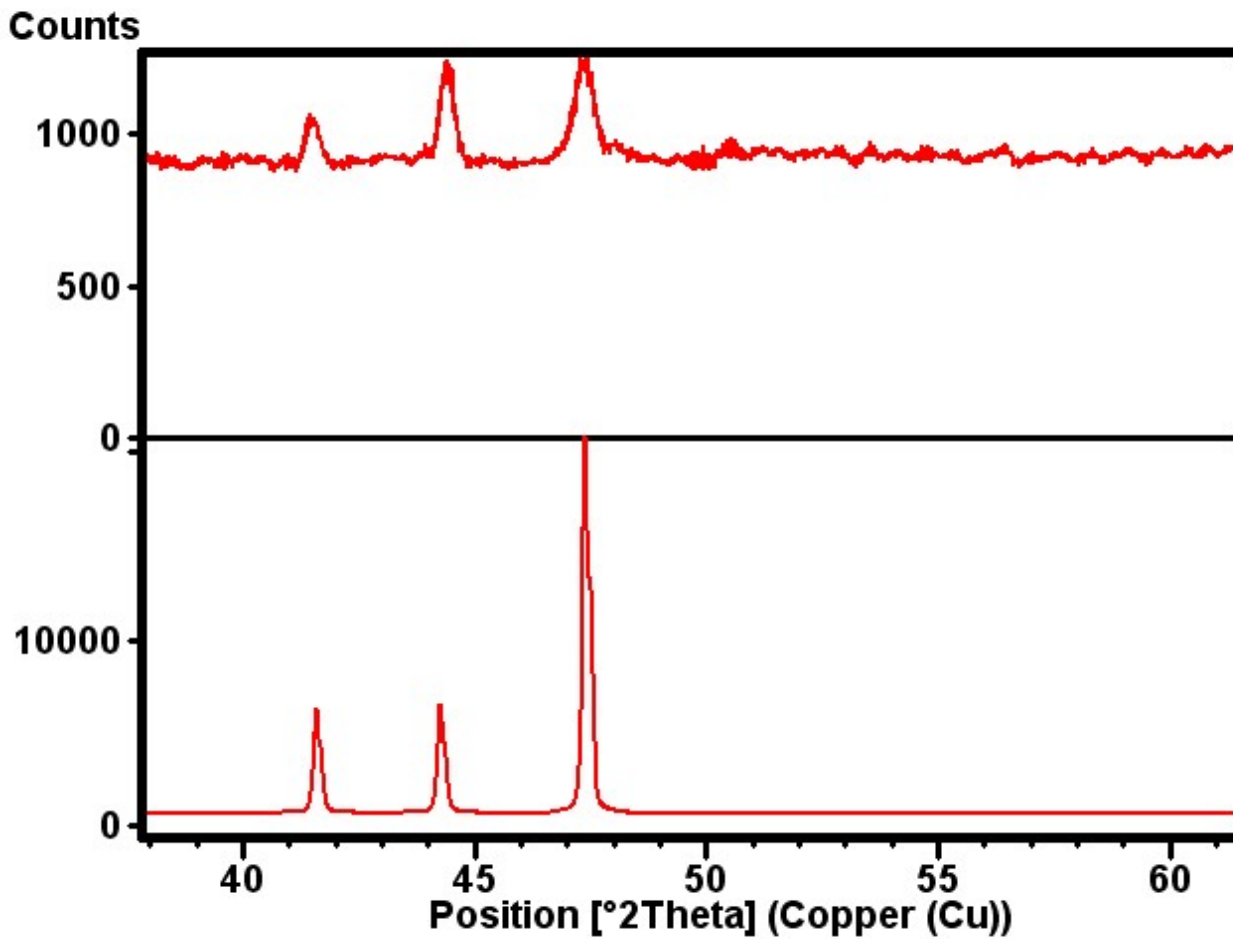


Fig. 2.4.2.1. XRD simulation pattern for samples collected at the outlet of MMRS upper peaks showing intermediate phase of Co hexagonal before forming Co_2C compared to HCP Co standard (Reference code number 01-08904308).

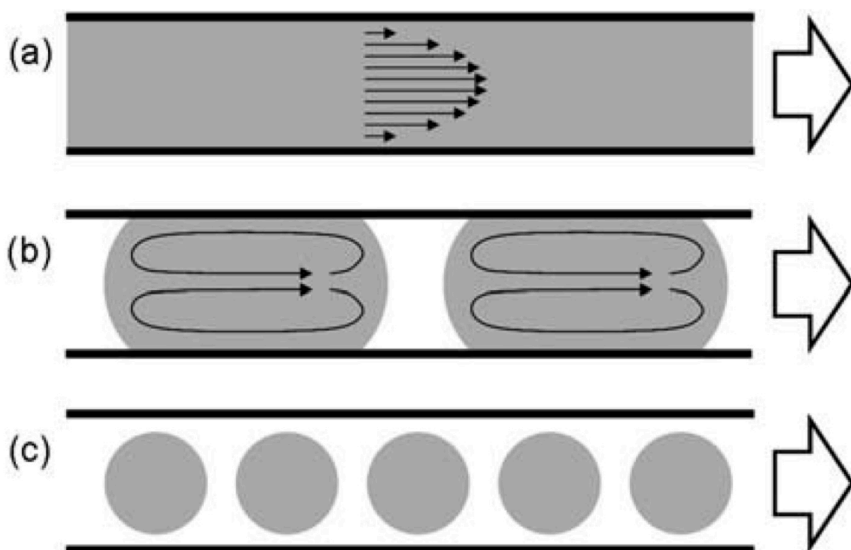


Fig. 2.4.2.2. Diagram showing three different flow regimes in micro fluidic reactors. In (a) In continuous flow parabolic velocity profile is formed across the channels when a friction with the tube wall, the velocity will be faster at the center of the flow with respect to the flow profile, (b) In slug flow the flow profile is discrete due to the immiscible phase introduced in the flow stream that can be gas or liquid that will cause convective mixing occurring across the channels, (c) flow stream in discrete droplets from immiscible liquid phase that are beneficially isolated from the channel walls.²⁷

The VSM revealed magnetic properties of cobalt HCP structure nanoparticle with 20 nm crystal size produced by MMRS. The saturation magnetization was 93 emu/g with a coercivity of 130 Oe shown at fig. 2.4.2.3 that are much higher than results reported by other literatures (80 emu/g and <than 50 Oe) cobalt HCP nano particles for nanoparticles produced with reducing agents.³⁰

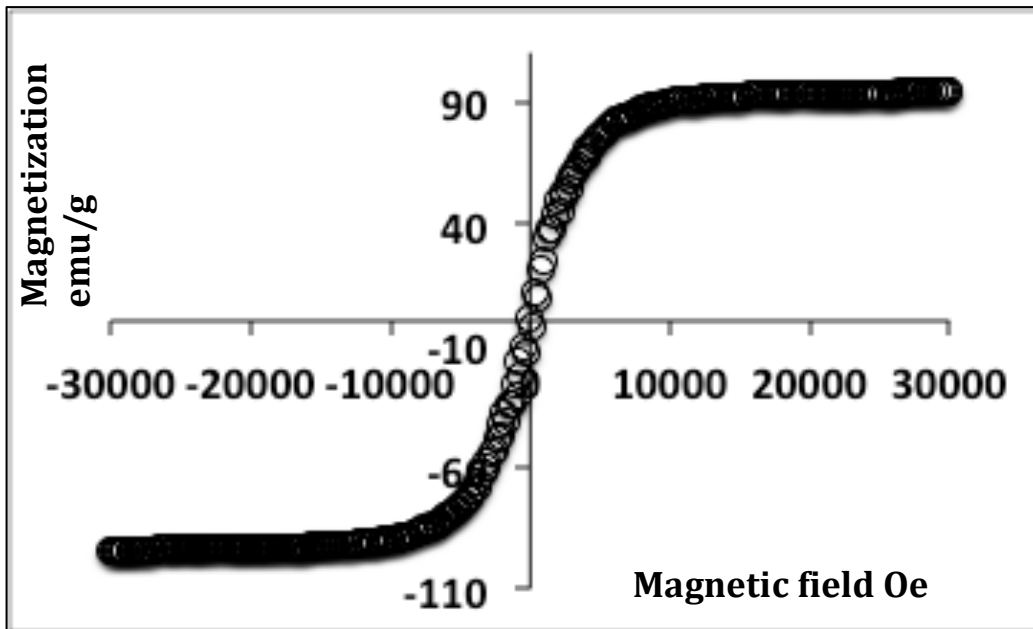


Fig. 2.4.2.3. Magnetic hysteresis of cobalt HCP showing magnetization of 93 emu/g and coercivity of 130 Oe.

2.5 Synthesising Cobalt carbide in modified MMRS

2.5.1 Introduction and motivation

Polyol (polyhydric alcohol) process used to reduce various metals when operated at boiling point temperatures of the glycol solvents. The mechanism governed by the ligand exchange between the deprotonated glycol and metal salt. At elevated temperature the excess glycol ions will reduce the salt metal also working as capping agent. In previous studies depending on the base amount, and reaction temperature, nucleation, and growth dynamics can be controlled.^{9,33,37,38} Regulating the growth and nucleation rates result in pure phase control of Co_2C and Co_3C . The addition of base will lower the

reaction temperature, which will lower the nucleation and growth rates.^{33,39} Reducing the growth rate is essential for surface reconstruction and diffusion of carbon atoms in cobalt crystals. The role of OH⁻ is extended to lower the distillation temperature and alter the capping agents to the cobalt carbide nucleus. The polyol mechanism to produce cobalt carbide suggests that aldehyde resulted from metal reduction function as carbon source similar to carbon monoxide in Fischer Tropsch (FT) reactions.⁴⁰⁻⁴² Polyol method holds the advantages of cost effective to produce transition metal carbides when compared to general method; mixing metal with carbon at 600°C whereas in polyol route temperature can be reduced to 300°C. A study was done to analyze cobalt carbide decomposition temperature with for both phases; Co₃C and Co₂C at high temperature.^{34,39} Co₃C decomposes at 325°C to α-Co while Co₂C will decompose at 275°C to α and β-Co.

2.5.2 Experimental

The hitch of low resident time requires a modification in the MMRS design without losing the advantage of molecular mixing capability of MMRS. The design should not disturb the flow rate and keep it at 25 ml/min. The new set up was implemented by adding another heating zone system with all the associated accessories shown at fig. 2.5.2.1. The fig. illustrates the second Huber oil bath that will have a 160 inch steel coil soaked inside at a temperature of 300°C. This unit is simply added to the typical one used in previous reactions. The outlet of this unit will be mixed in microchannel mixture and then flow inside the sandwich reactor to carry on the reaction and provide 6 minutes with the new setup.

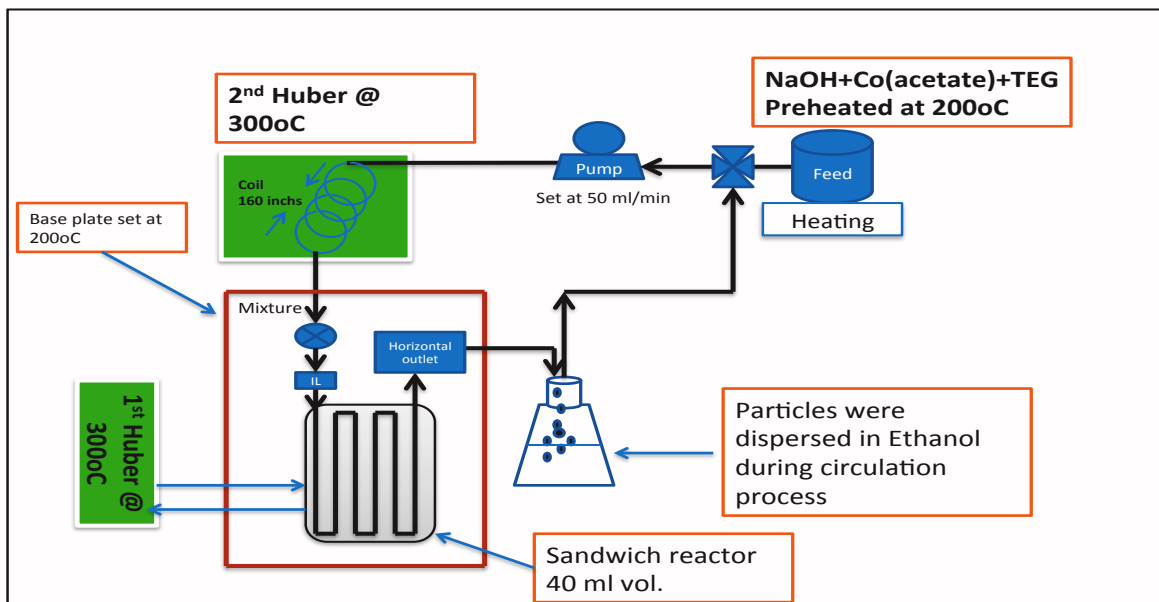


Fig. 2.5.2.1 Modifying MMRS to have a sequential heating zone under Huber 2 by adding 160 inches coil adding a volume of 128.6 ml that will increase the total resident time to 6.7 minutes.

2.5.3 Results and discussions

MMRS offers better features when compared to other microreactors: reliable simple scale up, defined residence times, enhanced operational safety, simple automation, higher yields, selectivity, high mixing speed, and excellent heat transfer. Micro mixing is important to shorten the mixing time as much as a mixing index of 95% in 1 s for dispersed gold nano particles.⁴³ MMRS give an advantage of customized as per the process requirements fig. 2.3.1.1(a). The parts can be assembled/de-assembled according to the experiment requirements. Parts we will be using in our set up will be; mixing unit Fig. 2.3.1.1(c), sandwich reactor Fig. 2.3.1.1(b), pumps as high as 50ml/min, and inlet/outlet feed Fig. 2.3.1.1(a). Both units in Fig. 2.3.1.1(b) and (c) will provide high

mixing due to the small channel lengths that are inversely proportional to the flow.^{44,45} With the modified set up improvement to resident time is achieved with respect to laminar flow.

The hydroxide introduction in this flow polyol reaction will play important role influencing the reaction kinetics. In other literatures the metal to hydroxide ratio increase showed also an increase in the grain size just like in the case of OH/Ni.^{33,34} Other ways to control the size particle was to use stronger reducing agents e.g. Trimethylene glycol (TMEG) compared to Triethylene glycol (TEG) and ethylene glycol (EG) to accelerate the reaction of Pt nanoparticles.⁴¹

The product was collected from the outlet in the same procedure done in the last sections and the XRD show that there was an improvement in Co_xC phase at Fig. 2.5.3.1.

Fixing OH/Co ratio based on knowledge from previous literatures showed successful production of Co_xC ($x= 2$ or 3) on bench chemistry.^{17,33,39}

Keeping the high flow rate maintained is vigorous for the following reasons:

1) Providing narrow resident time range for particles hence avoiding high dispersity. This can be attributed to the shear forces divulge from the channel walls. The effect of shear force will provide a parabolic flow profile where at low flow rate particles will have almost zero flow rate at the surface of the channels and will be highest at the center of the flow profile shown at fig. 2.4.2.2.^{27,46-48} 2) Avoid clogging inside the sandwich reactor channels that is related to the narrow resident time and providing control over nucleation/growth processes.⁴⁷

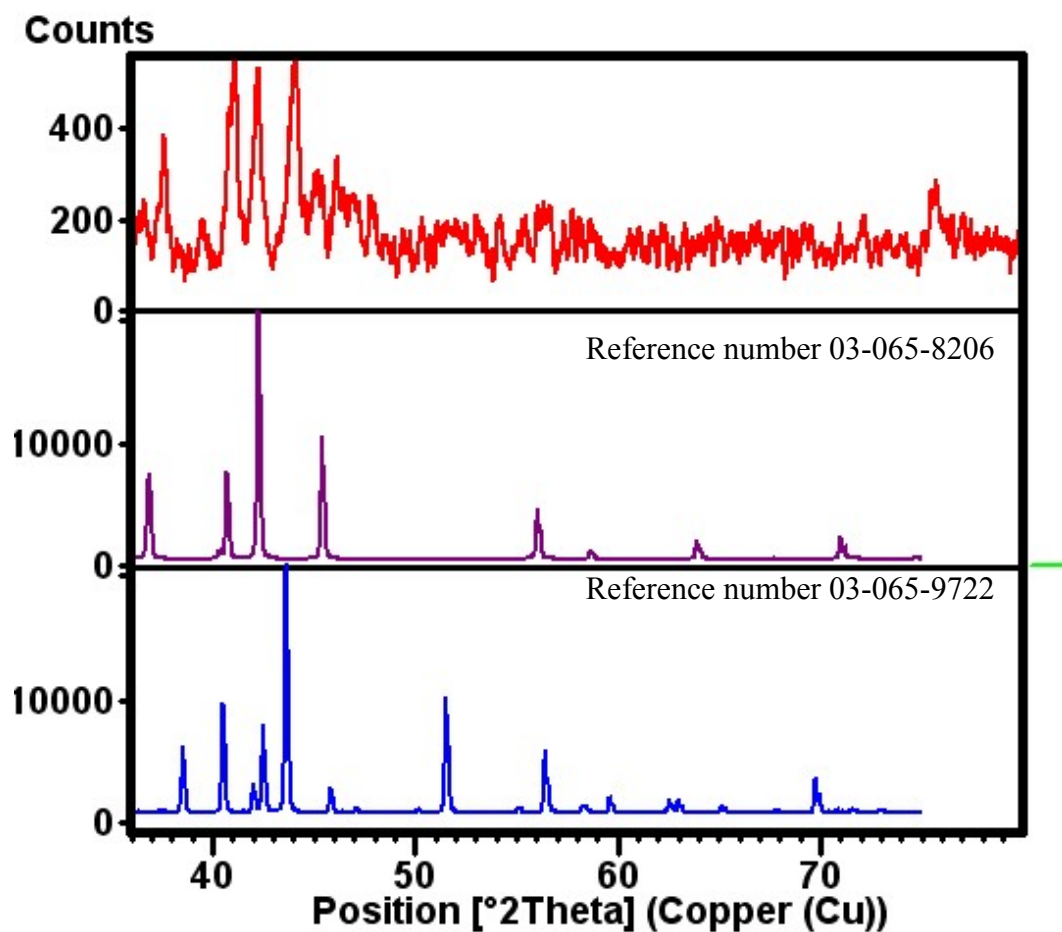


Fig. 2.5.3.1. High score simulation peaks showing mixed phase of Co₂C (reference number 03-065-8206) and Co HCP (reference number 03-065-9722).

The need for longer resident time is based on previous literatures whereas long reaction time is significant for the TEG to breakdown to operate as an active carbon source inside the cobalt metal lattice resulting in cobalt carbide product.^{18,37,44,45,49}

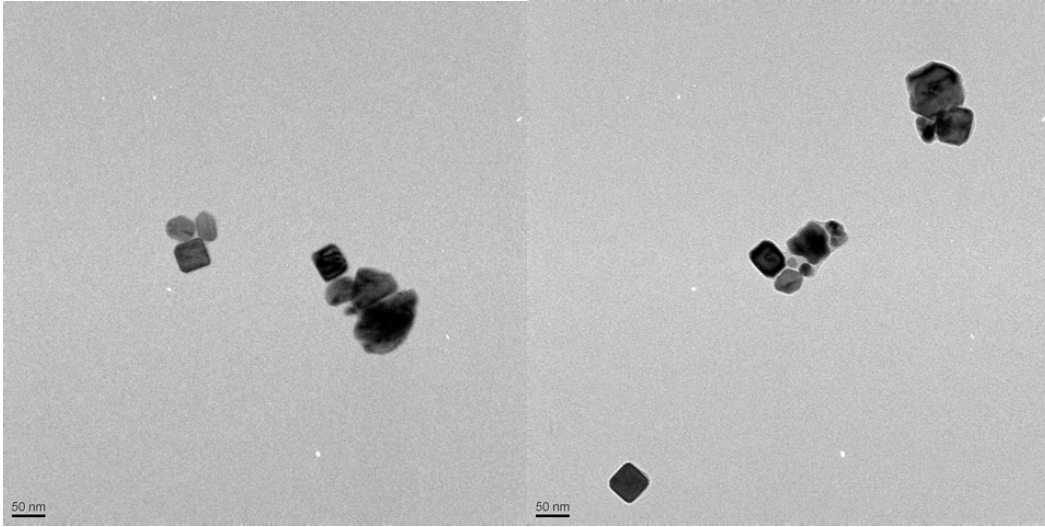


Fig. 2.5.3.2. TEM images showing cubic particles with the size of 20 – 50 nm.

Fig. 2.5.3.2 show interesting shapes of cubic particle (size of 20 – 50 nm). This is resulted from incomplete cobalt carbide nucleation. Pure phase of cobalt carbide have shown nanorods or sea urchin shapes in previous literatures.^{17,33}

2.5.4 Conclusion

MMRS have shown the flexibility in producing different metals such as copper FCC and cobalt HCP nanoparticles. Cobalt HCP magnetism properties was showing higher values when compared to microfluidic reactor requiring strong reducing agents such as hydrazine (N_2H_4) or lithium hydrotriethylborate ($LiBH(C_2H_5)_3$).³⁰ Scaling up cobalt carbide has been challenging requiring modification of MMRS in order to meet nucleation time for cobalt carbide and growth. The challenges also was the change in solvent viscosity at high temperature which also affected the flow nature from laminar to turbulent flow resulting in a change in Reynolds number as per the equation

$$Re = \mu D/\nu$$

Where; μ is the linear flow velocity, D is the inert diameter of the tube, and ν is kinematic viscosity of the fluid.

Previous studies have not addressed the plausible scale up of Co_xC by continuous flow microreactor, which is significant to meet industrial needs. The desire to scale up Co_xC materials with a continuous flow microreactor was mainly to investigate the viability for continuous flow chemistry, and possibly use pilot reactors at a later stage before production in large-scale industry. To the best of our knowledge Co_2C or Co_3C have not been produced in scale up processes. However, other studies have shown success in production of other nanomaterials such as Ag nanoparticles (NPs) in continuous flow microreactor.^{45,46} These microreactors used to produce Ag nano particles are not viable for producing Co_xC nanoparticles. This is attributed to the limitation in temperature capabilities of microreactors that is based on Polydimethylsiloxane (PDMS) materials.^{44,45,47,50} The nature of PDMS material will not make it practical for polyol reactions since they need higher temperature above $\sim 300^\circ\text{C}$.

The cobalt carbide reaction is exothermic in which fixed beds will not be suitable for the process e.g. patch reactors. This is attributed to the poor heat transfer rates of the fixed beds promoting hot spots rise during the operation. Flow chemistry process may overcome this problem, offering a condition of higher heat transfer rates coefficient.⁴⁰ In Fischer-Tropsch process, the higher the temperature at the inlet the higher rate of coke formation will be produced. Also, the lower ratio of H/CO the higher coke rate formation is observed. In this process graphite will be produced due to what's called the *Boudouard*

carbon reaction.⁴² Unlike the fixed bed reactor the flow reaction used in MMRS will reduce the possibility of reactor plug due to the graphite formation during the process.

Chapter 3. JMP statistical software for design of experiments

3.1 Introduction

JMP was developed by John Sall 1980 and was first released as statistical software tool at 1989 from SAS, which is a leading tool in statistical computerized field. This powerful tool used in many fields; business, agriculture, industry, and scientific research. Semiconductor manufacturers were one of the first to adopt JMP in their industry.⁵¹

In science, experimentation is a vital step in the scientific method. There are cases where scientific phenomena is will understood and have straight forward formula that can be easily used to extract good results. But in a complicated system such as wet reaction chemistry a straightforward formula cannot elucidate information.

JMP have showed the possibility to minimize the experimental runs and provide cost effective approach to analyze the findings. In tradition design of experiment one will require to test each factor (effect) individually by varying it and observing changes within the output (response) in cause and effect style. The disadvantage of this set up is time and cost consuming in addition it's not practical in scientific findings. JMP provides the dynamic interaction between statistical data and graphs allowing ease interpretation and helps in making decisions when trying to allocate and predict for example the most significant factors affecting the experiment results.

JMP is a statistical software tool that can be used to design experiments to allocate optimum conditions for the best response.^{52,53} In general JMP statistical tool utilizes design of experiment to offer the following advantages:

1. Reduce time to design/develop new products.
2. Provide process improvements for current process.

3. Achieving process robustness.
4. Improve reliability, and performance of chemical processes.
5. Evaluation of materials properties with respect to their process conditions

A good example to explain the useful tool in experiments, suppose that a metallurgical engineer is required to study the hardening processes; for example oil quenching and saltwater quenching, on an aluminum alloy. The engineer objective in such case to determine which quenching solution procedure produces the maximum hardness for the alloy. The engineer investigated the harness by subjecting a number of alloy specimens to each quenching solution that will be measured to determine which one is more solution hardness is the best. This looks like a simple experiment but there will be many questions that can be extracted from such simple experiment such as:

1. Are those the only two quenching solutions that are interesting?
2. What other factors that might be affecting the hardness besides quenching solution for example temperature, quenching media?
3. How many allow specimens should be tested in each solution?
4. What are should the data of the specimen alloys be tested and how will they be assigned?
5. Which data analysis method should be used?
6. Which determined difference in average hardness between two quenching solutions considered important?

These questions will be important to answer even before performing the experiment.⁵⁴

3.2 Design of experiments (DOE)

In this chapter only discussions to explain the basic knowledge required for the experimental parts on chapter 4 and 6. Design of experiment using JMP software is reliable to link the statistical data with the graphs. The design of experiment is essential to study the performance of process and systems shown in fig. 3.2.1. Experiments generally used to study the performance of a process to gain knowledge on possible enhancement or identifying the significant factors affecting the performance. The process interest will be the synthesis of cobalt carbide in poyol reaction through this dissertation.

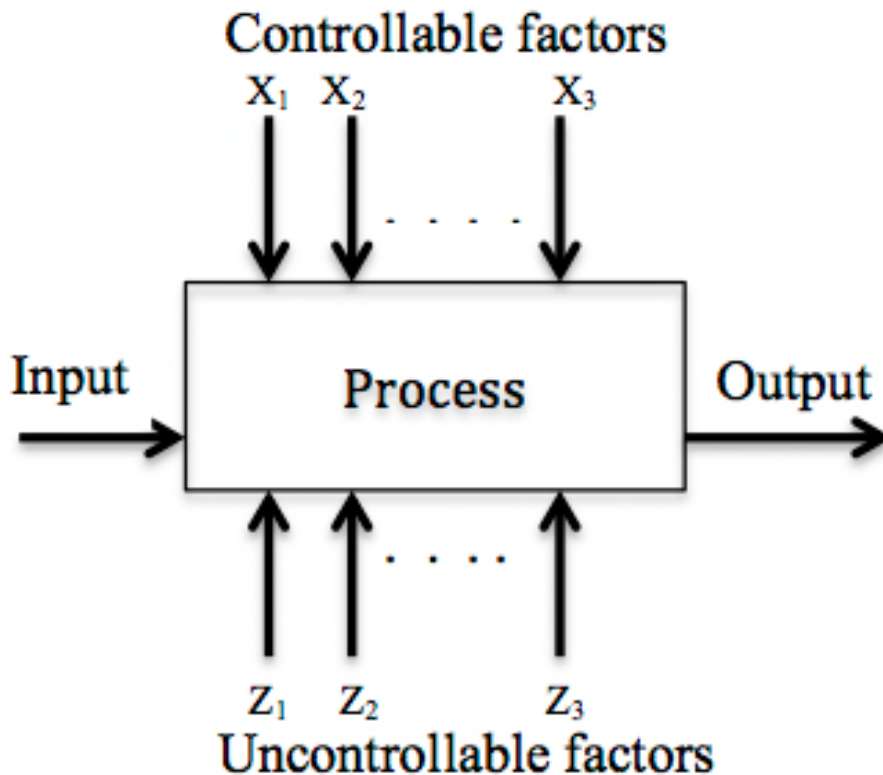


Fig. 3.2.1. Typical model for a process system.

Process such as chemical synthesis that transforms some input such as materials into an output called response and can be more than one. Some of the polyol process variables are controllable x_1, x_2, \dots, x_3 . These controllable variables in polyol synthesis to produce cobalt carbide can be; concentration, reaction time, reaction temperature, temperature ramp rate.... etc. Each factor normally have level of which it will operate during the experiment e.g. a temperature factor having two levels will have two different operating set point temperature. The uncontrollable variables z_1, z_2, \dots, z_3 cannot be controlled directly although they may be the interaction between any of the previous factors.

The goal of the experiment can be generally focus on the following outcome:

1. Determine the variable most affecting on the response y .
2. Determining set points for x 's to get the required nominal value for y .
3. Determining where to assign x 's so that y is small.
4. Determining where to set x 's so that the uncontrollable variables z_1, z_2, \dots, z_3 are minimized.

Normally choosing factors are based on engineering judgment and experience from previous reactions.⁵⁴

One of the famous strategies in experimentations is commonly practiced is the **one-factor-at-a-time (OFAT)**. In this technique one of the factors is selected from the starting point (baseline) and varied between its levels while other factors are held constant at their baseline level. After all tests are done, series of graphs showing the response changing by each change of the individual factor while others are held. Generally the interpretation of those graphs is straightforward. This is due to the simplicity of having all other factors constant while one only is varying with respect to

the response. The main disadvantage of the OFAT strategy is inability to show the interaction between factors. These interactions normally occur when an individual factor fails to display the same effect on the response for another factor at different levels.

3.2.1 Design of experiments types:

It is necessary to carefully select the design of experiment also based on number of factors. The design of experiment types are selected based on the objective experimenter trying to achieve.

1. Comparative objective:

The primary goal of this design is to identify the most important factor in an experiment in the presence or absence of other factors. This design will answer the question of whether this factor is significant; whether it changes the response significantly with a change in the levels. When there is a comparative problem between the factors, a comparative design is needed.

2. Screening objective:

In this design the experimenter is looking to distinguish between the important effects from many less important ones. This type of design is needed when there is a lack of experience and knowledge in certain process (experiment).

3. Response surface objective:

The importance of this design is to allow estimating the interaction and quadratic effects for complicated processes. The reason behind calling this method surface response is attributed to the ability to display information about the shape of the response surface that's investigated. This design is important for the following reasons:

- 1) Finding improved or optimizing process settings.
- 2) Investigating process problems and weak points.
- 3) Giving the process immunity against uncontrollable influences making the process more robust.

| <u>Number of factors</u> | <u>Comparative objective</u> | <u>Screening Objective</u> | <u>Response surface Objective</u> |
|--------------------------|---------------------------------------|----------------------------|--|
| 1 | 1-factor completely randomized design | - | - |
| 2-4 | Randomized block design | Full fractional factorial | Central composite or Box-Behnken |
| 5 or more | Randomized block design | Fractional factorial | Screen first to reduce number of factors |

Table 3.2.1.1. Design selection guide for choosing an experimental design.^{54,55}

Table 3.2.1.1 explains the basis of design of experiment selection type. It is better to select always the design with fewer runs than the budget

In general the importance of experimental design tool comes from the ability to improve the realization of a process in scientific and engineering world. The early development of experiment design in a process will result in the following:

1. Process yields improvements.
2. Reduce uncertainty and confirm target requirements.
3. Time reduction to reach ideal process requirements.
4. Reduction in process cost.

Surface response design contain two types of design:

A) Central Composite Designs

It compose imbedded fractional factorial design with center points that is enhanced with a group of star points that assist estimation of curvature as per fig. 3.2.1.1.

The distance from the center of the design space to a star point is $|\alpha| > 1$ when the distance from the center of the design space to the factorial point is ± 1 unit for each factor. The accurate value of α depends on the number of factors. A central composite design contains double, as many stars as there are factors shown in fig. 3.2.1.1. ⁵⁵

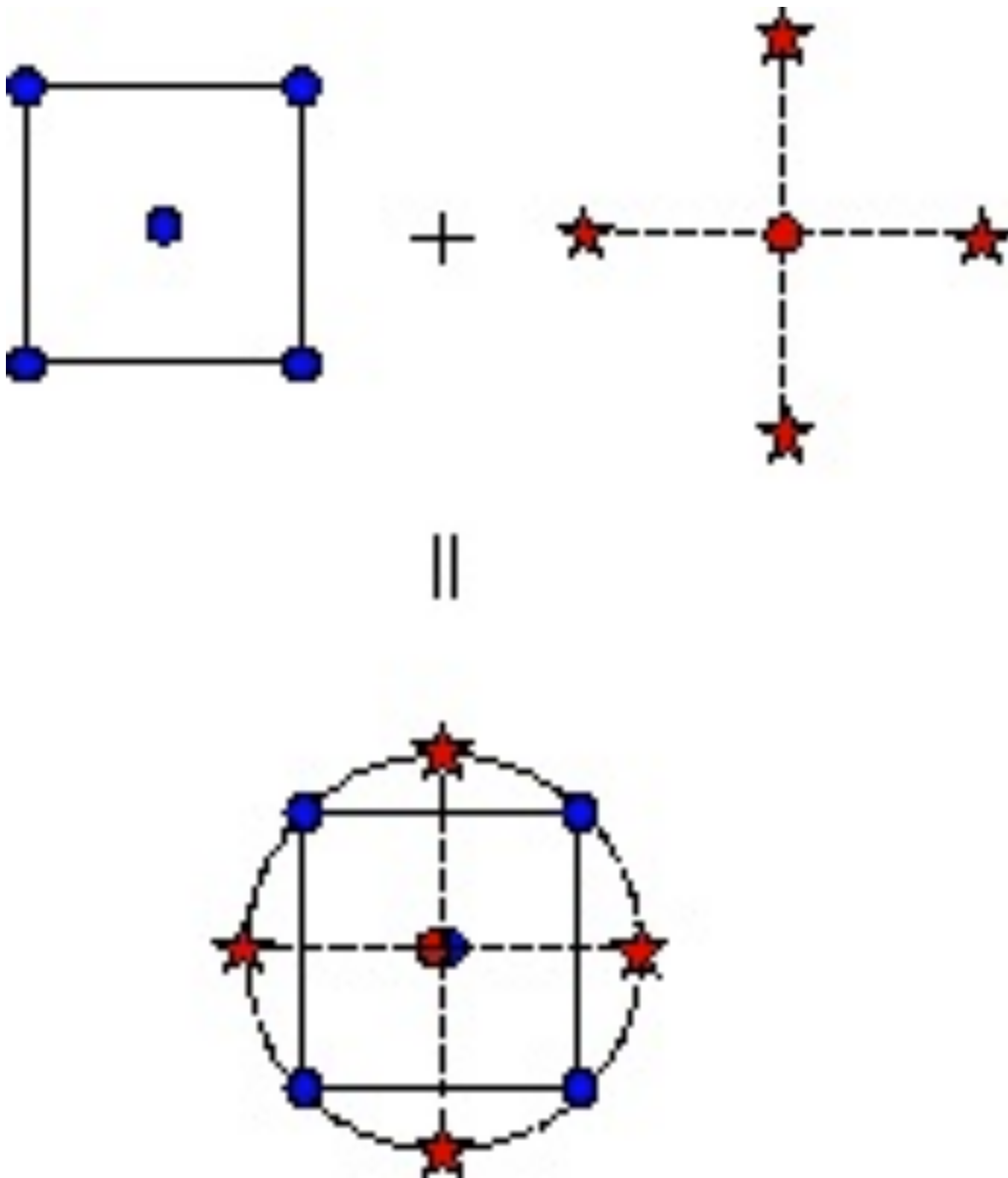


Fig. 3.2.1.1. Two factors generating central composite design.⁵⁵

Rotatability is required to be maintained for the design points through the value of α , which depends on the number of experimental runs as per the below formula:

$$\alpha = [\text{number of factorial runs}]^{1/4}$$

Number of factorial runs = 2^k , where k is the number of factors (effects).

B) Box-Behnken designs

This design unlike the central composite design does not contain an embedded factorial design, which makes it independent quadratic design. In this design the run points are at the midpoints of the process space and the edges as per fig. 3.2.1.2. The rotatability of this design comes from the requirement of three levels of each factor. The design is limited for orthogonal blocking compared to central composite design.

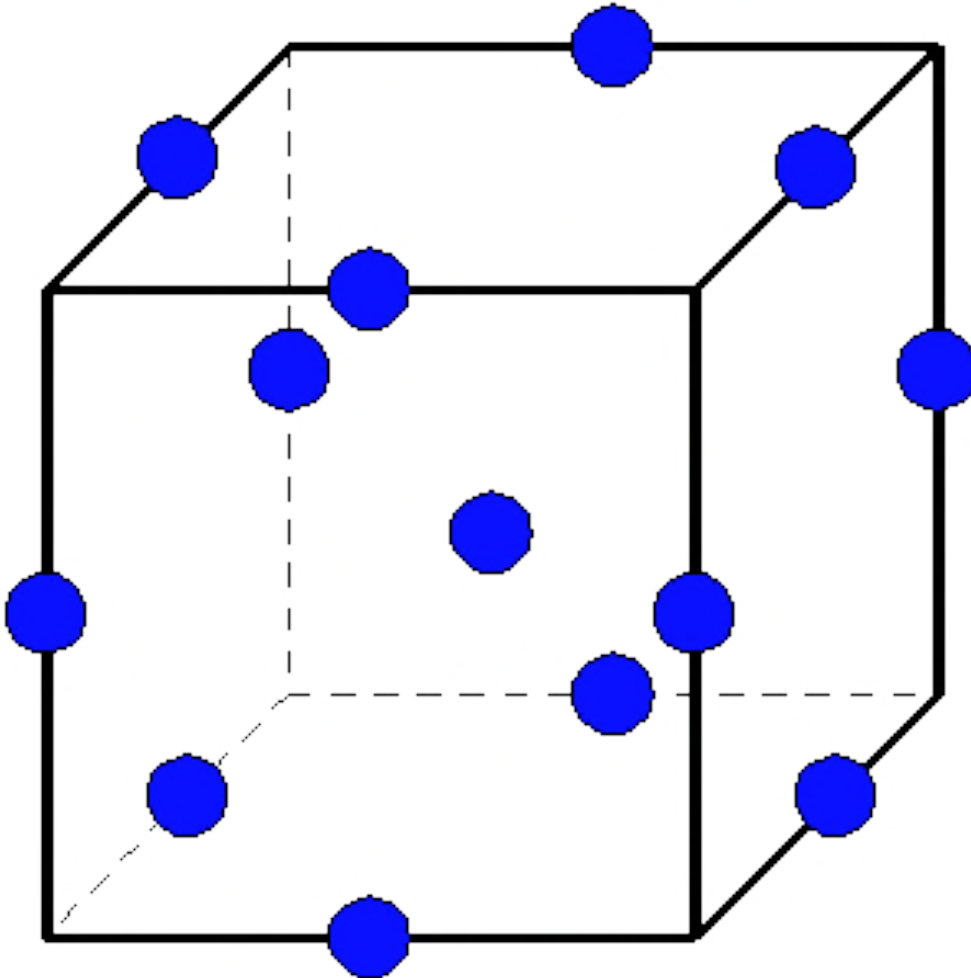


Fig. 3.2.1.2. Box-Behnken design for three factors.⁵⁵

JMP is a statistical software tool that can be used to design experiments to allocate optimum conditions for the best response.^{52,53} In general JMP statistical tool utilizes design of experiment to offer the following advantages:

1. Reduce time to design/develop new products.
2. Provide process improvements for current process.
3. Achieving process robustness.
4. Improve reliability, and performance of chemical processes.
5. Evaluation of materials properties with respect to their process conditions.

Conducting a design of experiment to produce Co_xC on bench chemistry, will allow us identify experimental parameters mostly affecting the magnetic properties. The outcome from studying the chemistry bench reactions statistically will provide understanding of parameters inducing the magnetic properties of Co_xC . This will be time and cost effective, avoiding the consumption of raw materials during scale up flow reactions. For example, if it is possible to optimize cobalt precursor by reducing the concentration and still have high magnetic properties for Co_xC , this same knowledge can be applied for scale up process to possibly reduce cost. The JMP tool is a powerful tool that been proved in industrial studies.

A project was done at SABIC technology center Huston (STCH) for studying the calcination of MgO base catalyst and the optimization of the regeneration process. The catalyst is used in alkylation process of phenol and methanol to produce 2,6-Xylenol. This was designed to give high selectivity (>60%) and conversion (>80%). Regeneration is a process in which calcination is performed at 475°C under H_2O steam, O_2 and N_2 to remove formed coke. The design of experiment (DOE) determined factors affecting the

decrease in surface area, which in turn reduces the efficiency of the catalyst lifetime after regeneration cycles. The DOE is designed based on definitive design, which used temperature, ramp temperature, soak time, and Nitrogen/Oxygen/Steam % mole concentrations, out of a space velocity of 2 as factors assumed to directly affect surface area shown at Fig. 3.2.1.3. This tool will also provide information about expected patterns when changing process parameters with minimum number of experiments by studying the surface response profile Fig. 3.2.1.4.

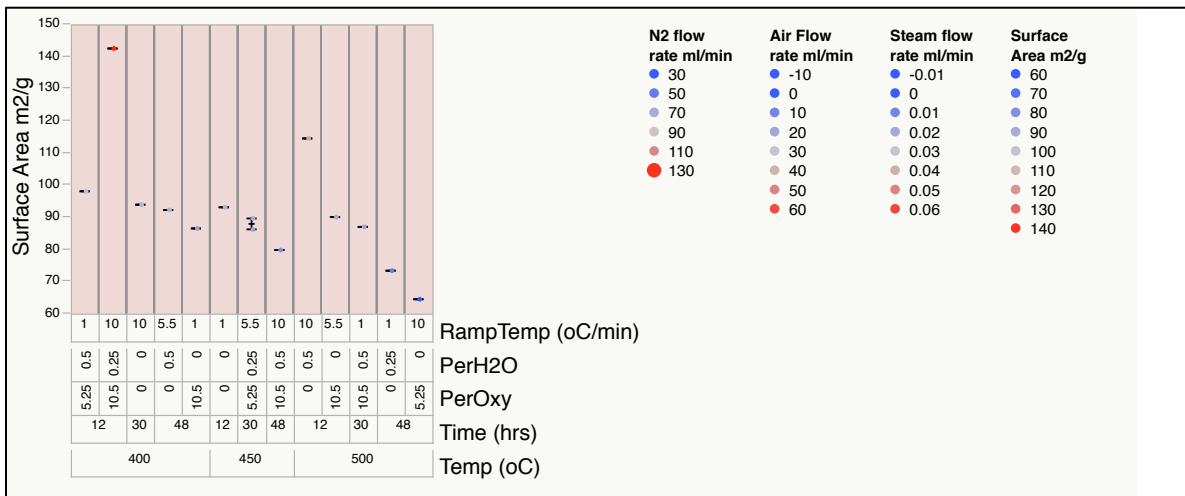


Fig. 3.2.1.3. Variability chart for MgO surface area (m²/g), affected by N₂ flow rate (ml/min), airflow rate (ml/min), steam flow rate (ml/min), which were chosen as factors.

This tool can be utilized to examine the conditions for experiments to reveal high magnetic properties by choosing coercivity, magnetization or other factor quantities such as particle size, crystal size, and aspect ratio for nano wires that will contribute to the magnetic properties. There have been many studies that discussed the enhancement of

magnetic properties for ferromagnetic materials such as Cobalt and Co_xC by controlling shape and size in polyol synthesis.^{9,17,33,37,49} The physical properties that encompass contributions to both coercivity and magnetization are magnetocrystalline, shape anisotropy, and magnetostatics.^{4,13,18,20,56} Basically particle size control can enhance coercivity when reaching the critical size of a magnetic particle, which was investigated in previous literatures. Critical size where the size of the particle will act as a giant spin and the magnetostatic energy will govern and be more effective than thermal energy.^{57,15}

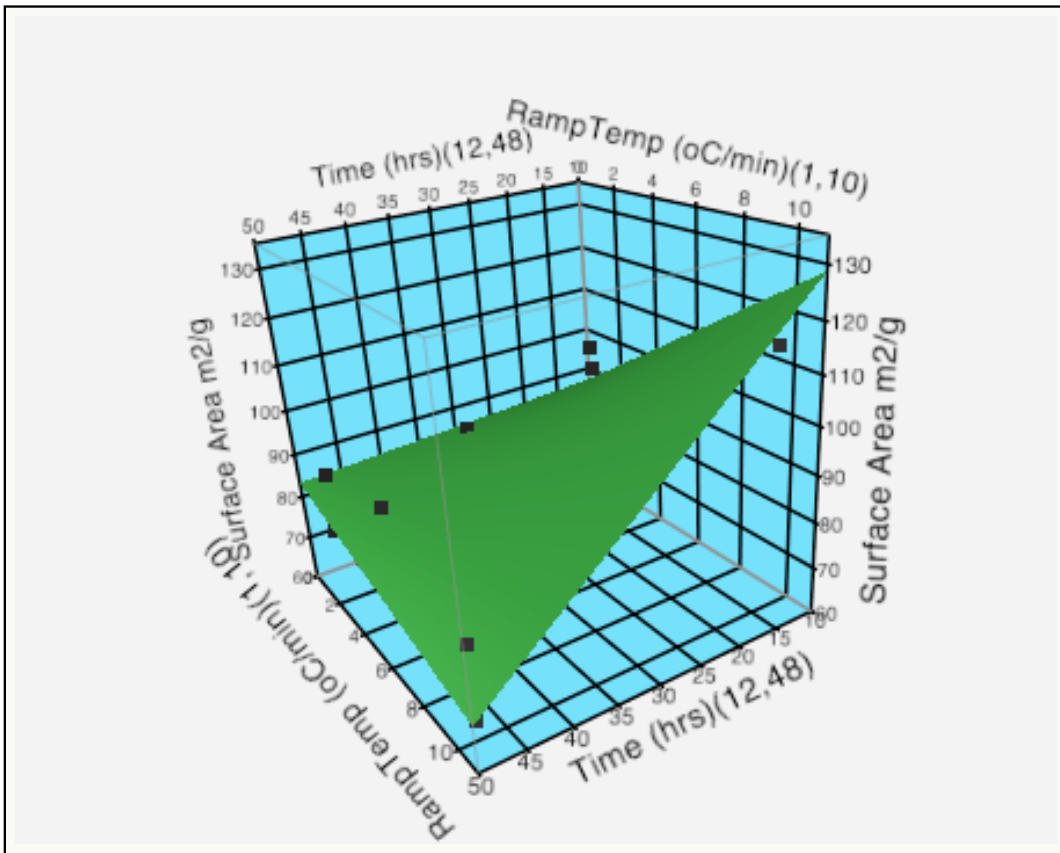


Fig. 3.2.1.4. Surface response profile showing forecaster of surface area in (m^2/g) response with respect to variation in in time, and ramp temperature.

**Chapter 4. Design of experiment to produce enhanced Co_xC
magnetic product in polyol with SAS-JMP statistics**

4.1 Overview/ Motivation

Cobalt carbide (Co_xC ($x=2$ or 3)) intriguingly has shown high magnetic properties but still varies based on different chemical approaches in previous studies.^{17,18,33,49} Co_xC ($x=2$ or 3) has been produced by different methods using polyol reaction routes.^{33,49} There has been many attempts to increase magnetization and coercivity of the Co_xC particles either by controlling the shape and size through varying the hydroxide concentrations or trying different precursors and solvents, but still justifying experimental conditions was not quantified to explain routes of optimizing cobalt carbide magnetic properties.^{33,49} This approach requires a statistical study to reveal the most important factors controlling intrinsic magnetic properties for Co_xC . From previous discovered magnetic materials not much statistical studies were done to show the relationship between anisotropy, energy product and Curie temperature that are influenced by the experimental conditions. The outcome of this statistical study will provide best practice to use when designing experiments in flow chemistry for the MMRS operation.

The objective of this chapter is to investigate and screen the conditions affecting magnetic energy product of cobalt carbide by introduce SAS-JMP optimization tool. The design of experiment will select some factors based on previous knowledge or other factors that have got our attention through cobalt carbide polyol synthesis. It is important to study the experimental conditions statistically since it never been studied in related cobalt carbide literatures.^{17,33,39} Statistical study will give better understanding for cobalt carbide chemistry and possibly estimate best conditions that will assist reaction when using flow chemistry approach.

4.2 Statistical approach to enhance ideal energy product of cobalt carbide and verify the significant parameters

Attempts to investigate the factors affecting the increase in ideal magnetic product energy resulted from magnetization and coercivity product $M_s \chi H_c$. The investigation was conducted statistical study choosing the following factors: temperature, time, and cobalt precursor concentration cobalt fumarate ($\text{CoC}_4\text{H}_2\text{CoO}_4$). It was reported that the selected factors are more vital in producing cobalt carbide.^{17,33,39} The system, which involves three significant independent variables Temp (X_1), Time (X_2), and Cobalt fumarate concentration (X_3), will be based on mathematical polynomial model to predict the response for a quadratic surface design:

$$Y = \beta_0 + \beta_1 X_1 + \beta_2 X_2 + \beta_3 X_3 + \beta_{12} X_1 X_2 + \beta_{13} X_1 X_3 + \beta_{23} X_2 X_3 + \beta_{11} X_1^2 + \beta_{22} X_2^2 + \beta_{33} X_3^2 + \varepsilon \quad (\text{eq.1})$$

Where ε is a random error component that follows a normal distribution with mean zero and unknown variance σ^2 ; where Y = estimate response in our case will be the magnetic product, β_0 = constant, β_1 , β_2 and β_3 = linear coefficients, β_{12} , β_{13} and β_{23} = interaction coefficients between the three chosen factors, β_{11} , β_{22} and β_{33} = quadratic coefficients. To obtain the coefficients of multiple regressions eq1 is used by JMP software.⁵⁸

The Box-Behnken design (Table 4.2.3.1) is used to construct a second-order polynomial model (eq.1) that can then be used to approximate the response function, which cannot be described by linear functions.⁵² The idea to generate reduction in the current operating conditions in the experiment protocols by utilizing a steepest ascent

method in order to meet the maximum possible increase in ideal magnetic product ($M_s \times H_c$). Reduction in experiment conditions such as temperature gives cost effective advantage for future industrial application.

4.2.1 Synthesis of cobalt carbide using based on JMP design of experiment

Cobalt fumarate was produced in the lab by adding 4.3 g of $\text{CoCl}_2 \cdot 6 \text{H}_2\text{O}$ in 10 ml of deionized water (DI) to 5.6 g of $\text{Na}_2\text{C}_4\text{H}_2\text{O}_4$ in a 20 ml (DI) heated under magnetic stirring for 20 min then put to dry in vacuum overnight. Using the dry pink powder of $\text{CoC}_4\text{H}_2\text{O}_4$ as starting material with TEG as one-step reaction method to get cobalt carbide Co_xC ($x=2$ or 3). The reaction started with $\text{CoC}_4\text{H}_2\text{O}_4$ in a 250 ml three neck round flask. 25 ml of TEG (Tetra Ethylene Glycol) $\text{C}_4\text{H}_{10}\text{O}_3$ was used to work as a reducing and capping agent. Each experiment was heated under reflux to different temperature, concentration, and time varying each of the parameter as per table 4.2.3.1 After the product was produced the solution was washed and the product was separated and collected by a rare earth magnet bar.

4.2.2 Materials characterization

Panalytical X'Pert Pro MPD series diffractometer was used to collect X-ray diffraction (XRD) scans, with $\text{Cu K}\alpha$ radiation ($\lambda=0.154056 \text{ \AA}$) in θ - 2θ geometry. Further analysis was carried out using X'Pert Highscore Plus software. Grain size of XRD scans was determined by starting with background correction then smoothed and each FWHM for each peak was identified using the Profit algorithm.

Transmission Electron Microscopy (TEM) was performed with a Zeiss Libra 120 operating at 120 kV and a JEOL 2100 LaB6 operating at 200 kV. TEM samples were prepared by suspending the particles in ethanol and sonicated for five minutes. Small amounts were then pipetted onto ultrathin carbon TEM grids and the solvent was allowed to dry before imaging. Lakeshore VSM with a maximum applied field of 10 kilo Oersted (kOe) used to identify magnetic properties. Isothermal Remanance Magnetization (IRM) plots were collected as a function of applied field. IRM plot, the magnetization was measured at zero field, then ramped to ΔH , and returned to zero field.

4.2.3 Result and discussion

The results of the designed shown at table 4.2.3.1, the study is interested in the qualitative results of the magnetic energy product. Other literatures have exhibited that it's impossible for cobalt to reach coercivities as high as 3 kOe at room temperature using this route with no modification.^{15,17,22,33,37,39} Although aligning cobalt nanowires have shown increase in coercivity at room temperature (3 kOe) but adding additional procedure is impractical for industrial scale up.¹³

This investigation advocated three factors and one levelled response analysed by response surface methodology. In the process of making mixed phases of Co, and Co_xC ($x=2$ or 3) multi phase carbides; time, temperature, and concentration were chosen as factors and magnetic product energy was chosen as one level response. The selections of these factors are based on previous study conclusions.^{18,33,39} Each of the three level factors designed with equal intervals in between each level. Temperature levels were selected as shown in table 4.2.3.1; 250°C, 275°C, 300 °C with 25°C difference between

each level.

| | Factor 1 | Factor 2 | Factor 3 | Response |
|----------------------|-----------------|-----------------|--------------------|--|
| Sample Number | [Co] (M) | Temp(°C) | Time(hours) | M_s x H_c(MGOe) |
| Sample 1 | 0.0005 | 250 | 2.25 | 0 |
| Sample 2 | 0.001 | 275 | 2.25 | 2.08 |
| Sample 3 | 0.0015 | 275 | 1.5 | 1 |
| Sample 4 | 0.001 | 250 | 1.5 | 0 |
| Sample 5 | 0.001 | 275 | 2.25 | 1.648 |
| Sample 6 | 0.0005 | 275 | 1.5 | 2.9925 |
| Sample 7 | 0.0005 | 300 | 2.25 | 2.625 |
| Sample 8 | 0.001 | 300 | 1.5 | 6.15 |
| Sample 9 | 0.001 | 250 | 3 | 0.295 |
| Sample 10 | 0.001 | 275 | 2.25 | 1.52 |
| Sample 12 | 0.0015 | 250 | 2.25 | 0.00351 |
| Sample 13 | 0.001 | 300 | 3 | 6.027 |
| Sample 14 | 0.0005 | 275 | 3 | 0 |
| Sample 15 | 0.0015 | 275 | 3 | 4.07 |
| Sample 16 | 0.0015 | 300 | 2.25 | 1.0875 |
| Sample 17 | 0.001 | 275 | 2.25 | 1.4186 |

Table 4.2.3.1. Design of experiment (DOE) for three factors with three levels and one response. M_sxH_c.

In previous literatures, conclusions elucidated temperature role that alter the transformation in glycol to ethoxy acetaldehyde that is associated with reduction in cobalt from Co²⁺ to Co⁰ at various temperatures.^{15,33,39,59,60} The kinetics play important rule whereas temperature regulates the growth in nucleation process. Temperature being a critical factor; will affect the nucleation rate also making TEG work as reducing agent as well as capping agent when reaching boiling point.^{20,33,34,39,56} In other literature temperature control displayed increase in magnetocrystalline resulted in coercivity increase and magnetic product enhancement.^{13,16,20,59} Particles experience poor crystallinity when crystal growth is suppressed by decreasing the reaction time therefore incomplete Co₃C phase produced.^{33,34} Time, temperature and concentration play

important role in Ostwald ripening mechanism. Basically, in Ostwald ripening process the bigger particles will be fed by the deconstruction of smaller particles that will dissolve instead.^{22,61} Time is vital factor; it is expected to govern the critical time in the growth process of cobalt carbide nucleus demonstrated in fig. 4.2.3.1.^{62,63} The time factor was designed with three levels at; 1.5 hrs, 2.25 hrs, and 3 hrs close to reaction time in previous results by same reaction techniques^{17,33,39} Varying Co concentration changes the supersaturation time needed for particles to reach their critical size and start growing. The concentration factor was designed at three levels; 0.0005M, 0.0015M, and 0.001M. Optimizing the precursor concentration is cost effective for industrial scale up application in future. The response (Y_1), which is of interest to optimize, will be the quantitative ideal energy product resulted from the product of coercivity (H_c) and magnetization (M_s) table 4.2.3.1, represented by the area under the magnetic hysteresis curve illustrated in VSM hysteresis in fig. 1.2.2.1.1.

A second-order response surface model fit introduced in curvature system represented in polynomial of higher degree shown below:⁵⁴

$$y = \beta_0 + \sum_{i=1}^k \beta_i x_i + \sum_{i=1}^k \beta_{ii} x_i^2 + \sum_{i < j} \sum \beta_{ij} x_i x_j + \epsilon$$

The model fit will assist identifying and predicting parameters with most significant effect on the ideal magnetic energy product calculated in MGOe. The model fit aims to provide the knowledge to take current operating conditions towards the region of optimum operating conditions shown in fig. 4.2.3.2.

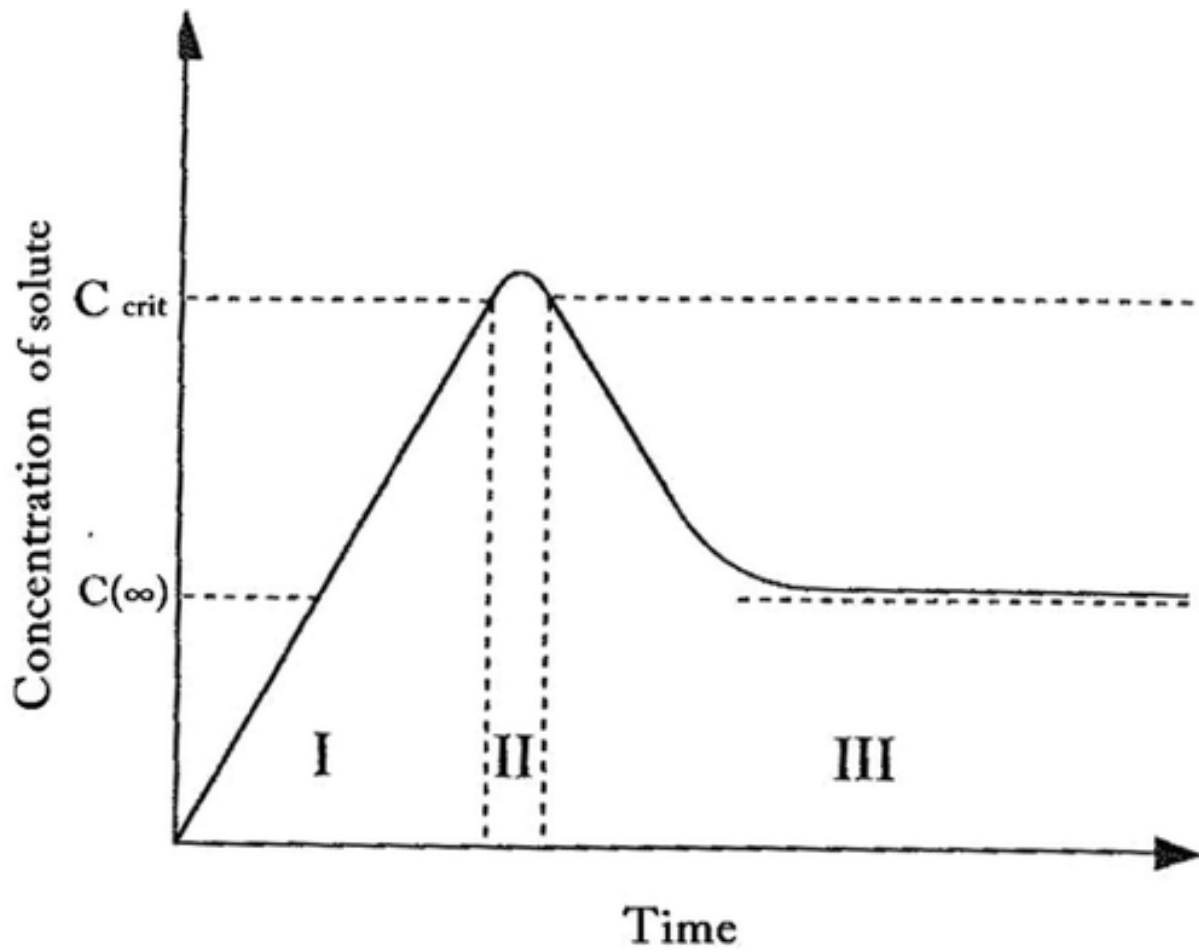


Fig. 4.2.3.0.1. La-Mer model demonstrate the mechanism of the growth and nucleation process vs time. At critical concentration (C_{crit}) the of nucleation process (stage II) start till the growth process kick in (stage III).⁶³

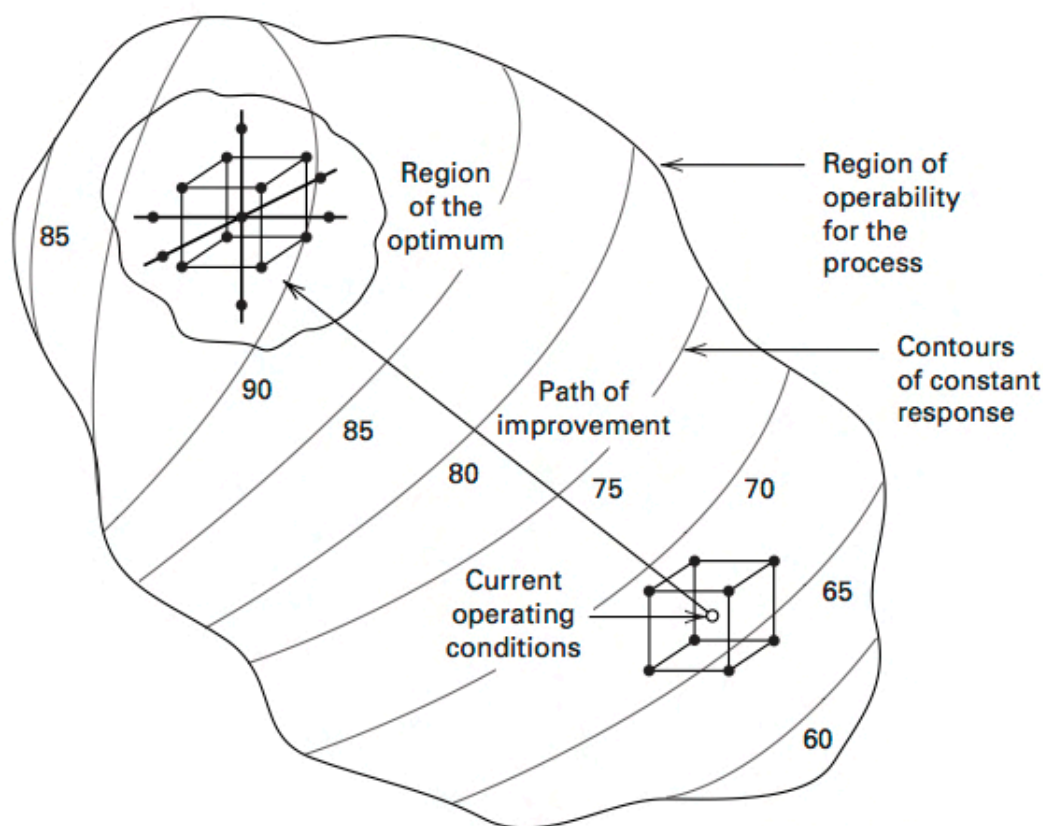


Fig. 4.2.3.2. The sequential nature of response surface methodology.⁵⁴

Analysing table 4.2.3.1, sample 13 have shown the highest ideal energy product (6.027 MGOe) at relatively aggressive conditions of 300° C and long reaction time (3 hours). This high condition is not practical when applied in flow chemistry technology due to the need for long resident time. These current operating conditions showing high ideal magnetic product are of our interest in order to optimize the model. It was concluded from table 4.2.3.1 that when comparing sample 13 with sample 9, high temperature and longer time is important to produce hard magnetic cobalt carbide. The coefficient of determination (R_{square}) of the targeted ideal magnetic product function (Y) gave 0.97, which means we can be 97% confident with the results of ideal magnetic product

variations from response (Y).

JMP provide prediction profile shown at Fig. 4.2.3.3. This prediction profile offers predictions of possible conditions to optimize and reach optimum response values. All factors can be geared towards the point where maximum values of response are possible. The first curve on the far left shows the concentration of the first factor [Co] that can be reduced to low values 0.0005M, second curve represents the second factor temperature fixed at 300°C and third curve represents time of the reaction in hours fixed at 1.5. The model showed that at these optimized conditions the response reaches the highest values at 6.64 MGOe.

One of the great advantages of using the surface response methodology opposed to one factor at a time for this study is the ability to detect dependency of the influence of one factor on the level of another factor.^{54,64} In table 4.2.3.2 the interaction effect is shown between different factors for different orders.

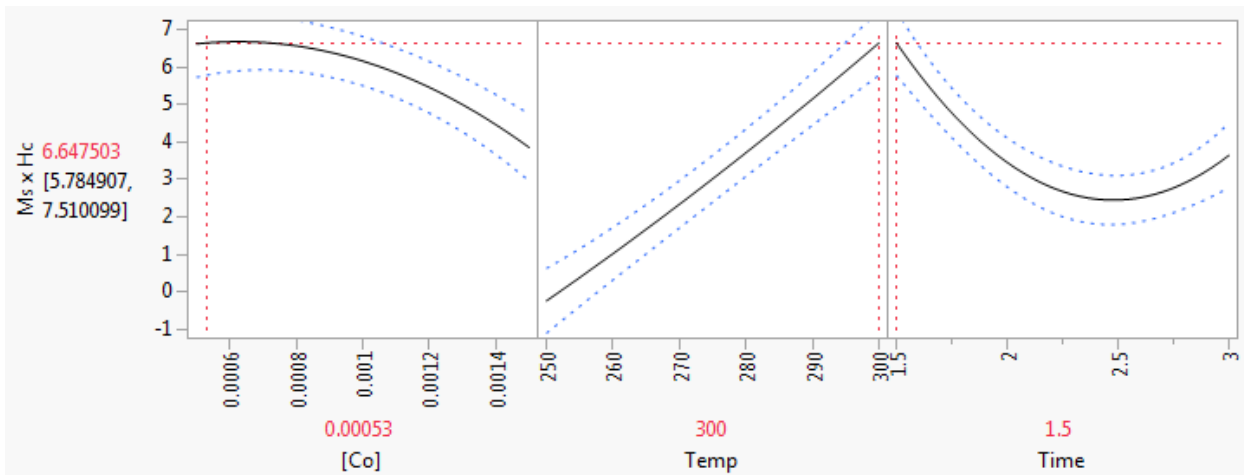


Fig. 4.2.3.2. Prediction profile showing the three factors (reaction time, cobalt concentration, and reaction temperature) optimized to reach the highest response of ideal magnetic product at 6.64 MGOe.

The interactive effect of the parameters is not commonly considered in traditional experiment design methods but in this method it is more observable and ease to allocate. For instance there was a strong interaction between concentration and time explained by the high bar value of $[Co]*Time$ interaction table 4.2.3.2 and very low P-values (<0.0001). Basically, the response function will not be affected by the factors when the P-values are larger than the hypothesis value 0.05.












| Factors Term | Standard Error | t Ratio | Prob> t |
|-----------------------|----------------|--|------------|
| $[Co]*Time$ | 0.047912 |  | $<.0001^*$ |
| $Time*Time*Temp$ | 0.067757 |  | $<.0001^*$ |
| $Time*Time$ | 0.049868 |  | 0.0001^* |
| $Temp(250,300)$ | 0.047912 |  | 0.0003^* |
| $[Co]*[Co]$ | 0.049868 |  | 0.0004^* |
| $Time*Time*[Co]$ | 0.067757 |  | 0.0009^* |
| $[Co]*Temp$ | 0.047912 |  | 0.0040^* |
| $[Co](0.0005,0.0015)$ | 0.047912 |  | 0.0041^* |
| $Temp*Temp$ | 0.049868 |  | 0.0151^* |
| $Temp*Time$ | 0.047912 |  | 0.1172 |
| $Time(1.5,3)$ | 0.033879 |  | 0.4252 |

Table 4.2.3.2. Interaction table showing all the interacting factor terms with respect to probability.

The low $Prob > |t|$; (P-value), of the term factor term $[Co]*Time$ means that the effect of time on response depends on the level of cobalt fumarate concentration. This finding verifies the necessity for longer time with higher concentration synthesis. In fact this explains the suggested mechanism of cobalt carbide chemistry in former literatures, where carbon diffusion rate inside the cobalt crystal is higher with higher cobalt nucleus sites to receive carbon atoms and produce cobalt carbide.^{17,37,49} The critical role of time

observed verified by the low P-value of the second order interaction of both factor terms; *Time*Time*Temp* and *Time*Time* shown at interaction table 4.2.3.2.

From the prediction profile fig. 4.2.3.3 a validation experiment was conducted to verify the optimized conditions of the three factors to verify ideal magnetic product (Y) of 6.64 MGOe. The experimental conditions set to the same conditions in fig. 4.2.3.3 and the response value of ideal magnetic energy product was calculated from sample 18 in fig. 4.2.3.4. From the inset of fig. 4.2.3.4 sample 18 showed coercivity (H_c) of 1258 Oe at and a magnetization (M_s) of 50 emu/g resulted in ideal magnetic energy product of 6.2MGOe. This result is close to the expected response by the prediction model 6.69 MGOe. The slight difference between the prediction profile and experimental results can be attributed to other systematic errors caused from environmental effects.

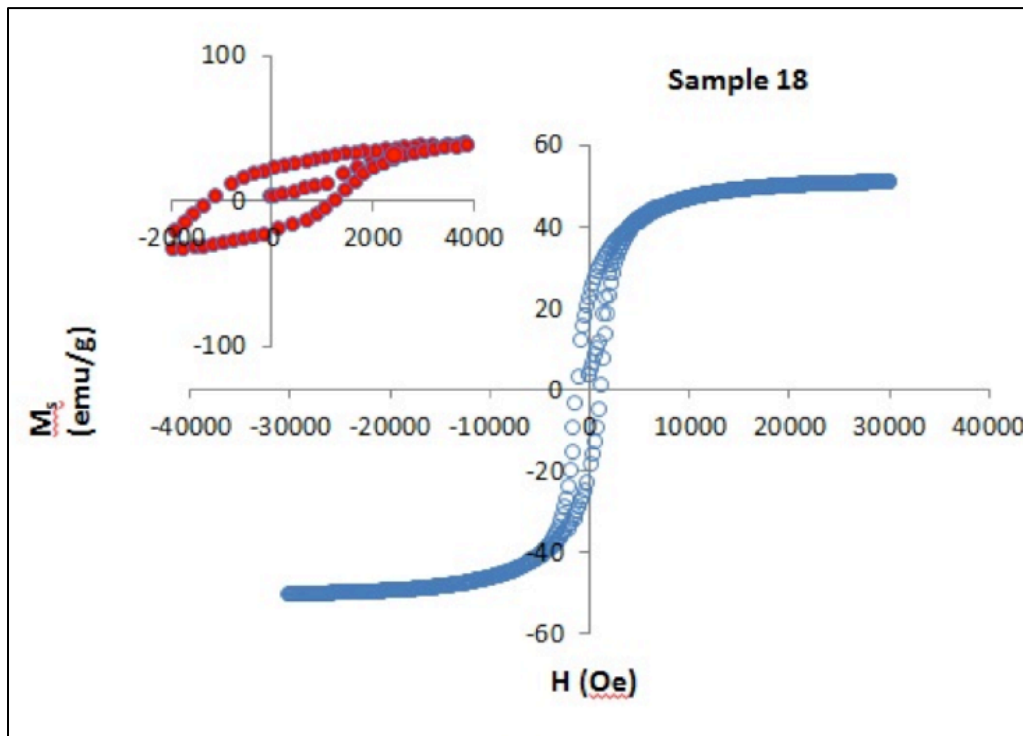


Fig. 4.2.3.4. Hysteresis of the proposed run for optimized factors predicted in fig. 4.2.3.3.

The enhancement of the ideal magnetic energy product in sample 18 explained by the importance of the interaction between time and the low level of cobalt concentration. Since less cobalt concentration is adequate for faster reaction, it is favorable to produce cobalt carbide with low concentration at short time. The critical concentration can be reached with ease reducing the time to reach critical time where nucleation starts fig. 4.2.3.1.

The surface response design characterized by the surface response profile, which provide information about the stationary point. Stationary point can be either; maximum point, minimum point or a saddle point as per fig. 4.3.4.5. This depends on the characterization of the surface response profile for example fig. 4.3.4.5. To explain the stationary point, suppose the levels; $x_1, x_2 \dots x_k$ of interest to optimize the predicted response incorporates curvature of which approximated with a second-order model. Then the stationary point exists at points; $x_1, x_2 \dots x_k$, for the partial derivatives of this point $\frac{\partial y^{\wedge}}{\partial x_1} = \frac{\partial y^{\wedge}}{\partial x_2} = \dots = \frac{\partial y^{\wedge}}{\partial x_k} = 0$.⁵⁴ The surface response profile for the set of responses with the designated factor levels can be approximated in fig. 4.2.3.6. In the former said fig. the surface response profile for Time, [Co] vs the $H_c \times M_s$ (ideal energy product) characterized and showed stationary point of a saddle points behavior. The time with cobalt concentration (Time*[Co] term) was chosen in the surface profile based on the fact that they have shown high probability of interaction than the rest of the factor terms as per table 4.2.3.2.

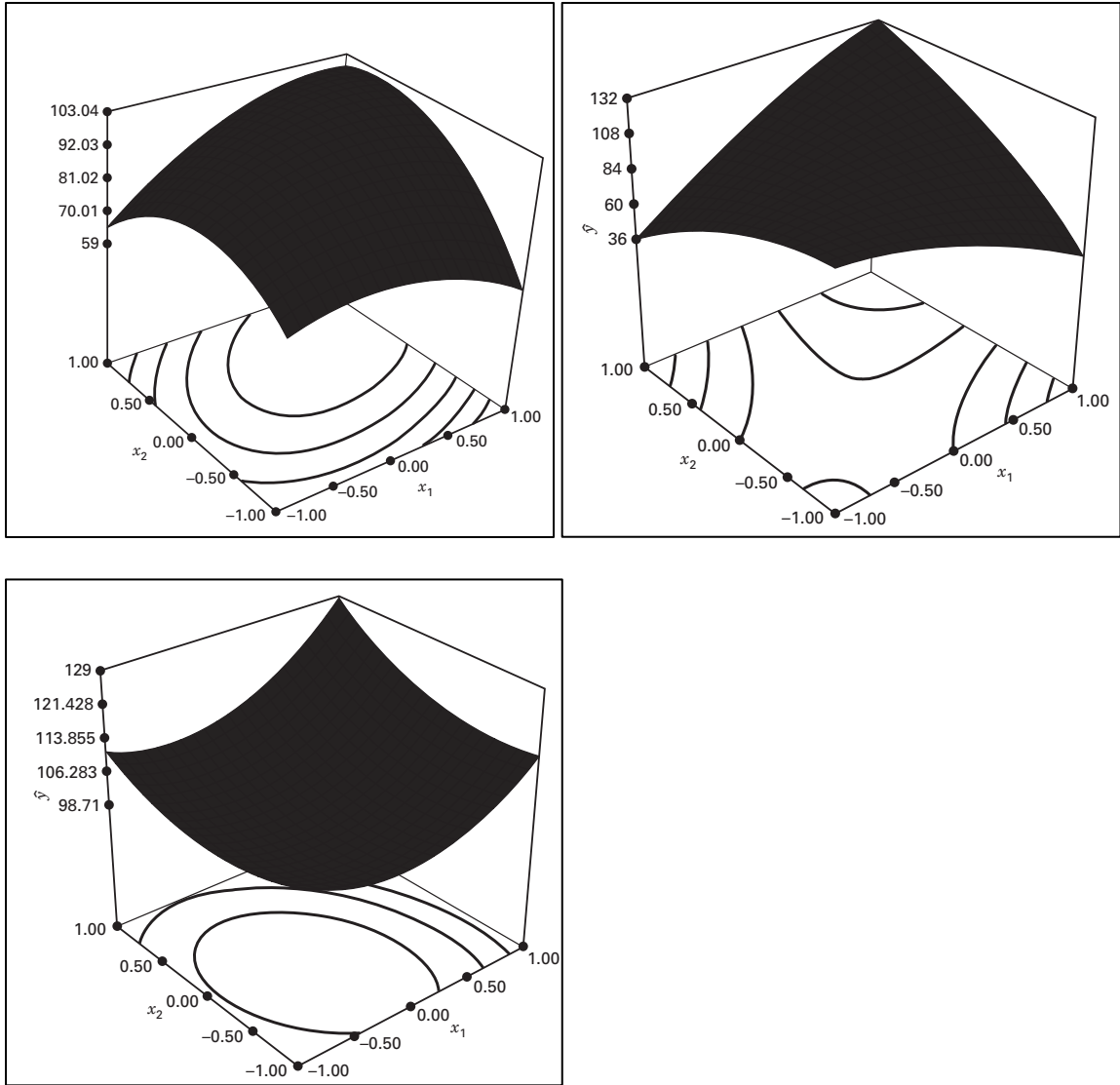


Fig. 4.2.3.5. Stationary points for; maximum response (top right fig.), minimum response (bottom fig.), and saddle point (top right fig.)⁵⁴

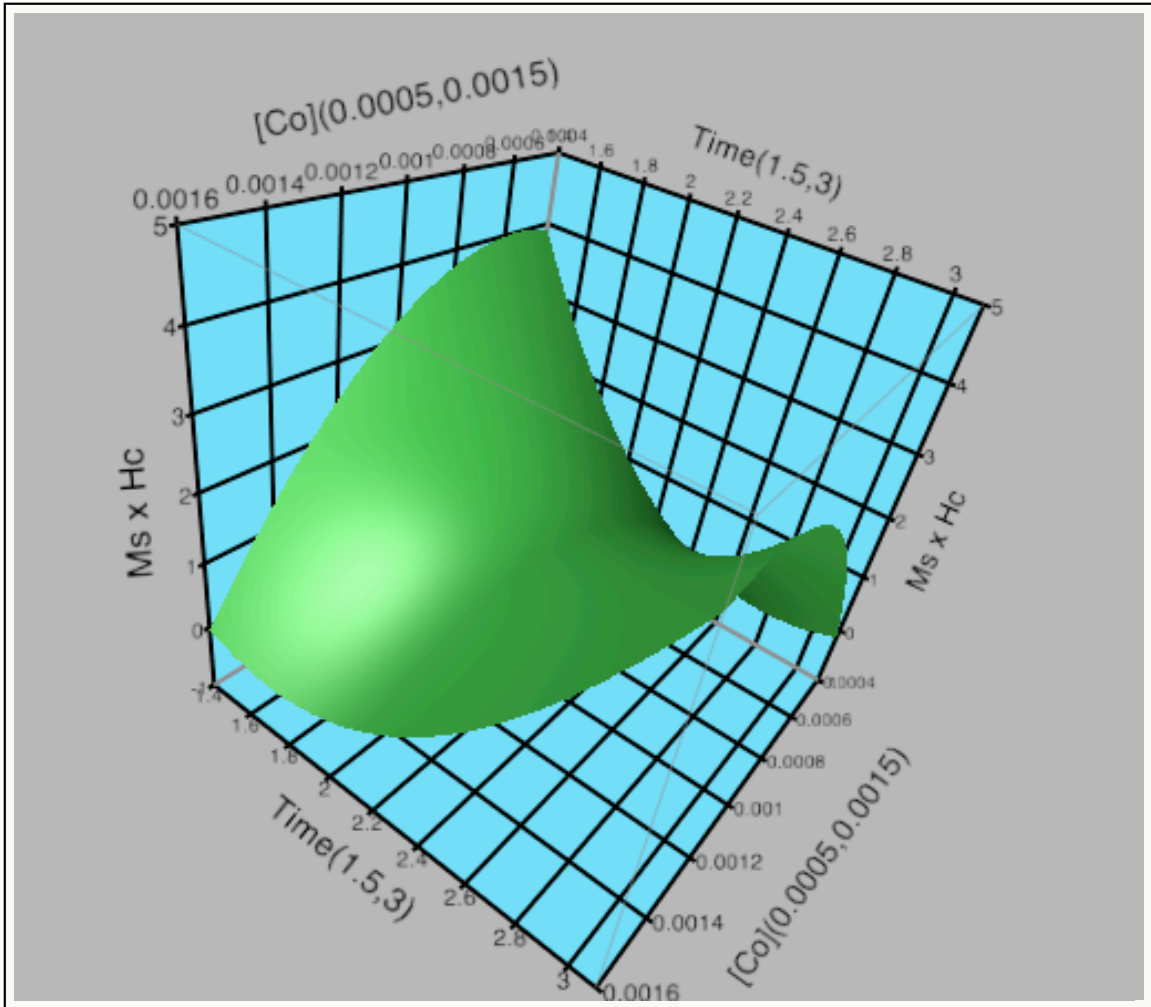


Fig. 4.2.3.6. Surface profile graph showing stationary point of a saddle point in the top corner where reaction time with cobalt concentration level interaction will significantly affect response ($H_c \times M_s$).

The saddle point at the top of graph in fig. 4.2.3.6 for the factors time and [Co] show that response optimization possible when there is excessive decrease in both cobalt concentration and reaction time. On the other side there have been low quantitative values of response in the middle range of cobalt concentration and time factors.

For detailed analysis contour diagram will provide more details of experiment sensitivity to factors.⁵³ Contour profile shows response contours for two factors at a time fig. 4.2.3.7.

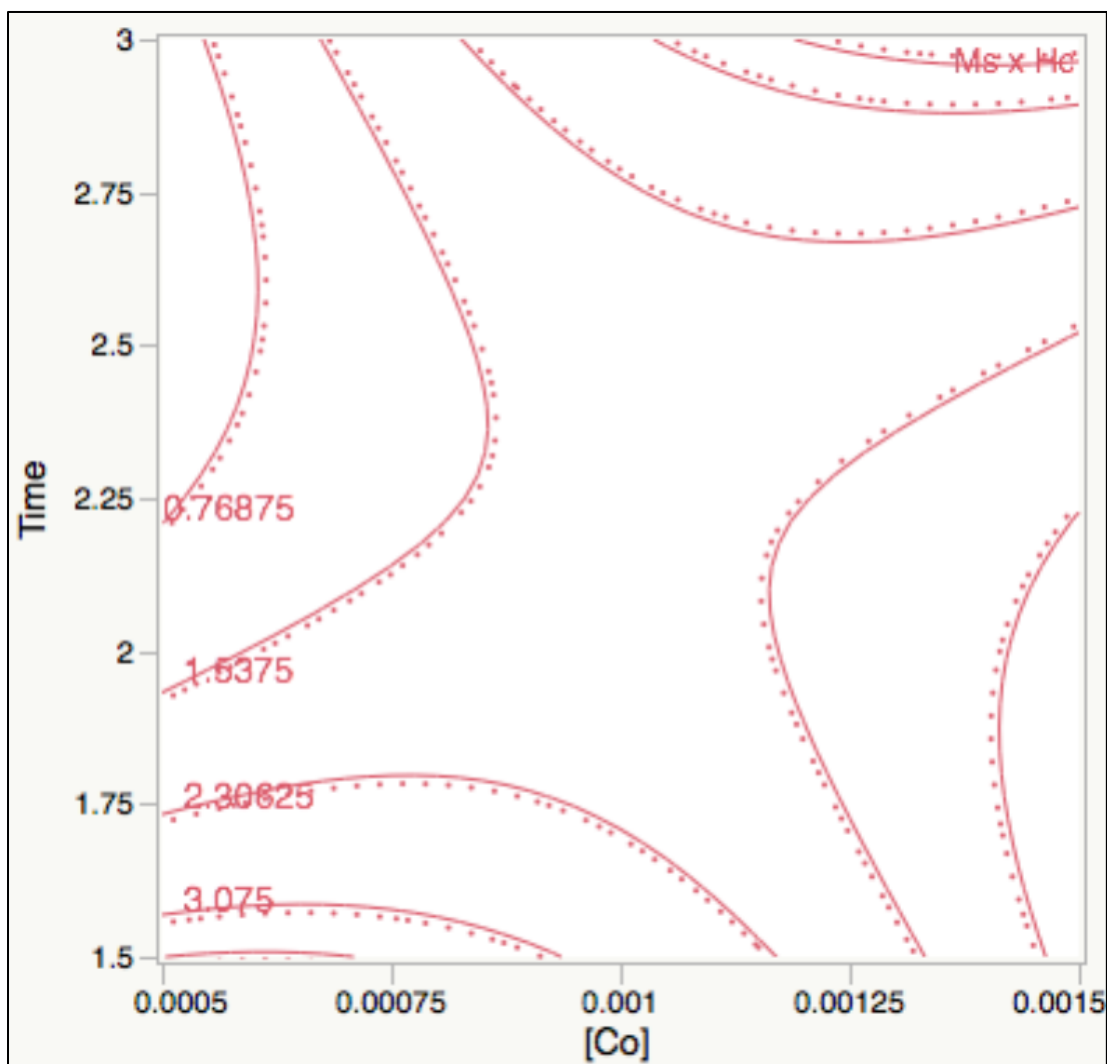


Fig. 4.2.3.7. Contour profile showing two factors ([Co], time) interaction with response ($H_c \times M_s$).

The interactive contour profile is useful for optimizing response surfaces graphically. Cobalt concentration and reaction time plotted with the response ($H_c \times M_s$) as per fig. 4.2.3.7 and reveal that the response ($H_c \times M_s$) is more sensitive to reaction time which comply with the conclusion of the resident time importance when scaling up micro reaction system in flow chemistry at chapter 2. The interaction between the reaction time and cobalt concentration are clearer in the saddle point when observing increase in response ($H_c \times M_s$) as we get close to shorter time and low cobalt concentration.^{52,54,64,65}

Chapter 5. High magnetocrystalline anisotropy of Co_xC (x=2 or 3)

5.1 Introduction

In the last two decades the focus has moved from the micro-crystalline to the nanocrystalline magnetic materials⁶⁶. While the majority of magnetic applications using nanocrystalline materials rely on the soft magnetic properties or those with low coercivities, alternative energy applications require hard magnetic materials or high coercivities.^{56,67} Recently a new class of hard magnetic materials based on nanocrystalline Co_xC ($x = 2$ or 3) have shown promise for these alternative energy applications. Cobalt carbide nanoparticles synthesized using a modified polyol process and described elsewhere.^{37,39,49} These particles show a narrow size distribution, stability against oxidation, larger magnetocrystalline anisotropy, and larger coercivity.

5.2 Experimental

Co_xC is prepared by dissolving 125mg of cobalt fumerate powder in 25 ml of TEG. The reaction solution is heated 300°C for 90 min. Then the reaction was cooled and the product was collected by magnetic separation. Any residual solvent or unreacted salts were removed by washing 3 times with ethanol. Further details are described elsewhere.³⁹

5.3 Results and discussions

In order to carry out a detailed magnetic study of this new class of nanomagnets, first the phase structure was determined using X-ray diffraction and is shown in Fig. 5.3.1. The peaks were analyzed and compared with published ICDD-PDF reference

numbers 00-026-0450 (Co_3C) and 03-065-8206 (Co_2C). Samples did exhibit a multiphase structure consisting of 70% of Co_3C (red arrows) and the remaining 30% Co_2C (blue arrows) phase. The grain size of each phase was determined from full width at half maximum β (FWHM) of the diffraction peaks by means of Scherrer formula $d_{\text{xRD}}=1.0 \lambda/\beta \cos \theta$ [13]. Based on TEM imaging of the nanoparticles (Fig. 5.3.2) they have cylindrical or rod-like shape therefore a shape factor of $K=1$ was used and $\lambda=0.15418$ nm providing an average grain size of the Co_3C and Co_2C nanoparticles amount to 8.5 and 7.6 nm, respectively.

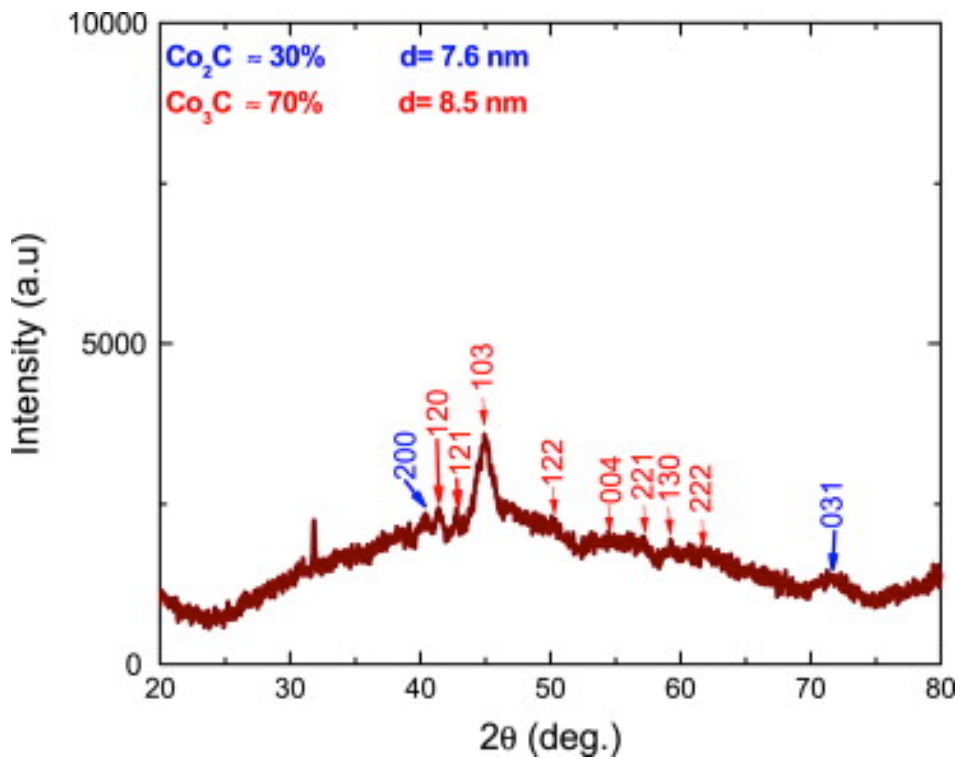


Fig. 5.3.0.1. XRD diffraction pattern for CoC nanoparticles. The crystallite size for each phase has been determined using Scherrer formula. (For interpretation of the references to color in this fig., the reader is referred to the web version of this article.)

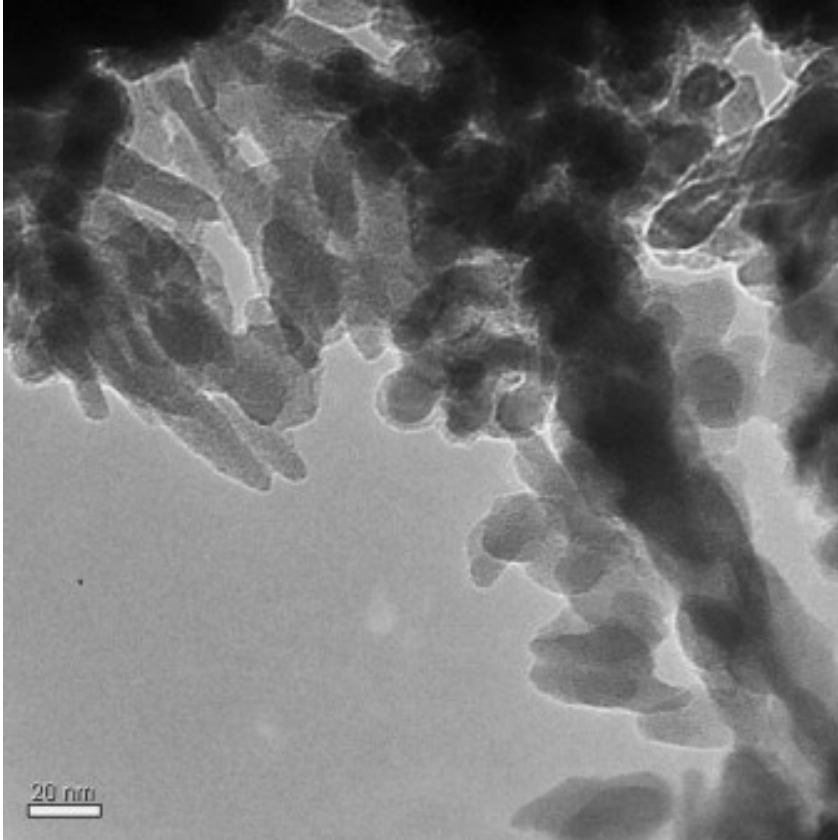


Fig. 5.3.2. TEM images of CoC nanoparticles. The particles shape is rod like particles.

To further study the cylindrical shape of the synthesized Co_xC with XRD more information regarding the length and the apparent size was determined from the XRD peak profile. Since the samples are composed of homogeneous grains appearing in a random orientation, it is possible to determine the shape of the crystals from the powder pattern based on the shape of the reflection domains themselves. From previous published work for a spherical grain of diameter d_{xRD} , the direction of the reflecting plane is unimportant and the apparent size amounts $D=0.75d_{\text{xRD}}$. So, if we define L as the nanoparticle length which is equal to $V^{1/3}=(\pi d_{\text{xRD}}^3/6)^{1/3}$ then by substituting the value of d_{xRD} we get $D=0.93L$ revealing the cylindrical shape assumed before. Hence, the length

and the apparent size of the Co_3C and Co_2C phases yield (6.9, 6.4) and (6.1, 5.7) nm, respectively.

The magnetization dependence of the sample based on the external magnetic field, or hysteresis curves, were collected from -3 T to 3 T and from 50 K to 400 K. In Fig. 5.3.3(a) the hysteresis loops at the various temperatures show a typically ferromagnetic behavior. However, a knee beside the remanence has been observed at temperature ranges from 50 to 250 K.

This knee originated from the decoupling of hard (Co_2C) and soft (Co_3C) phases that can be attributed to the differences in magnetocrystalline anisotropy K_{eff} , magnetization M , and exchange constant A . The strong uniaxial anisotropy associated with the hard magnetic phase is capable of preventing the magnetization reversal of the soft regions.⁴⁹

These two phases are said to be exchange coupled through the inter-granular grain boundaries, which appears strongly at low temperature ranges. In addition it was observed that at 400 K the closed hysteresis loop is obtained suggesting a superparamagnetic behavior.

At this temperature, known as the blocking temperature (T_B), a transition between the ferromagnetic state and the superparamagnetic state occurs. Above this critical temperature, the thermal energy $k_B T$ is higher than the anisotropy energy barrier $K_{\text{eff}} V$ where switching of the magnetization direction between energy minima can occur. This is commonly seen in superparamagnets or spin glass materials. The particles show a quite large H_C , ranging from the small value of 135 Oe at 400 K of the superparamagnetic-like behavior up to the maximum value of 8 kOe at 55 K. The carbide particles do not possess the ubiquitous metal oxide shell as observed in the XRD analysis nor a significant

difference in the magnitudes of the coercivity fields measured at the positive (+ H_C) and negative ($-H_C$) sides. A strong temperature dependence of H_C was observed as shown in Fig. 5.3.3(b).

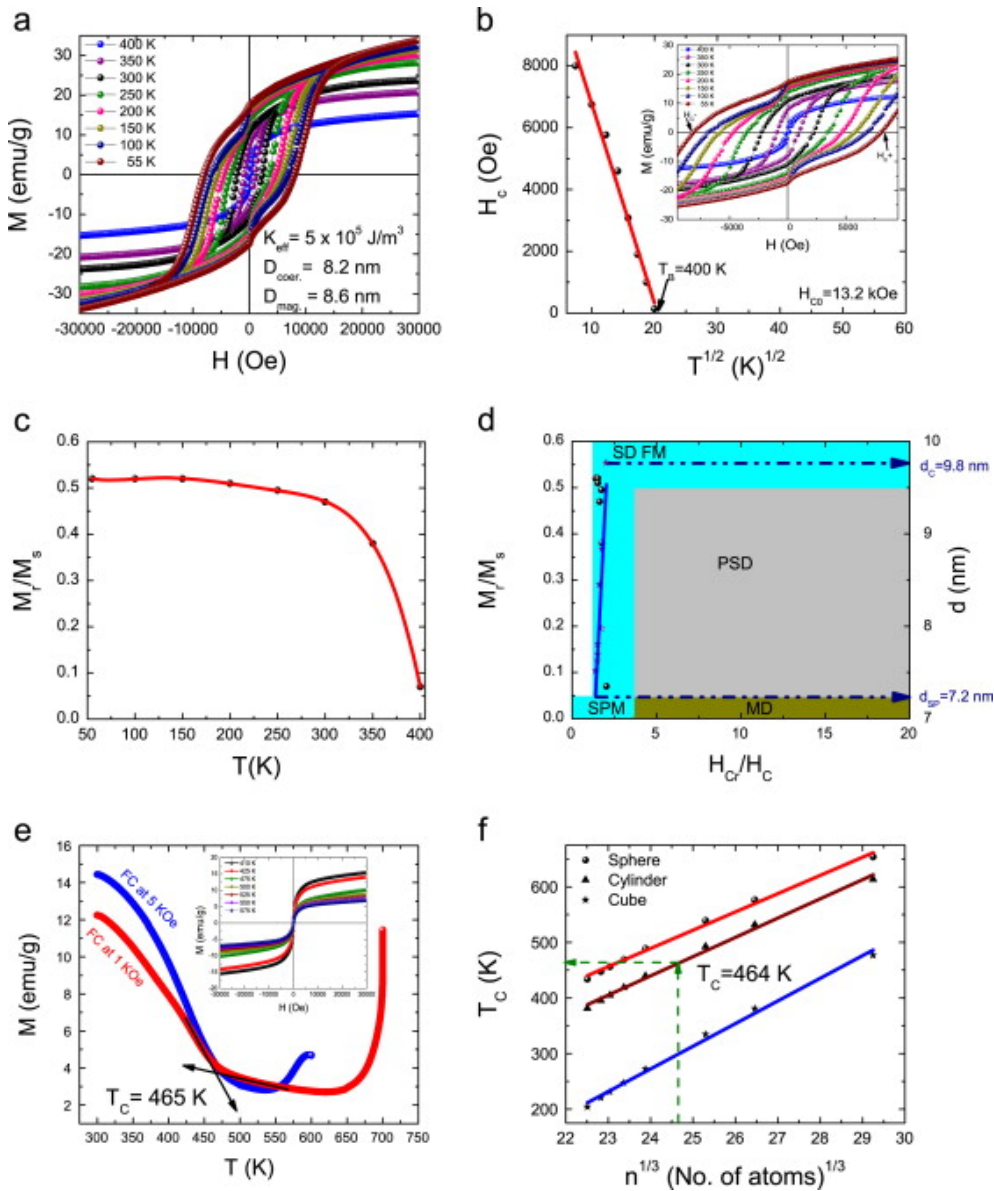


Fig. 5.3.3. Specific magnetic study of Co_xC nanoparticles: (a) Magnetization dependence of an external magnetic field at different temperatures. (b) Coercivity dependence of temperatures (determination of TB at $H_C=0$). (c) Temperature dependent on M_r/M_s ratio reveals uniaxial anisotropy for Co_xC . (d) Magnetic domain phase diagram: determination of Co_xC nanoparticles critical sizes. (e) Temperature dependent on magnetization at $H=1$ and 5 kOe. Inset fig. shows paramagnetic behavior at higher temperature. (f) Calculation of the Curie temperature from the cohesive energy model.

The relation between H_C and $T_{1/2}$ was fitted linearly to reveal information regarding the critical temperature T_B that occurs at approximately zero coercive fields and the coercivity value at zero temperature (H_{C0}). These values amount 400 K and 13.2 kOe for T_B and H_{C0} respectively. By knowing such parameters and assumed to be for the randomly oriented and non-interacting magnetic particles, one can estimate the average effective magnetocrystalline anisotropy K_{eff} which amounts $5 \pm 1 \times 10^5 \text{ J m}^{-3}$.^{4,5}

By substituting the T_B value in the common Brown and Néel equation the average magnetic domain diameter can be determined to be $d_{\text{coer}} = 8.2 \pm 0.8 \text{ nm}$ which reveals a narrow domain size distribution. This value is consistent with the calculated crystallite size from XRD. The biggest particle size can be implied from the magnetization studies by evaluating the initial slopes near the zero field of the M versus H curves. The major contribution to the initial slope arises from the largest particles. Their larger magnetization vectors are more easily oriented by a magnetic field and thus an upper boundary for the magnetic size d_{mag} can be estimated for closed hysteresis at 400 K to be 8.6 nm which approximately corresponds to the d_{coer} determined from H_C as well as the crystallite size determined from XRD. By comparing this size to the d_{XRD} , the crystallinity index should be considered 1 for both Co_xC phases, which indicates the monocrystallinity in our phases. The nature of the magnetization axis uniaxial or cubic anisotropy can be determined by the temperature dependence of the remnant to saturation magnetization ratio (M_r/M_s). From Fig. 5.3.3(c), the M_r/M_s values reveal 0.52 at temperatures $< 250 \text{ K}$ and 0.05–0.5 at temperatures $\geq 250 \text{ K}$. These data imply that our particles are in the uniaxial anisotropy range rather than the cubic anisotropy range which

demands M_r/M_s to equal 0.87. Combining all the obtained data from Fig. 5.3.3(a, b and c) the magnetic domain phase diagram can be obtained as seen in Fig. 5.3.3(d). Fig. 3(d) shows the dependence of the M_r/M_s of the H_{Cr}/H_C where H_{Cr} is the coercive field of the remnant value. The plot shows the distinguished regions for single SD (superparamagnetic SPM and ferromagnetic FM), pseudo (PSD), and multi domain (MD). From the M_r/M_s values, all of our particles lie in the single domain region (SD). After linearly fitting the d_{coer} data the critical size (d_{cr}) which distinguish between the SD and MD, and the superparamagnetic size (d_{sp}) was determined to be 9.8 and 7.2 nm, respectively, which addresses them for the first time for cobalt carbide nanoparticles.

The magnetization dependence of the temperature was measured at constant external magnetic field of 1 and 5 kOe as shown in Fig. 5.3.3(e). The plot shows the ferromagnetic behavior dependence of the temperature and demonstrates the vanishing of the magnetic moment near to 465 K, which is called Curie temperature T_C . At 650 K the magnetic moments start to increase showing paramagnetic behavior following the Curie–Weiss law. This is also clear from the measured hysteresis loops at higher temperature range, which shows a non-saturated magnetization appearing in a paramagnetic behavior (inset fig. of Fig. 5.3.3(e)). In Fig. 3(e), the M – T curve were measured twice at 1 kOe and 5 kOe to indicate that there was no change in the Co_xC structure has been occurred such decomposition of Co_xC to Co as the sample was heated for the 700 K measurements. On the other hand, because T_C value at the nanoscale depends on particle size and shape we can again get information regarding the shape by applying cohesive energy model to our materials (Fig. 5.3.3(f)). As seen from the plot, T_C is showing a linear relation with the

number of atoms that is directly proportional to the particle size for 5.3.3 different shapes such as sphere, cube, and cylinder. By comparing our result to the plot, we have found that our experimentally obtained T_C lies in the range of cylindrical shaped nanoparticles, which is consistent with our postulation in XRD. Also by comparing our particle size result to the plot, we have found that the calculated T_C amounts 464 K, which is in a good agreement with the experimental result.

5.3 Conclusion

Narrow sized single domain Co_xC nanomagnets have been successfully synthesized using a polyol method. The particles show single domain ferromagnetic behavior with nanostructures exhibiting giant coercivity at low temperatures. This unusually large coercivity originates from the large magnetocrystalline anisotropy of the produced particles. The narrow particle size distribution has been observed from the hysteresis, which results in magnetocrystalline anisotropy one order of magnitude larger than the commonly used ferrite nanomagnets. The specific magnetic domain study revealed a magnetic domain diagram with valuable information regarding the superparamagnetic and critical particle sizes that has never been reported in the literature. The blocking temperature and the Curie temperature have been obtained to be approximately 400 K and 465 K, respectively. The T_C dependent on the size based on the number of atoms revealed cylindrical shape for our Co_xC nanoparticles. Thereby, the particles show a ferromagnetic behavior up to 400 K and then superparamagnetic behavior from 400 to 465 K and paramagnetic behavior above 465 K. Such various behaviors at different temperatures can be tailored for application in magnetic sensors as

well as permanent magnets. In addition the obtained high magnetic signal from the large magnetic anisotropy can be utilized for contrast enhancement for MRI diagnostic techniques.

Chapter 6. Co_xC (x= 2 or 3) synthesis using nucleating agent

6.1 Overview/Motivation

Various ways reported possible crystallinity control for cobalt carbide.^{17,33,39} Nucleating agents such as Ru, and Pt has shown importance in controlling shape of magnetic nano composite (MNC) particles.^{13,14} However, due to the high cost of these nucleating agents it was not practical to apply it in flow chemistry when attempting to produce cobalt carbide in microrreactor technology. Also adding expensive nucleating agents such samarium, ruthenium, and platinum would not augment other properties whereas investigating other nucleating agents such as noble metals would possibly show surface plasmon resonance beside the magnetic properties.^{45,68-70}

Lack of fundamentals investigation on nucleating agent affecting the process of producing cobalt carbide gave motive to consider different nucleating agents. Conversely, some literatures showed convalesce shape anisotropy and magnetocrystalline for cobalt nanoparticles when using nucleating agents such as rathuinium.^{13,22,71} To our knowledge no statistical study has been conducted to facilitate and explain the mechanism of nucleating agent with respect to Co_xC coercivity strength. It is interesting to test the nucleating agent concentration with respect to other experiment factors by means of statistical routes.^{13-15,22,49} A systemic study is needed to provide comprehensive knowledge to reveal experimental conditions that can be applied to a flow chemistry approach to produce cobalt carbide. It is also important to compare and study different nucleating agents that would possibly alter different behavior on magnetic properties of cobalt carbide. For example, some nucleating agents develop the properties of

ferromagnetic material either as a function of coercivity or as a function of magnetization.^{13,49,72}

Heterogeneous nucleation theory may be applied to get more understanding and explain the behavior of nucleating agent.^{24,61,63,73} The heterogeneous nucleation reduces the Gibbs energy needed during the particles formation process providing advantageous when compared to homogeneous nucleation. Also it has been shown that studies heterogeneous offer shape control as will.^{20,22,59,61}

Investigating the variation of nucleating agent to precursor concentration ratio can lead to information on experimental conditions governs the formation of bimetallic or core-shell nanoparticles.^{16,74} The outcome of this knowledge the right concentration of nucleating agent can be applied to get higher yield of cobalt carbide without forming unwanted product. This delivers information on magnetic interaction behavior between the nature of metallic nucleating agent and the magnetic source from the transition metals.^{26,70,75} The antiferromagnetic-ferromagnetic core-shell material has shown interesting magnetic interaction resulting in exchange bias and increasing the coercivity.^{2,15,16,24,76} Nucleating agents at bulk have different properties before reduced to nanoparticle size. For instance silver if used as nucleating agent will be diamagnetic in bulk and paramagnetic at nanosize.^{72,77} Magnetic properties of nucleating agents is important to be studied at the nanoscale since at bulk scale it will display tremendously different magnetic characteristics. For instance silver at bulk indicate diamagnetic behavior while at nanoscale it reveal paramagnetic behavior. Silver carbon nanocomposite have shown weak ferromagnetic behavior properties at room temperature 103 Oe.⁷⁷ Silver nanoparticles exhibited stability with the presence of long chain capping

agents such as PVP, and oleic acid that stabilize the active sites of silver nanoparticles.^{69,78}

Magnetic Au_{Core}-Core_{shell} nanoparticles produced by first producing gold precursor nanoparticles then slowly injecting a mixture prepared in gloves box of Co₂(CO)₈ in toluene with extra oleylamine and oleic acid into the suspended gold nanoparticles in toluene.¹⁰ It would be interesting to study the formation of gold or silver nanoparticles in situ during cobalt carbide formation especially that its of ease to control the shapes of gold and silver when compared to other elements.⁶⁹

The growth of noble metals was studied extensively by the investigation of two different metals interfacial in core shells. The lattice mismatch governs the growth of Pt/Au also between Pt/Pd. The higher degree of mismatch in Pt/Au (4.08%) prevented conformal overgrowth on Pd whereas for Pt/Pd mismatch was less (0.77%) allowing overgrowth on the metal.^{68,79}

Both silver and gold fall under face centered cube (FCC) class with fully occupied d-band and very close lattice constants 0.288 nm for the nearest-neighbor distance on Au (1 1 1) and 0.289 nm for Ag (1 1 1). Submonolayer cobalt was deposited on Ag using e-beam evaporator to study the Co island nucleation on the Ag (1 1 1) substrate. There were adequate results from scanning tunneling microscopy (STM) proving that Co growth resulted from an exchange process between Ag defect sites at the elbow and Co adatoms. It was observed that Co mobilization was possible even at room temperatures in the case of using Ag (1 1 1) on the defected elbows. However, Co-Ag alloy produced at higher temperatures 343 K when growing Co at Ag (1 0 0).⁸⁰

6.2 Introduction

Various studies have shown that controlling the crystallinity of cobalt carbide is possible through varying the base.^{17,33,39} Hydroxide to cobalt metal ratio have shown the ability to control the cobalt phase when varying hydroxide in polyol media as per fig.6.2.1.⁵⁹ The high crystallinity is important as it impact the magnetocrystalline resulting in a boost in magnetic property. Other route to enhance anisotropic of cobalt nanorods is by introducing solid host template to direct the growth. In porous alumina matrix, hexagonal mesoporous silica, or carbon nano tube, cobalt and nickel nano wires can be produced.^{14,15,17}

The selective coordination of hexadecylamine on the metal surface allowed the synthesis of nanometer-sized nickel rods.^{59,76,81} In previous literatures the addition of OH⁻ showed that it could slow down the reaction and growth rate allowing more carbon incorporated inside the cobalt metal crystal structure.^{20,35,399,17,33,37-40} This approach will assist the role of TEG as capping agent increasing the acetyl aldehyde role. The reaction time will still be vital to influence growth whereas looking into alternative methods to develop reaction with lower reaction temperature and shorter time is cost effective for flow chemistry application.

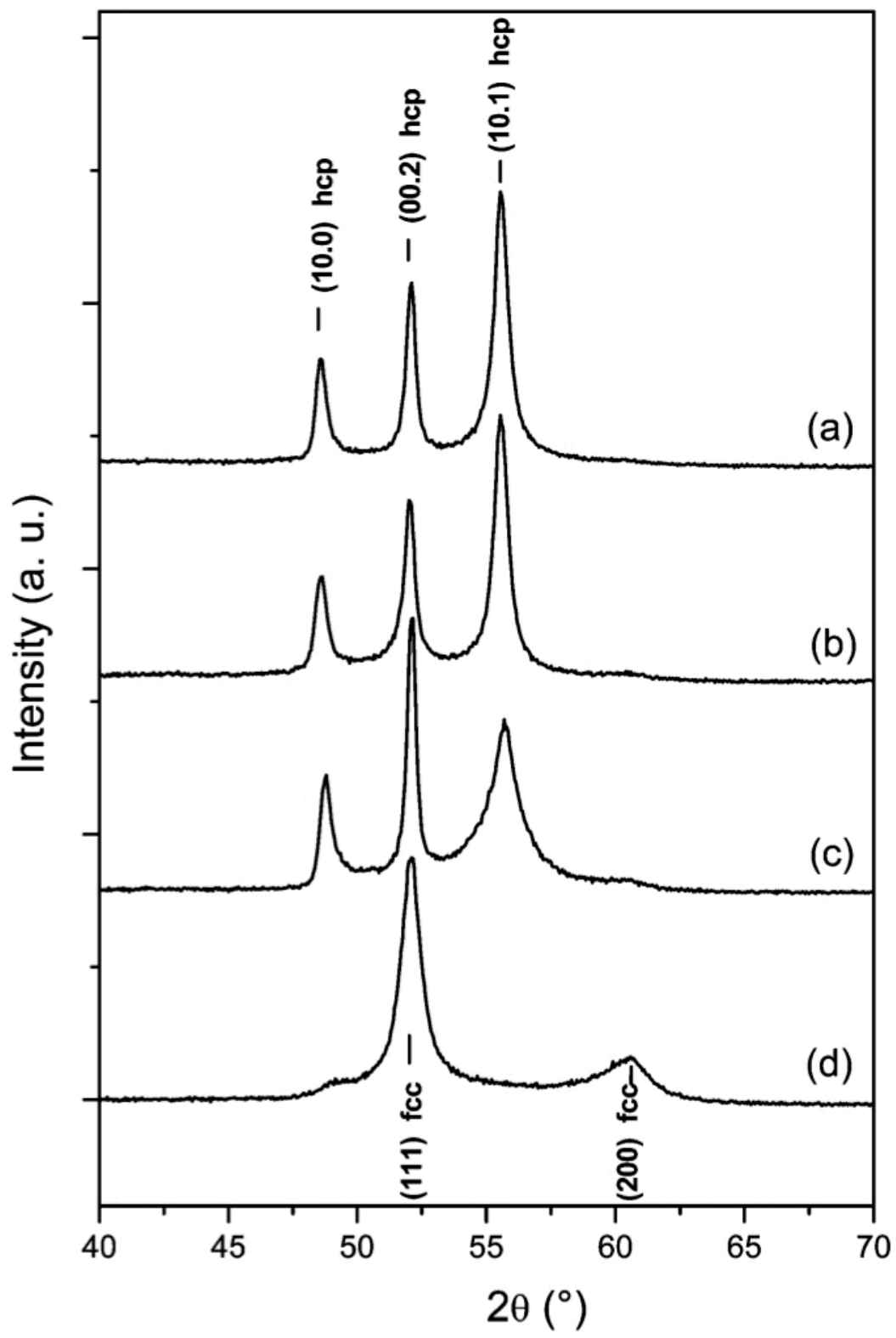


Fig. 6.2.1. The increase of [OH⁻]/[Co] ratio shifted cobalt from hcp phase to fcc.⁵⁹

In chapter 4 qualitative studies provided basic results from software model fit. The result of the study determined that there was a strong interaction between time and cobalt concentration. The fact that growth of Co on Ag (1 1 1) has been successful in other literatures made it worth of studying Ag as nucleating agent for the cobalt carbide mobilization. In addition, the possibility of mobilizing Co nucleus on Ag nucleating sites altered by the defection in the surface at room temperature made it promising candidate as nucleating agent.⁸⁰

In this chapter the goal is to develop optimized approach that can obtain enhanced Co_xC in polyol route assisted by Ag nucleating agent concentration experimental design. Comparison of optimization of cobalt carbide without and with the nucleating agent will give an idea about the critical conditions when applying the reaction to MMRS for flow chemistry and conceivable beneficial of applying Ag nucleating agent. In previous optimization study at chapter 4 it was indicated that the metal concentration of cobalt precursor along with reaction time would have high impact on the magnetic energy product. This is related to the nucleation and growth mechanism plateau of the cobalt nucleus when reduced by TEG. The strong interaction between time and cobalt precursor concentration directed the focus towards investigating other mechanisms to reduce the amount of expensive cobalt material and reduce the temperature to get enhanced magnetic properties with high yield. The criticality of controlling growth mechanism is related to the fact that it is important to drive both magnetocrystalline and shape anisotropy. Controlling the growth mechanism attained by involving the nucleating agent to provide heterogeneous growth.^{22,24,61,80} Different nucleating agents based in their atomic radius provides different pattern for metal growth.^{34,61}

This requires investigating different nucleating agent that aim potential reduction in time or temperature. Also, investigating the significance of cobalt precursor concentration increases for conceivable higher cobalt carbide yield.

The JMP showed that with homogenous nucleation by using straightforward method of producing cobalt fumarate in TEG would require either two scenarios; 1) low concentration of cobalt precursor with short reaction time, 2) high cobalt precursor with long reaction time. Silver has shown easy control on shape and size in polyol synthesis.^{69,70,78} The reaction temperature factor is vital in controlling the shape of silver nanoparticles.^{69,79}

6.3 Experimental methods

6.3.1 Synthesis

Tetraethylene Glycol (4-EG) was stored in dry environment by the addition of 3Å molecular sieves to prevent any water contamination in the stored bottles. In typical reaction steps (0.5 mM, 17 mM, or 8.75 mM) of silver nitrite (AgNO_3) dissolved in TEG and ramped to 160°C under magnetic stirring then (59 mM, 49 mM, or 39 mM) of cobalt fumarate ($\text{C}_4\text{H}_2\text{CoO}_4 \cdot \text{H}_2\text{O}$) added immediately, then the reaction kept at (270°C, 285°C, 300°C) for desired time (1 hr, 2hrs, or 3 hrs) experiment set up shown in fig. 6.3.1.1. The yellow solution observed before adding cobalt fumarate indicates suspended Ag NPs rods in the solution which is formed at 160°C.⁶⁹

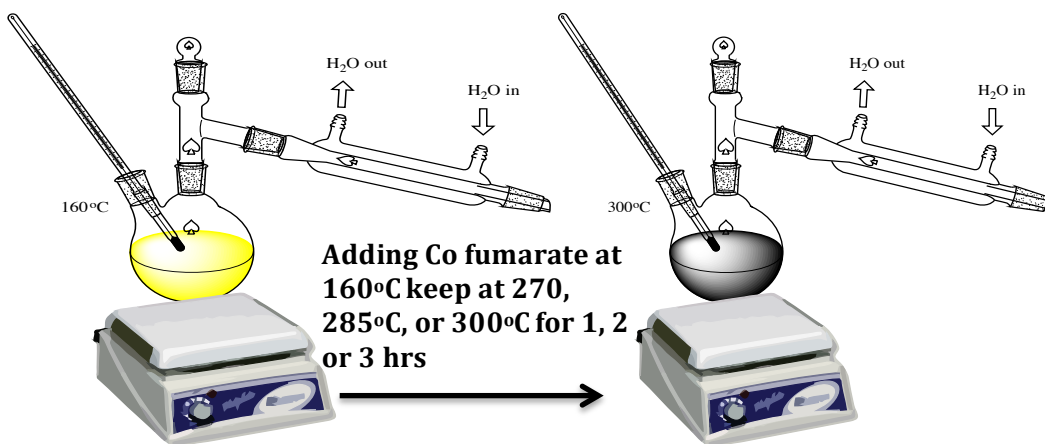


Fig. 6.3.1.1. Reaction scheme of synthesising cobalt carbide in polyol media using seed silver nanoparticles.

The product was collected at the end of the reaction time and left to cool down at room temperature, which approximately take 20 minutes. Once the solution reached room temperature, the product was rinsed under sonication three times with methanol and separated magnetically with rare earth magnetic bar.

6.3.2 JMP design of experiment

Using JMP 11 design of experiment was set using surface response method using reaction time (T), reaction temperature (Temp), concentration of AgNO_3 ([Ag]), and concentration of $\text{C}_4\text{H}_2\text{CoO}_4 \cdot \text{H}_2\text{O}$ ([Co]) as three leveled factors as per table 6.3.2.1. The surface response design allows estimating the interaction and quadratic effects between the nucleating agent concentration [Ag] and precursor concentration [Co] with respect to time and temperature. Furthermore, this will give the ability to display information about the shape of the response surface between these factors and offer the

benefits of; finding improved or optimizing process settings, investigating process problems and weak points, possibly give the experiment exemption against uncontrollable influences making the process more robust.

Concentration of AgNO_3 effect on the growth mechanism of cobalt carbide has never been studied. In previous literatures the ability to provide heterogeneous growth of Co on Ag (1 1 1) at the defected sites provided motivation to study the variation the both Ag and Co concentrations.^{22,80} Temperature has also showed critical role in controlling the growth of Co islands on Ag (1 1 1) and also controlling the corrugation shape of Ag silver nanoparticles, inasmuch temperature has been playing significant part in cobalt carbide formation.^{49,61,80}

Coercivity selected to be the response for design of experiments results. When using varied concentration of noble metals such as Ag or Au, it is expected to result in diminishing magnetization unfortunately. At the same time due to possible shape or magnetocrystalline anisotropic control, the macroscopic coercivity can attain enhancement at room temperature.^{10,69,75,82}

6.3.3 Characterization

PANalytical X'Pert Pro MPD diffractometer using $\text{Cu K}\alpha$ ($\lambda=1.5418 \text{ \AA}$) radiation used to accomplish crystal structure Analysis. X'Pert Highscore analysis software used to perform analysis of collected X-Ray Diffraction (XRD) scans. Phase composition and peak widths were determined as a result of Reitveld refinement using space groups and lattice parameters from literature.⁸³

| | Temp | [Ag] | [Co] | Time | H _c |
|----|------|---------|-------|------|----------------|
| 1 | 300 | 0.0005 | 0.059 | 1 | 2400 |
| 2 | 300 | 0.017 | 0.059 | 3 | 1075 |
| 3 | 300 | 0.0005 | 0.059 | 3 | 681 |
| 4 | 270 | 0.00875 | 0.049 | 2 | 793 |
| 5 | 270 | 0.017 | 0.039 | 1 | 680 |
| 6 | 300 | 0.017 | 0.039 | 3 | 466 |
| 7 | 270 | 0.017 | 0.059 | 3 | 617 |
| 8 | 270 | 0.0005 | 0.039 | 3 | 2622 |
| 9 | 285 | 0.017 | 0.049 | 2 | 268 |
| 10 | 285 | 0.00875 | 0.049 | 1 | 822 |
| 11 | 285 | 0.00875 | 0.049 | 2 | 688 |
| 12 | 300 | 0.0005 | 0.039 | 3 | 2700 |
| 13 | 270 | 0.017 | 0.059 | 1 | 840 |
| 14 | 285 | 0.00875 | 0.039 | 2 | 400 |
| 15 | 300 | 0.017 | 0.059 | 1 | 663 |
| 16 | 285 | 0.00875 | 0.049 | 3 | 790 |
| 17 | 285 | 0.0005 | 0.049 | 2 | 853 |
| 18 | 285 | 0.00875 | 0.059 | 2 | 2826 |
| 19 | 270 | 0.0005 | 0.039 | 1 | 293 |
| 20 | 300 | 0.017 | 0.039 | 1 | 650 |
| 21 | 270 | 0.017 | 0.039 | 3 | 315 |
| 22 | 285 | 0.00875 | 0.049 | 2 | 617 |
| 23 | 270 | 0.0005 | 0.059 | 3 | 200 |
| 24 | 270 | 0.0005 | 0.059 | 1 | 560 |
| 25 | 300 | 0.00875 | 0.049 | 2 | 667 |
| 26 | 300 | 0.0005 | 0.039 | 1 | 367 |

Table 6.3.2.1. Surface response design table showing three factors; time, temperature, [Ag], and [Co]. Also, coercivity H_c was chosen as response.

Crystal grain size was determined using the Scherrer Calculator in X'pert Highscore Plus.

Transmission electron imaging and analysis was conducted on a Zeiss Libra120 with an

accelerating voltage of 120 kV. Vibration Sampling magnetometry (VSM) measurements was applied shown high coercivity and relatively low magnetization.

6.4 Results

6.4.1 Proposed mechanism

The starting reaction of AgNO_3 in TEG has shown a yellowish color at 160°C indicating the formation of silver nanoparticle spheres.²⁸ This temperature is chosen for next step; hot addition of cobalt fumarate. At this temperature, silver nanoparticle shapes will experience highest surface energy thus, offer increase in nucleate sites population at the surface of silver nanoparticles (Ag NPs). This assists the incorporation growth of critical size cobalt nucleus on the heterogeneous surface of Ag NPs encouraged by the fact that Co metal NPs will struggle to reduce Gibbs energy on other surfaces fig. 6.4.1. Furthermore, the surface of Co during growth at Ag nucleation sites will have surface reconstruction with active carbon atoms incorporated in the crystal lattice.^{33,37}

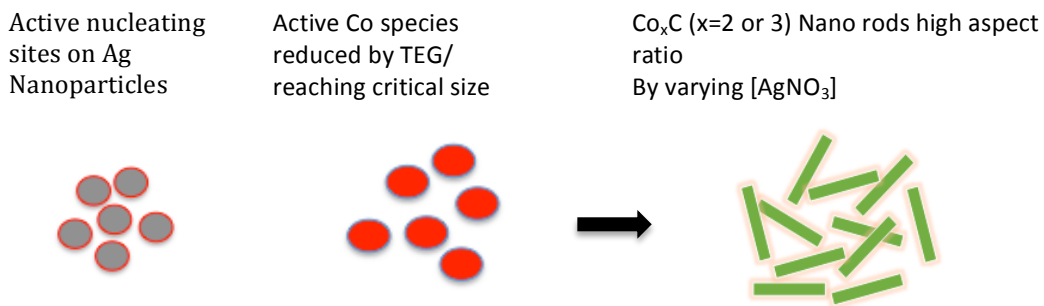


Figure 6.4.1. Schematic show the mechanism heterogamous growth of cobalt carbide controlled shape assisted by the nucleation sites of silver nanoparticles.

The silver nanoparticles at the selected hot addition temperature (160°C) displayed high surface energy and more control on particles shape.^{69,78} Temperatures higher than 160°C exhibited various silver nanoparticles shape can be indicated by a gray color of the solvent making it difficult to control silver nanoparticles facets at temperatures higher than 160°C even with the presence of strong capping agent such as PVP as been reported in other studies.⁷⁸

Other interesting difference observed from previous synthesis routes to produce Co_xC without nucleating agents is that upon the addition of cobalt fumarate, the solution turned into brownish color directly without going through the purple color.^{33,39} This indicate that the rate of carbon diffusion on the surface was increased. Cobalt known to have slower carbon diffusion rate to produce carbide than iron, this was revealed from catalyst deactivation study when cobalt catalyst was poisoned with carbonization.⁴⁰

Silver nanoparticles have shown that the highest energy facets tended to overcome that energy by blocking the growth with high polarity capping agents such as cationic CTAB, and PVP.^{46,69,78} It was shown recently that the polymer capping reagent of PVP will provide uniform particles during seeding process.⁷⁸

6.4.2 Model fit

The results represented in table 6.3.2.1 reveal variation in the coercivity values when changing experimental conditions with their respected levels for each factor.

Quick screening of table 6.3.2.1 reveals the highest coercivity for sample 18 (3kOe) at the following conditions; temp 285°C, time 2 hrs, cobalt precursor concentration 0.059M and silver nitrite concentration of 0.00875M. The summary of the 26 runs for coercivity

(H_c) as a function of each factor with respect to all three levels for each factor demonstrated at figures 6.4.2.1 – 6.4.2.4.

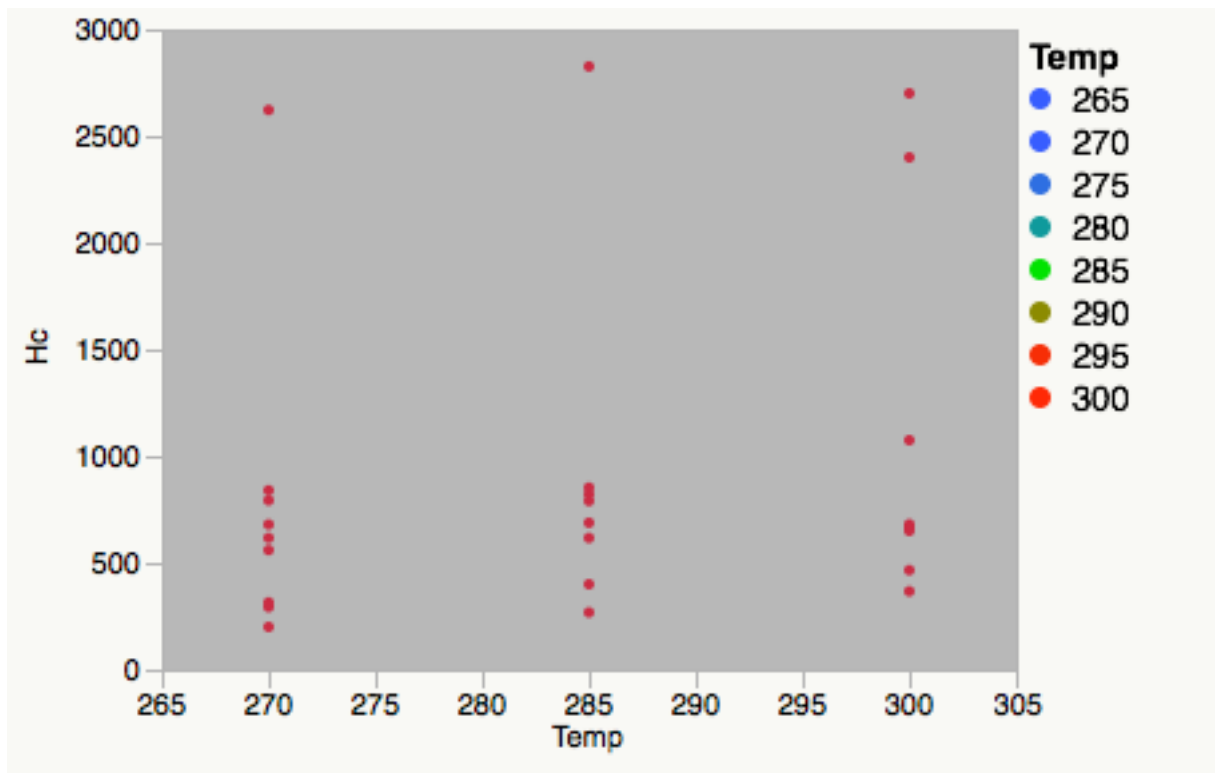


Figure 6.4.2.1 Fit Y by X from JMP software showing the regression of H_c (Oe) vs Temp. ($^{\circ}\text{C}$) Where H_c can possibly be highest at 285°C around 3kOe .

In figure 6.4.2.1, highest coercivity (3kOe) achieved at 285°C . This temperature was lower compared to previous reports when producing Co_xC . Coercivity was high without the need of reaching TEG boiling point (310°C).^{37,39,49} The presence of 0.0005 M of AgNO_3 figure 6.4.2.2 operated Ag NPs to offer heterogeneous nucleation sites for Co_xC nucleus to reach coercivity of 3kOe . This reduction in temperature has advantageous for scale up when using MMRS. At higher temperatures the coercivity can reach up to 2.5kOe figure 6.4.2.1 but on the cost of elongated reactions figure 6.4.2.2.

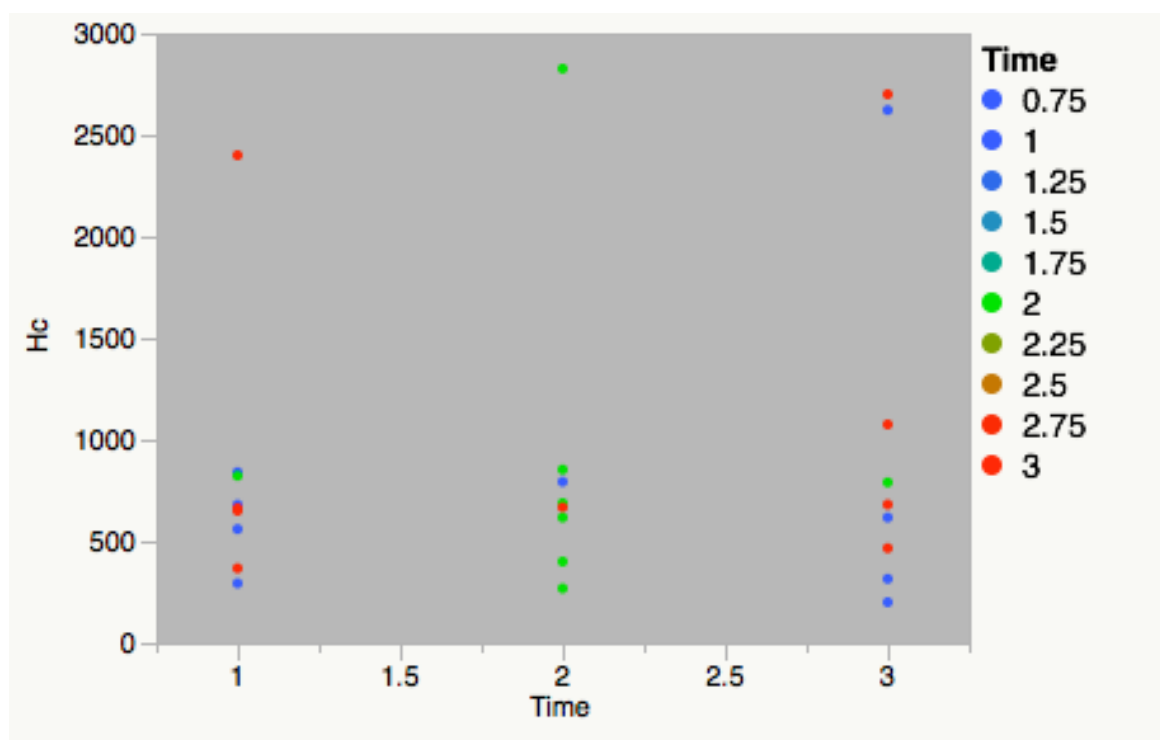


Figure 6.4.2.2 Fit Y by X from JMP software showing the regression of H_c vs Temp. Where H_c reaches 3kOe at 3 hours and 2.5kOe at 1 hour.

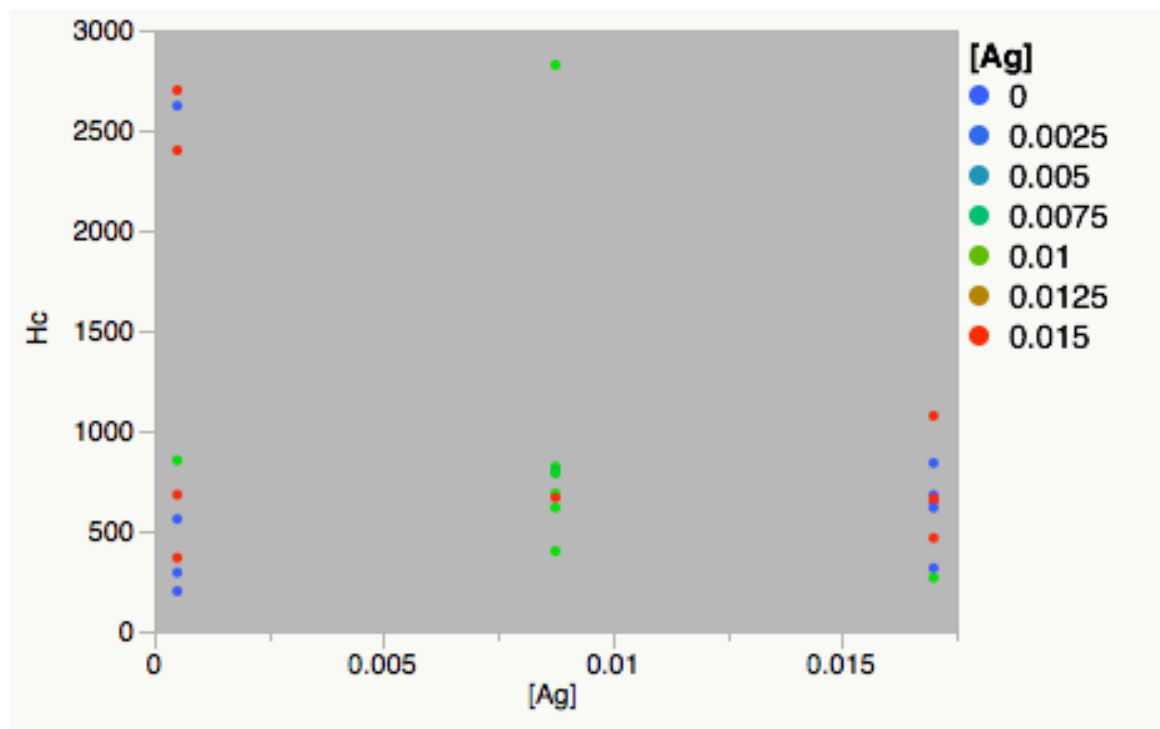


Figure 6.4.2.3 Fit Y by X from JMP software showing the regression of H_c (Oe) vs $[Ag]$ (M). Where H_c can possibly as high as 3kOe when silver concentration is low.

Figure 6.4.2.3 supports findings of DoE done of cobalt carbide without using nucleating agent earlier in chapter 4.

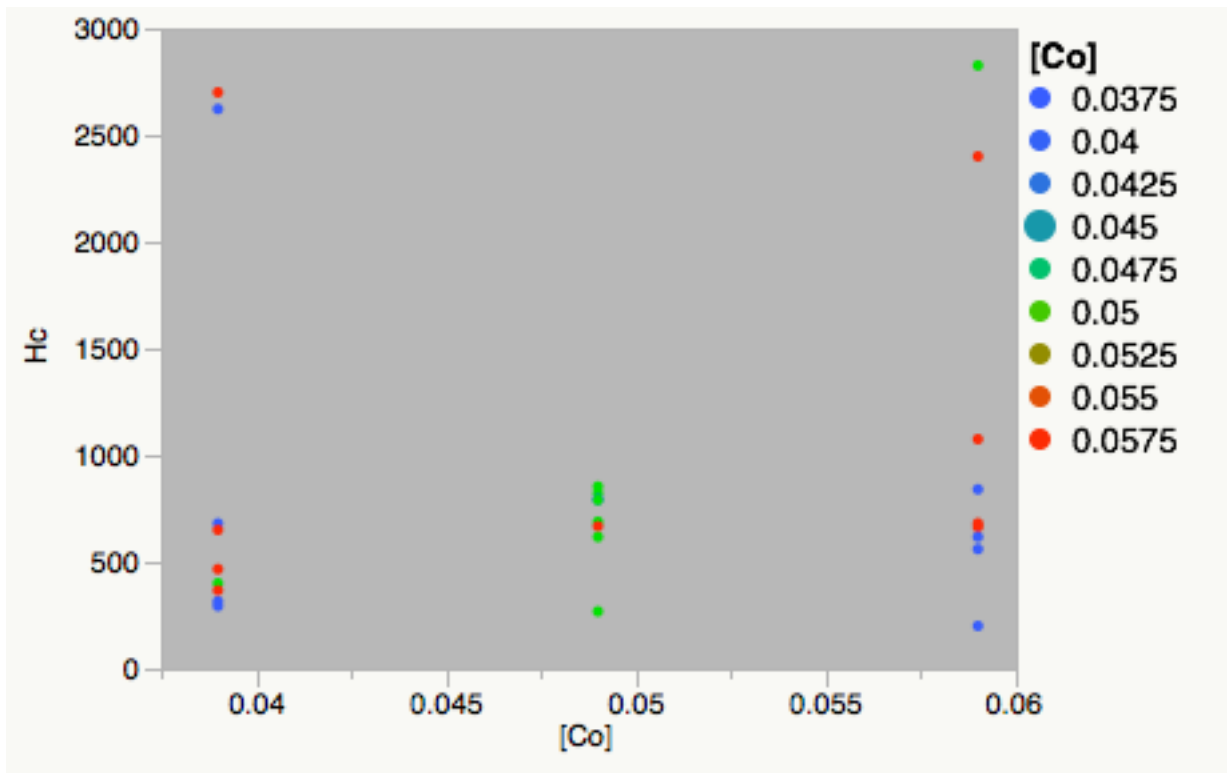


Figure 6.4.2.4 Fit Y by X from JMP software showing the regression of H_c vs Temp. Where H_c can possibly be highest at low and high cobalt concentrations.

Using nucleating agents have enhanced the coercivity of cobalt carbide when compared to the study at chapter 4 or earlier reports.^{33,37}

Table 6.4.2.1 shows the parameter estimates, where the estimates of the model parameters and, for each parameter, gives a t test for the hypothesis that it equals zero. The source column will show the terms, which is a set of factors combined. The strength of their interaction is measured by the P-value shown in the Prob > F column table 6.4.2.1. Prob>F gives the P-value for the effected test of; the p-value is a function of the detected sample results (a test statistic) qualified to the surface response statistical model,

which measures how extreme the observation is. The p-value is the probability that the observed result has nothing to do with what the actually test for.

| Effect Tests | | | | | | |
|--------------------|-------|----|----------------|---------|----------|---------|
| Source | Nparm | DF | Sum of Squares | F Ratio | Prob > F | |
| Temp(270,300) | 1 | 1 | 93038.1 | 0.6499 | 0.4467 | |
| [Ag](0.0005,0.017) | 1 | 1 | 700655.9 | 4.8939 | 0.0626 | |
| [Co](0.02,0.03) | 1 | 1 | 517890.1 | 3.6173 | 0.0989 | |
| Time(1,3) | 1 | 1 | 2514311.4 | 17.5619 | 0.0041* | |
| Temp*[Ag] | 1 | 1 | 268065.1 | 1.8724 | 0.2135 | |
| Temp*[Co] | 1 | 1 | 339015.1 | 2.3679 | 0.1677 | |
| [Ag]*[Co] | 1 | 1 | 650039.1 | 4.5404 | 0.0706 | |
| Temp*Time | 1 | 1 | 24945.8 | 0.1742 | 0.6889 | |
| [Ag]*Time | 1 | 1 | 4035694.7 | 28.1884 | 0.0011* | |
| [Co]*Time | 1 | 1 | 2252250.6 | 15.7315 | 0.0054* | |
| Temp*Temp | 1 | 0 | 0.0 | . | . | LostDFs |
| [Ag]*[Ag] | 1 | 0 | 0.0 | . | . | LostDFs |
| [Co]*[Co] | 1 | 1 | 1308240.9 | 9.1378 | 0.0193* | |
| Time*Time | 1 | 0 | 0.0 | . | . | LostDFs |
| Temp*Temp*[Co] | 1 | 0 | 0.0 | . | . | LostDFs |
| Temp*Temp*[Ag] | 1 | 1 | 184.5 | 0.0013 | 0.9724 | |
| [Co]*Time*[Ag] | 1 | 1 | 3495965.1 | 24.4186 | 0.0017* | |
| [Co]*Time*Temp | 1 | 1 | 51642.6 | 0.3607 | 0.5670 | |
| [Co]*Time*Time | 1 | 0 | 0.0 | . | . | LostDFs |
| [Ag]*[Ag]*[Co] | 1 | 0 | 0.0 | . | . | LostDFs |

Table 6.4.2.1. The table reports the strength of the interaction between different terms at the source column based on their strength at the Prob>F column.

The P-value shows that time factor is playing major role interacting with both cobalt and silver concentrations. $[Ag]*Time$ and $[Co]*Time$ showed P-values of 0.0011 and 0.0054 respectively displaying high attainment to prove the statistical test. The magnetic hysteresis outcome showing time interaction with both cobalt and silver concentration levels shown at figures 6.4.2.4-6.4.2.9. Coercivity values were extracted from the hysteresis figures in order to feed table 6.3.1 with the response (coercivity (H_c)).

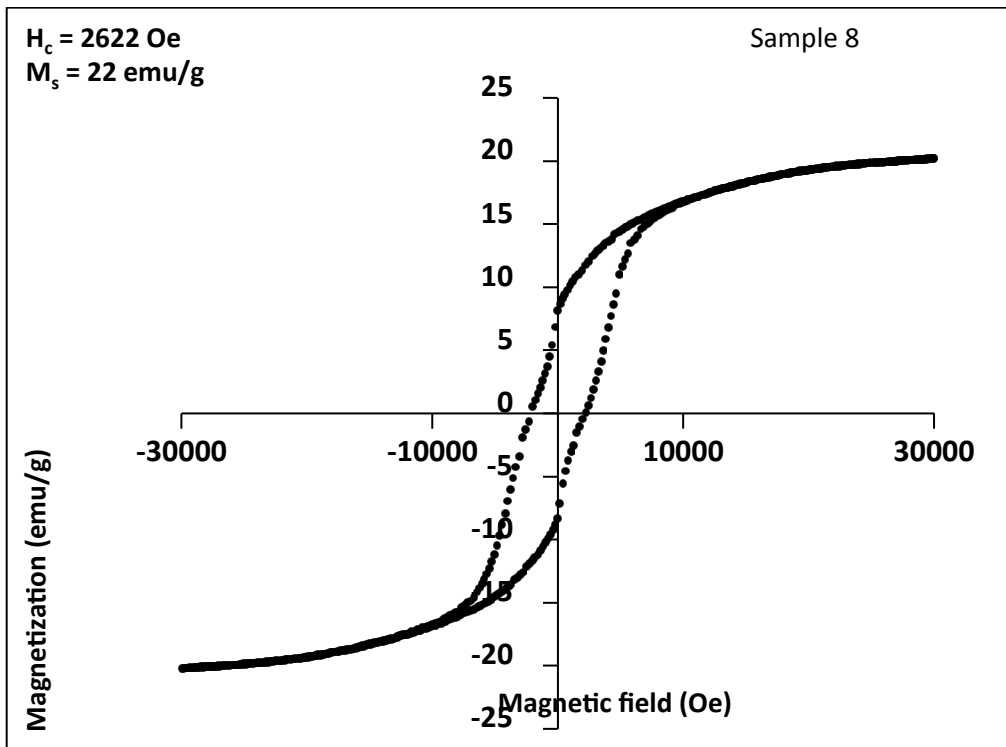


Figure 6.4.2.4. Hysteresis for sample 8 where silver concentration 0.017 M, cobalt concentration 0.039 M, temp 270°C, time 3 hrs. The silver concentration effect is pronounced in the hysteresis from the overlapping between the two phases soft and hard phases. While the it was possible to attain a coercivity of 2.6 kOe at low temperature as a concrescence of adding silver as nucleating agent. The poor magnetization is related to the non-ferromagnetic phase added to cobalt carbide.

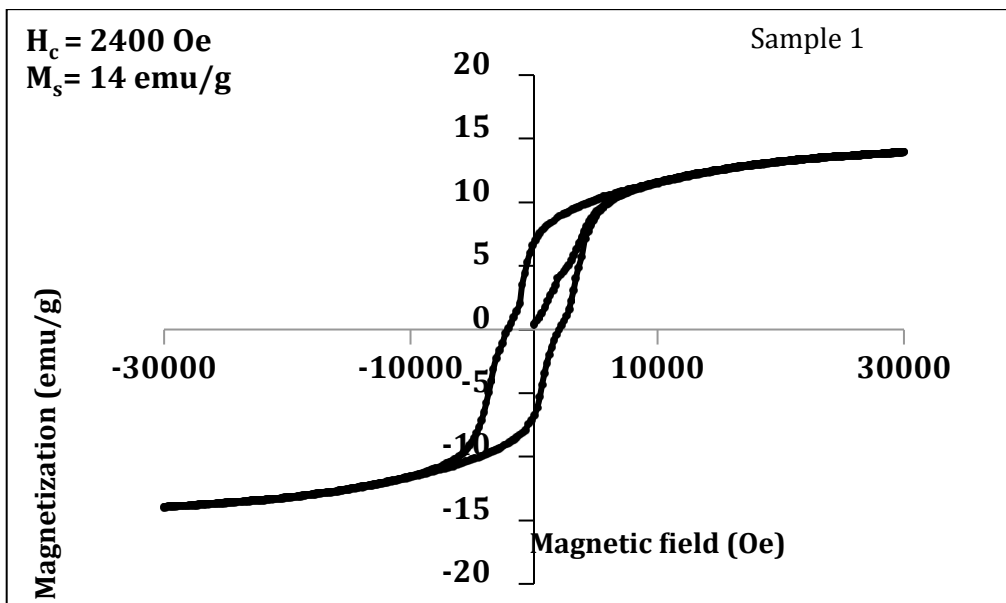


Figure 6.4.2.5. Hysteresis for sample 1 where silver concentration 0.0005 M, cobalt concentration 0.059 M, temp 300°C, time 1 hrs. The silver concentration effect is less pronounced since its less than previous figure, the hysteresis from the overlapping between the two phases soft and hard phases. While the it

was possible to attain a coercivity of 2.4 kOe at low temperature as a consequence of adding silver as nucleating agent.

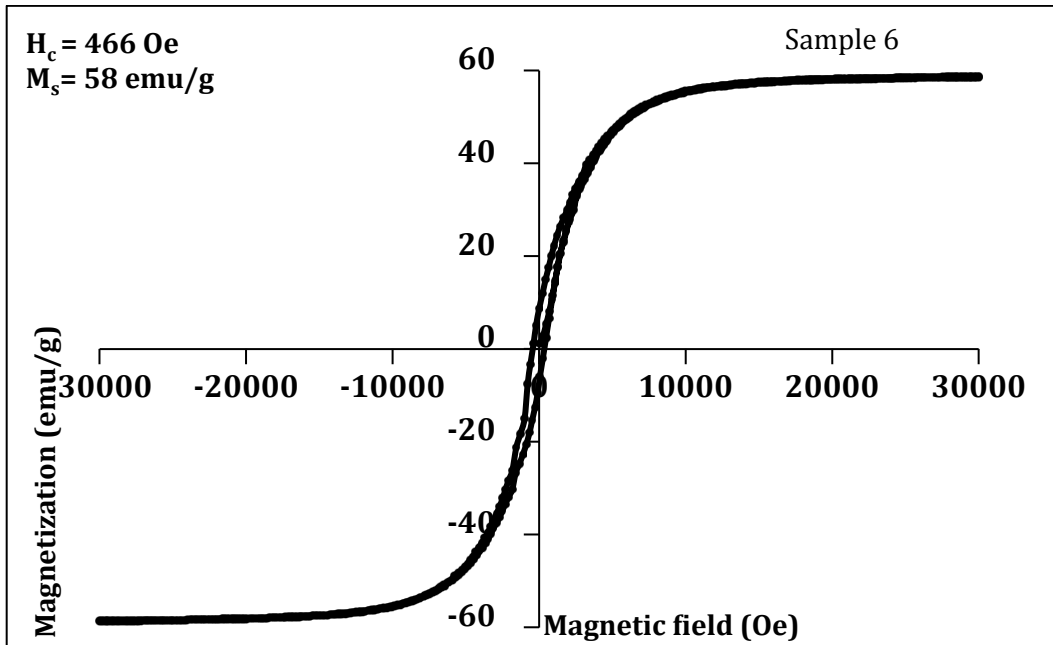


Figure 6.4.2.6. Hysteresis for sample 6 where silver concentration 0.017 M, cobalt concentration 0.039 M, temp 300°C, time 3 hrs. The low coercivity (466 Oe) indicates that cobalt carbide phase did not form, the phase is close to cobalt structure since magnetization saturated at 60 emu/g with low coercivity.

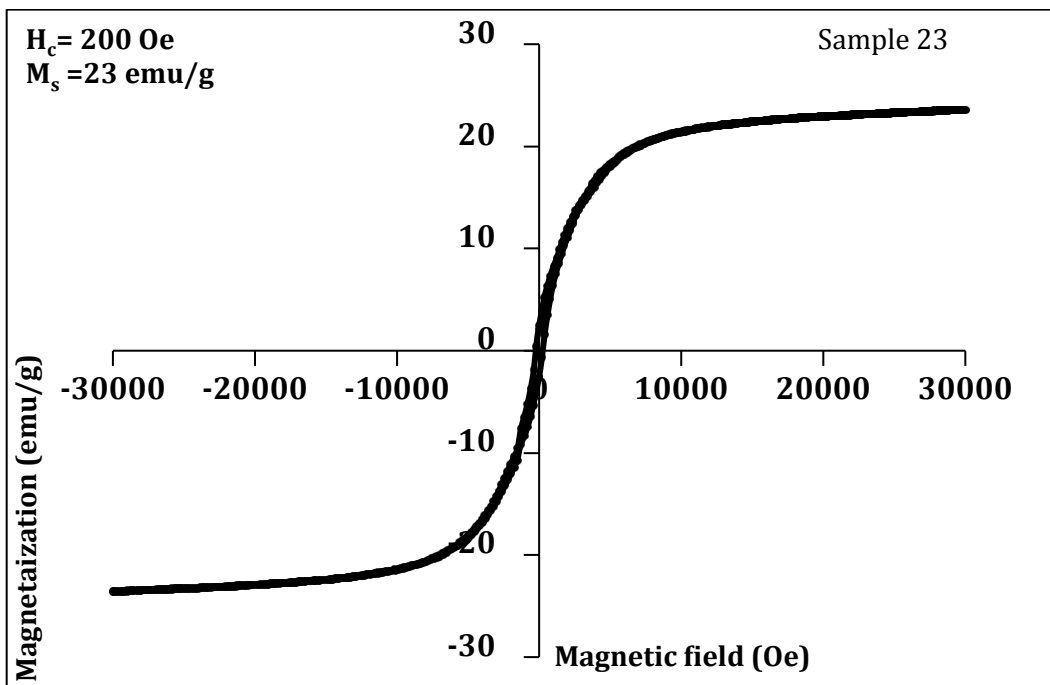


Figure 6.4.2.7. Hysteresis for sample 23 where silver concentration 0.0005 M, cobalt concentration 0.059 M, temp 270°C, time 3 hrs. The low coercivity (200 Oe) indicates that cobalt carbide phase did not form.

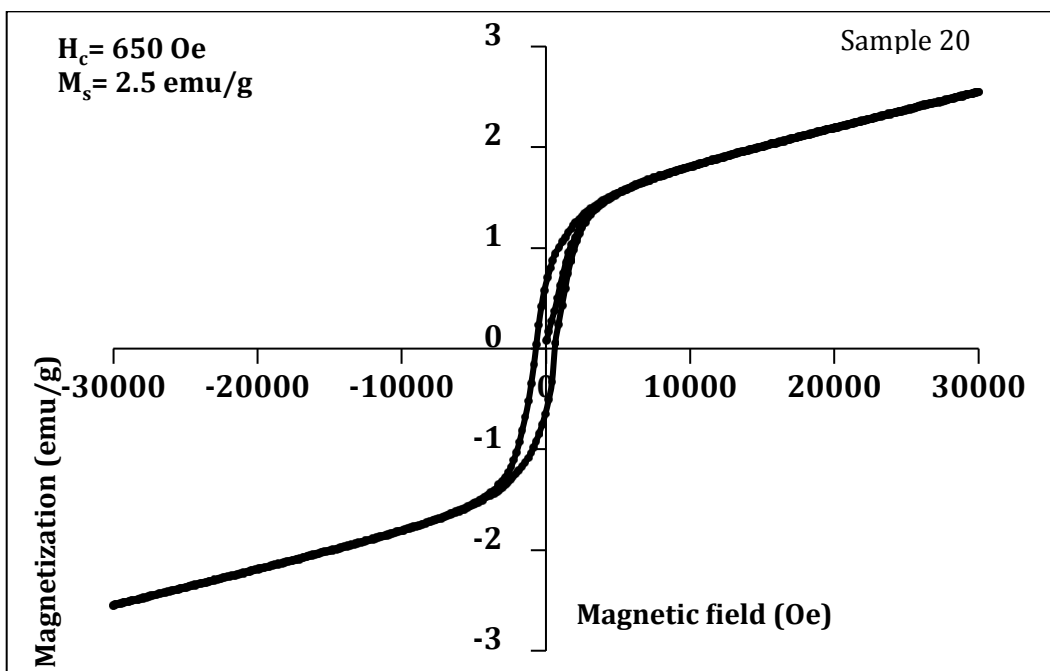


Figure 6.4.2.8. Hysteresis for sample 20 where silver concentration 0.017 M, cobalt concentration 0.039 M, temp 300°C, time 1 hrs. The low coercivity (650 Oe) indicates that cobalt carbide phase did not form. The poor magnetization is related to insufficient source of magnetic material resulted from the low cobalt precursor concentration.

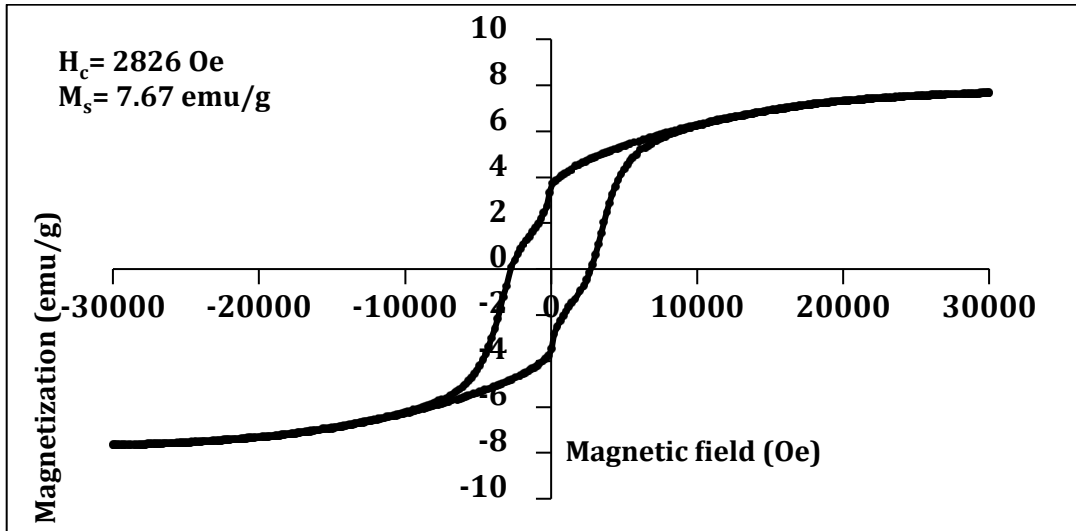


Figure 6.4.2.4.9 Hysteresis for sample 20 where silver concentration 0.017 M, cobalt concentration 0.039 M, temp 300°C, time 1 hrs. The low coercivity (650 Oe) indicates that cobalt carbide phase did not form. The poor magnetization is related to insufficient source of magnetic material resulted from the low cobalt precursor concentration.

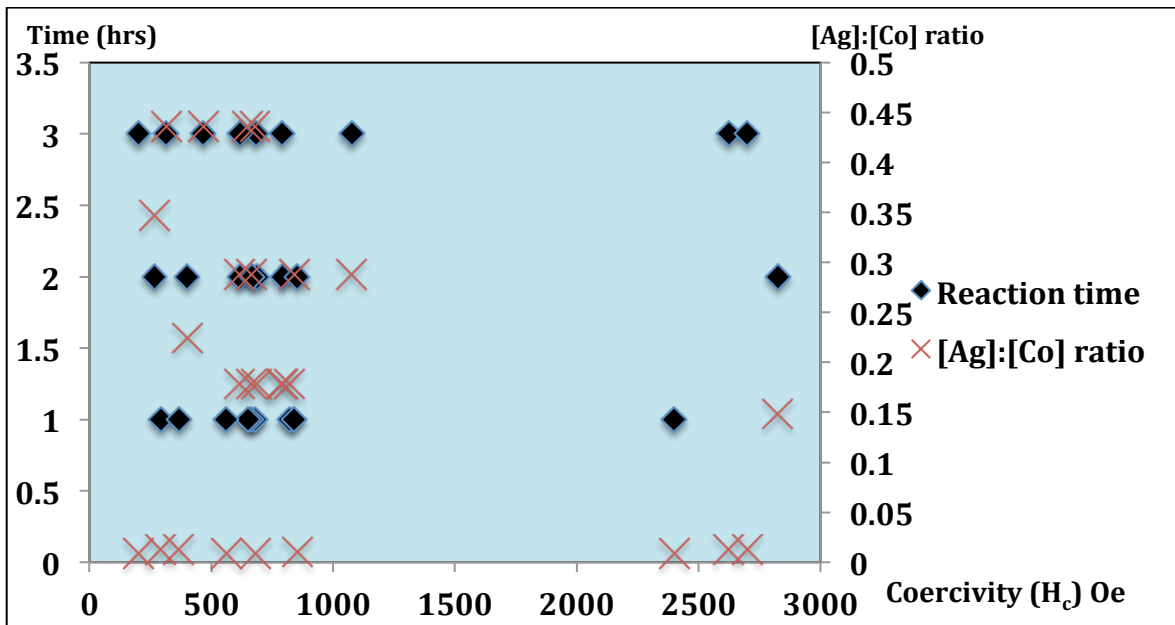


Figure 6.4.2.11 One factor at a time vs the response coercivity H_c in Oe.

The variation in coercivities figure 6.4.2.11 can be attributed to the defects in the non-uniform interfacial between the nonmagnetic parts and the magnetic source created from introducing silver nanoparticle especially in the high concentration samples shown in figure 2 6.4.2.7 and 6.4.2.8. The defects at the interfacial can be related to the magnetic pinning phenomena, which can be revealed at low temperature when testing in VSM.^{10,23,24}

Silver nano particle in graphite sheets have shown ferromagnetic behavior although both are having diamagnetic state in bulk. The ferromagnetic is coming from the interaction between graphitic shell on the silver nano particles induced by the hybridization.⁷⁷

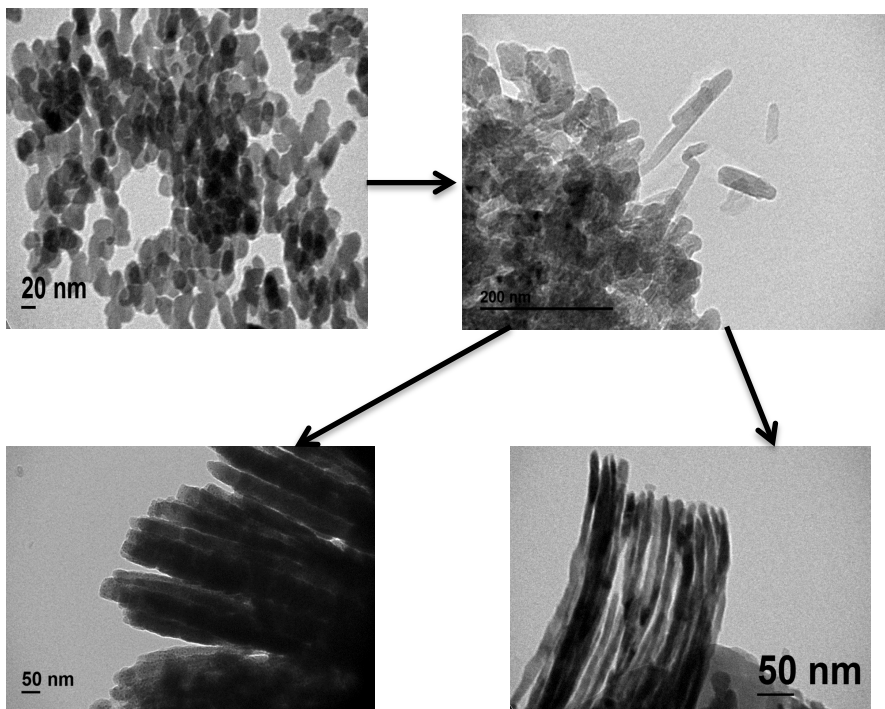


Figure 6.4.2.12. Showing change for cobalt carbide nanoparticle with the increase in Ag:Co ratio. From top to down as Ag concentration increase, nanorods are formed and will vary in aspect ratio as Ag concentration increase.

As the Ag:Co ratio increase, the coercivity increase considerably (3 kOe) figure 6.4.2.11 with formation of cobalt carbide nanorods as shown by TEM images in figure 6.4.2.12. The more increase in Ag:Co ratio, the more pronounced change in nanorods aspect ratio. The increase in Ag:Co ratio beyond 0.15 will drop the coercivity intensely (<1 kOe) figure 6.4.2.11. In previous literatures cobalt carbide shape control was not possible but instead crystallinity was possible with varying hydroxide.^{33,37} In this dissertation, increase in coercivity assisted by shape control was displayed. Silver nanoparticles revealed the prospect or providing catalytic sites for the cobalt carbide in burst nucleation process. This results in directing the growth and hence provides better control on particle shape and altering shape anisotropy.

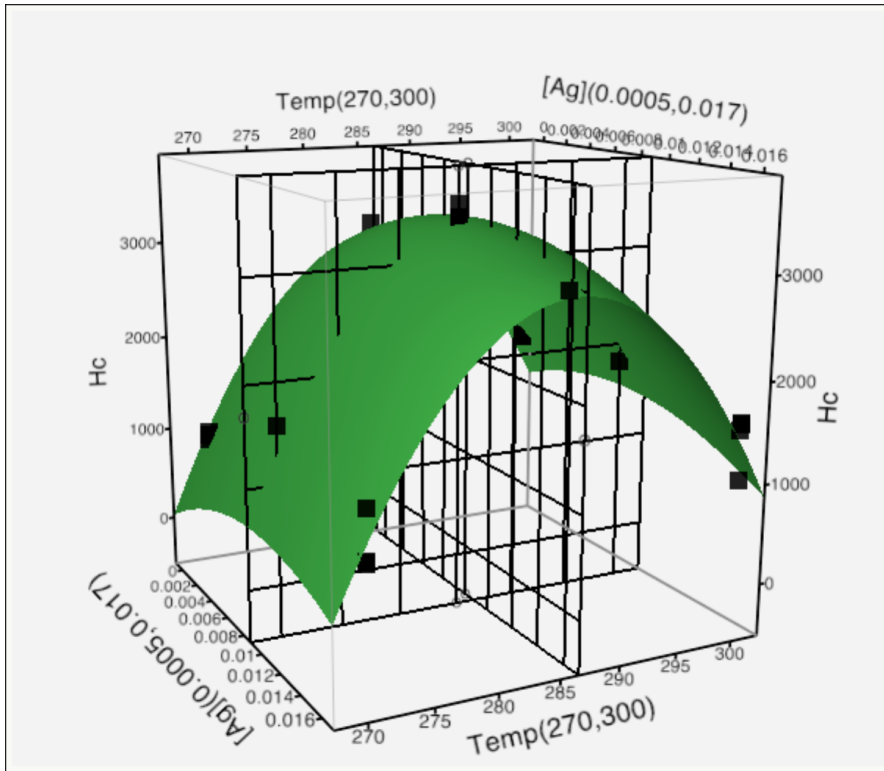


Figure 6.4.2.13. Surface profile showing saddle point for the profile of the effects; Ag, Temp vs the response H_c . The black points represent the design points in the design table.

In figure 6.4.2.13 provides information about the surface profile behavior with the change in Co concentration and reaction temperature with coercivity change H_c .

References

- (1) Gutfleisch, O.; Willard, M. A.; Brück, E.; Chen, C. H.; Sankar, S. G.; Liu, J. P. *Advanced Materials* **2011**, *23*, 821.
- (2) Coey, J. M. D. *Magnetics, IEEE Transactions on* **2011**, *47*, 4671.
- (3) *Demand for rare earth materials in permanent magnets*, Arnold Magnetic Technologies
- (4) Chikazumi, S. *Physics of Ferromagnetism*; Oxford University: Oxford, England, 1997; Vol. 2.
- (5) Tannous, C.; Gieraltowski, J. *European Journal of Physics* **2008**, *29*, 475.
- (6) Coey, J. M. D. *Magnetism and Magnetic Materials*; Cambridge University Press 2010.
- (7) Cullity, B. D. *Introduction to Magnetic Materials*, 1972.
- (8) Carpenter, E. E. *Journal of Magnetism and Magnetic Materials* **2001**, *225*, 17.
- (9) Zamanpour, M.; Bennett, S.; Taheri, P.; Chen, Y.; Harris, V. G. *Journal of Applied Physics* **2014**, *115*, 17A747.
- (10) Wen, T.; Krishnan, K. M. *Journal of Applied Physics* **2011**, *109*, 07B515.
- (11) Leslie-Pelecky, D. L.; Rieke, R. D. *Chemistry of Materials* **1996**, *8*, 1770.
- (12) Spaldin, N. A. *Physics of Ferroelectrics: A Modern Perspective*; Springer: Berlin 2007; Vol. 105.
- (13) Viau, G.; Garcia, C.; Maurer, T.; Chaboussant, G.; Ott, F.; Soumare, Y.; Piquemal, J. Y. *physica status solidi (a)* **2009**, *206*, 663.
- (14) Gandha, K.; Elkins, K.; Poudyal, N.; Liu, X.; Liu, J. P. *Sci. Rep.* **2014**, *4*.
- (15) Wen, T.; Krishnan, K. M. *Journal of Physics D: Applied Physics* **2011**, *44*, 393001.
- (16) Durst, K. D.; Kronmüller, H. *Journal of Magnetism and Magnetic Materials* **1987**, *68*, 63.
- (17) El-Gendy, A. A.; Qian, M.; Huba, Z. J.; Khanna, S. N.; Carpenter, E. E. *Applied Physics Letters* **2014**, *104*, 023111.
- (18) El-Gendy, A. A.; Almugaiteeb, T.; Carpenter, E. E. *Journal of Magnetism and Magnetic Materials* **2013**, *348*, 136.
- (19) Bertotti, G. *Hysteresis in Magnetism: For Physicists, Materials Scientists, and Engineers*; ACADEMIC PressINC, 1998.
- (20) Ait Atmane, K.; Zighem, F.; Soumare, Y.; Ibrahim, M.; Boubekri, R.; Maurer, T.; Margueritat, J.; Piquemal, J.-Y.; Ott, F.; Chaboussant, G.; Schoenstein, F.; Jouini, N.; Viau, G. *Journal of Solid State Chemistry* **2013**, *197*, 297.
- (21) Palchoudhury, S.; Xu, Y.; Goodwin, J.; Bao, Y. *Journal of Applied Physics* **2011**, *109*, 07E314.
- (22) Ung, D.; Viau, G.; Ricolleau, C.; Warmont, F.; Gredin, P.; Fiévet, F. *Advanced Materials* **2005**, *17*, 338.
- (23) Tan, X. H.; Chan, S. F.; Han, K.; Xu, H. *Scientific Reports* **2014**, *4*, 6805.
- (24) Zhao, G. P.; Wang, X. L. *Physical Review B* **2006**, *74*, 012409.

- (25) Coehoorn, R.; de Mooij, D. B.; de Waard, C. *Journal of Magnetism and Magnetic Materials* **1989**, *80*, 101.
- (26) Abou-Hassan, A.; Bazzi, R.; Cabuil, V. *Angewandte Chemie International Edition* **2009**, *48*, 7180.
- (27) Nightingale, A. M.; de Mello, J. C. *Journal of Materials Chemistry* **2010**, *20*, 8454.
- (28) Nightingale, A. M.; de Mello, J. C. *ChemPhysChem* **2009**, *10*, 2612.
- (29) Tiggelaar, R. M.; Male, P. v.; Berenschot, J. W.; Gardeniers, J. G. E.; Oosterbroek, R. E.; Croon, M. H. J. M. d.; Schouten, J. C.; Berg, A. v. d.; Elwenspoek, M. C. *Sensors and Actuators A: Physical* **2005**, *119*, 196.
- (30) Song, Y.; Modrow, H.; Henry, L. L.; Saw, C. K.; Doomes, E. E.; Palshin, V.; Hormes, J.; Kumar, C. S. S. R. *Chemistry of Materials* **2006**, *18*, 2817.
- (31) Duffy, D. C.; McDonald, J. C.; Schueller, O. J. A.; Whitesides, G. M. *Analytical Chemistry* **1998**, *70*, 4974.
- (32) Yen, B. K. H.; Stott, N. E.; Jensen, K. F.; Bawendi, M. G. *Advanced Materials* **2003**, *15*, 1858.
- (33) Huba, Z. J.; Carpenter, E. E. *Journal of Applied Physics* **2012**, *111*, 07B529.
- (34) Huba, Z. J.; Carpenter, E. E. *CrystEngComm* **2013**, *15*, 8919.
- (35) Savage, P. E.; Gopalan, S.; Mizan, T. I.; Martino, C. J.; Brock, E. E. *AIChE Journal* **1995**, *41*, 1723.
- (36) Blosi, M.; Albonetti, S.; Dondi, M.; Martelli, C.; Baldi, G. *J Nanopart Res* **2011**, *13*, 127.
- (37) Zhang, Y.; Chaubey, G. S.; Rong, C.; Ding, Y.; Poudyal, N.; Tsai, P.-c.; Zhang, Q.; Liu, J. P. *Journal of Magnetism and Magnetic Materials* **2011**, *323*, 1495.
- (38) Cheng, J.; Hu, P.; Ellis, P.; French, S.; Kelly, G.; Lok, C. M. *The Journal of Physical Chemistry C* **2010**, *114*, 1085.
- (39) Carroll, K. J.; Huba, Z. J.; Spurgeon, S. R.; Qian, M.; Khanna, S. N.; Hudgins, D. M.; Taheri, M. L.; Carpenter, E. E. *Applied Physics Letters* **2012**, *101*, 012409.
- (40) Tsakoumis, N. E.; Rønning, M.; Borg, Ø.; Rytter, E.; Holmen, A. *Catalysis Today* **2010**, *154*, 162.
- (41) Hinotsu, T.; Jeyadevan, B.; Chinnasamy, C. N.; Shinoda, K.; Tohji, K. *Journal of Applied Physics* **2004**, *95*, 7477.
- (42) Fox, J. M. *A comparison of slurry versus fixed-bed reactor design principles for methanol and Fischer-Tropsch distillate production*, 1990.
- (43) Yang, S.-Y.; Cheng, F.-Y.; Yeh, C.-S.; Lee, G.-B. *Microfluid Nanofluid* **2010**, *8*, 303.
- (44) Jahn, A.; Reiner, J.; Vreeland, W.; DeVoe, D.; Locascio, L.; Gaitan, M. *J Nanopart Res* **2008**, *10*, 925.
- (45) Lin, X. Z.; Terepka, A. D.; Yang, H. *Nano Letters* **2004**, *4*, 2227.
- (46) Patil, G. A.; Bari, M. L.; Bhanvase, B. A.; Ganvir, V.; Mishra, S.; Sonawane, S. H. *Chemical Engineering and Processing: Process Intensification* **2012**, *62*, 69.
- (47) Krishnadasan, S.; Tovilla, J.; Vilar, R.; deMello, A. J.; deMello, J. C. *Journal of Materials Chemistry* **2004**, *14*, 2655.

- (48) Nakamura, H.; Li, X.; Wang, H.; Uehara, M.; Miyazaki, M.; Shimizu, H.; Maeda, H. *Chemical Engineering Journal* **2004**, *101*, 261.
- (49) Harris, V. G.; Chen, Y.; Yang, A.; Yoon, S.; Chen, Z.; Geiler, A. L.; Gao, J.; Chinnasamy, C. N.; Lewis, L. H.; Vittoria, C.; Carpenter, E. E.; Carroll, K. J.; Goswami, R.; Willard, M. A.; Kurihara, L.; Gjoka, M.; Kalogirou, O. *Journal of Physics D: Applied Physics* **2010**, *43*, 165003.
- (50) Köhler, J. M.; Abahmane, L.; Wagner, J.; Albert, J.; Mayer, G. *Chemical Engineering Science* **2008**, *63*, 5048.
- (51) Collins, J.; The Irish Times: September 23, 2005
- (52) Aidin Lak , F. L., Jan M. Scholtyssek , Jan Dieckhoff , Kathrin Fiege , and Meinhard Schilling *IEEE TRANSACTIONS ON MAGNETICS*, **2013**, *49*.
- (53) Silva, V. B.; Rouboa, A. *Applied Mathematics and Computation* **2012**, *218*, 6733.
- (54) Montgomery, D. C. *Design and analysis of experiments* Eighth edition ed., 2008.
- (55) Anscombe, F. *Graphs in Statistical Analysis*; The American Statistician , 1973.
- (56) Kauffmann-Weiss, S.; Hamann, S.; Gruner, M. E.; Schultz, L.; Ludwig, A.; Fähler, S. *Acta Materialia* **2012**, *60*, 6920.
- (57) Kneller, E. F.; Luborsky, F. E. *Journal of Applied Physics* **1963**, *34*, 656.
- (58) Khajeh, M. *Biol Trace Elem Res* **2010**, *135*, 355.
- (59) Chakroune, N.; Viau, G.; Ricolleau, C.; Fievet-Vincent, F.; Fievet, F. *Journal of Materials Chemistry* **2003**, *13*, 312.
- (60) Carroll, K. J.; Reveles, J. U.; Shultz, M. D.; Khanna, S. N.; Carpenter, E. E. *The Journal of Physical Chemistry C* **2011**, *115*, 2656.
- (61) Fievet, F.; Lagier, J. P.; Blin, B.; Beaudoin, B.; Figlarz, M. *Solid State Ionics* **1989**, *32-33, Part 1*, 198.
- (62) LaMer, V. K.; Dinegar, R. H. *Journal of the American Chemical Society* **1950**, *72*, 4847.
- (63) Thanh, N. T. K.; Maclean, N.; Mahiddine, S. *Chemical Reviews* **2014**, *114*, 7610.
- (64) Xu, S.; Adiga, N.; Ba, S.; Dasgupta, T.; Wu, C. F. J.; Wang, Z. L. *ACS Nano* **2009**, *3*, 1803.
- (65) Kim, K. D.; Han, D. N.; Kim, H. T. *Chemical Engineering Journal* **2004**, *104*, 55.
- (66) Hiromi, K.; Hiroyuki, A.; Yasuyuki, S.; Mihoko, K.; Takuya, U.; Masatoshi, Y.; Atsushi, T.; Hiroshi, Y. *Japanese Journal of Applied Physics* **2005**, *44*, 2077.
- (67) Kolhatkar, A. G.; Jamison, A. C.; Litvinov, D.; Willson, R. C.; Lee, T. R. *International Journal of Molecular Sciences* **2013**, *14*, 15977.
- (68) Fan, F.-R.; Liu, D.-Y.; Wu, Y.-F.; Duan, S.; Xie, Z.-X.; Jiang, Z.-Y.; Tian, Z.-Q. *Journal of the American Chemical Society* **2008**, *130*, 6949.
- (69) Sun, Y.; Xia, Y. *Science* **2002**, *298*, 2176.
- (70) Yong, K.-T.; Sahoo, Y.; Swihart, M. T.; Prasad, P. N. *Colloids and Surfaces A: Physicochemical and Engineering Aspects* **2006**, *290*, 89.

- (71) Tailhades, P.; Villette, C.; Rousset, A.; Kulkarni, G. U.; Kannan, K. R.; Rao, C. N. R.; Lenglet, M. *Journal of Solid State Chemistry* **1998**, *141*, 56.
- (72) Chin, S. F.; Iyer, K. S.; Raston, C. L. *Crystal Growth & Design* **2009**, *9*, 2685.
- (73) Repain, V.; Baudot, G.; Ellmer, H.; Rousset, S. *Materials Science and Engineering: B* **2002**, *96*, 178.
- (74) Gregg, K. A.; Perera, S. C.; Lawes, G.; Shinozaki, S.; Brock, S. L. *Chemistry of Materials* **2006**, *18*, 879.
- (75) Carroll, K. J.; Hudgins, D. M.; Spurgeon, S.; Kemner, K. M.; Mishra, B.; Boyanov, M. I.; Brown, L. W.; Taheri, M. L.; Carpenter, E. E. *Chemistry of Materials* **2010**, *22*, 6291.
- (76) Maurice, J. L.; Imhoff, D.; Etienne, P.; Durand, O.; Dubois, S.; Piraux, L.; George, J. M.; Galtier, P.; Fert, A. *Journal of Magnetism and Magnetic Materials* **1998**, *184*, 1.
- (77) Caudillo, R.; Gao, X.; Escudero, R.; José-Yacaman, M.; Goodenough, J. B. *Physical Review B* **2006**, *74*, 214418.
- (78) Sun, Y.; Mayers, B.; Herricks, T.; Xia, Y. *Nano Letters* **2003**, *3*, 955.
- (79) Habas, S. E.; Lee, H.; Radmilovic, V.; Somorjai, G. A.; Yang, P. *Nat Mater* **2007**, *6*, 692.
- (80) Morgenstern, K.; Kibsgaard, J.; Lauritsen, J. V.; Lægsgaard, E.; Besenbacher, F. *Surface Science* **2007**, *601*, 1967.
- (81) Zhang, Z.; Dai, S.; Blom, D. A.; Shen, J. *Chemistry of Materials* **2002**, *14*, 965.
- (82) Suber, L.; Fiorani, D.; Scavia, G.; Imperatori, P.; Plunkett, W. R. *Chemistry of Materials* **2007**, *19*, 1509.
- (83) In *A Handbook of Lattice Spacings and Structures of Metals and Alloys*; Pearson, W. B., Ed.; Pergamon: 1958; Vol. 4, p iv.